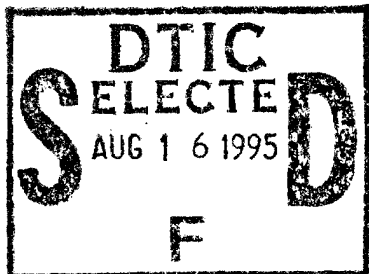


62

NAVAL POSTGRADUATE SCHOOL MONTEREY, CALIFORNIA



Original contains color
plates: All DTIC reproductions will be in black and white

THESIS

ANALYSIS OF
THE EAST ASIAN COLD SURGE
USING A 15-YEAR NAVY DATA SET

by

James R. Jarvis

March, 1995

Thesis Advisor:
Co-Advisor:

Chih-Pei Chang
Jeng Ming Chen

Approved for public release; distribution is unlimited.

19950814 079

DTIC QUALITY INSPECTED 1

364

REPORT DOCUMENTATION PAGE

Form Approved OMB No. 0704-0188

Public reporting burden for this collection of information is estimated to average 1 hour per response, including the time for reviewing instruction, searching existing data sources, gathering and maintaining the data needed, and completing and reviewing the collection of information. Send comments regarding this burden estimate or any other aspect of this collection of information, including suggestions for reducing this burden, to Washington Headquarters Services, Directorate for Information Operations and Reports, 1215 Jefferson Davis Highway, Suite 1204, Arlington, VA 22202-4302, and to the Office of Management and Budget, Paperwork Reduction Project (0704-0188) Washington DC 20503.

1. AGENCY USE ONLY (<i>Leave blank</i>)			2. REPORT DATE March, 1995.	3. REPORT TYPE AND DATES COVERED Master's Thesis
4. TITLE AND SUBTITLE ANALYSIS OF THE EAST ASIAN COLD SURGE USING A 15-YEAR NAVY DATA SET			5. FUNDING NUMBERS	
6. AUTHOR(S) James R. Jarvis			8. PERFORMING ORGANIZATION REPORT NUMBER	
7. PERFORMING ORGANIZATION NAME(S) AND ADDRESS(ES) Naval Postgraduate School Monterey CA 93943-5000			10. SPONSORING/MONITORING AGENCY REPORT NUMBER	
9. SPONSORING/MONITORING AGENCY NAME(S) AND ADDRESS(ES)			11. SUPPLEMENTARY NOTES The views expressed in this thesis are those of the author and do not reflect the official policy or position of the Department of Defense or the U.S. Government.	
12a. DISTRIBUTION/AVAILABILITY STATEMENT Approved for public release; distribution is unlimited.			12b. DISTRIBUTION CODE	
13. ABSTRACT (<i>maximum 200 words</i>) The East Asian winter monsoon cold surge is examined using Navy tropical Global Band Analysis data for January-March of 1975-1988. Multiple-set Canonicle Correlation (MCC) analysis, single-point correlation analysis, and composite analysis are used to determine the the cold surge structure over a broad domain that includes the western Pacific and eastern Indian ocean. The results show that the structure of the cold surge is manifested in MCC modes 1 and 2 of surface v calculated over both the East and South China Seas. Single-point correlation and composite analyses indicate that the surge can be viewed as a single mode over a rather broad region, with an average period of 8 days, that includes simultaneous eastward propagating longwaves across the East China Sea and northwestern Pacific, and equatorward propagating surge waves across the South China Sea. Composite analyses during strong events also reveal cross-equatorial surge influence present at low levels and increases in divergence over the maritime continent at 200 hPa. MCC modes 3 and 4 calculated over a small spatial domain that includes the East China Sea describe 3-day eastward propagating waves with wavelengths on the order of 1500-2000 km. Associated with these shorter waves are modest surge waves that also propagate equatorward across the South China Sea.				
14. SUBJECT TERMS Cold Surge, Northeast Monsoon, Winter Monsoon			15. NUMBER OF PAGES 118	
16. PRICE CODE			17. SECURITY CLASSIFI- CATION OF REPORT Unclassified	
18. SECURITY CLASSIFI- CATION OF THIS PAGE Unclassified			19. SECURITY CLASSIFI- CATION OF ABSTRACT Unclassified	
20. LIMITATION OF ABSTRACT UL			NSN 7540-01-280-5500	

Standard Form 298 (Rev. 2-89)
Prescribed by ANSI Std. Z39-18 298-102

Approved for public release; distribution is unlimited.

**ANALYSIS OF THE EAST ASIAN COLD SURGE
USING A 15-YEAR NAVY DATA SET**

James R. Jarvis
Lieutenant, United States Navy
B.E.S., Johns Hopkins University, 1985

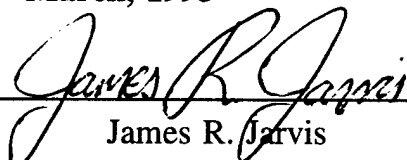
Submitted in partial fulfillment
of the requirements for the degree of

**MASTER OF SCIENCE IN METEOROLOGY AND PHYSICAL
OCEANOGRAPHY**

from the

**NAVAL POSTGRADUATE SCHOOL
March, 1995**

Author:



James R. Jarvis

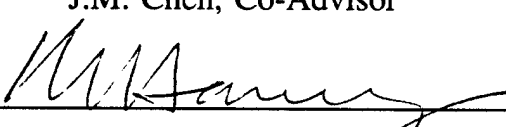
Approved by:



C.P. Chang, Thesis Advisor



J.M. Chen, Co-Advisor



R.L. Haney, Chairman
Department of Meteorology

ABSTRACT

The East Asian winter monsoon cold surge is examined using Navy tropical Global Band Analysis data for January-March of 1975-1988. Multiple-set Canonicle Correlation (MCC) analysis, single-point correlation analysis, and composite analysis are used to determine the the cold surge structure over a broad domain that includes the western Pacific and eastern Indian ocean.

The results show that the structure of the cold surge is manifested in MCC modes 1 and 2 of surface v calculated over both the East and South China Seas. Single-point correlation and composite analyses indicate that the surge can be viewed as a single mode over a rather broad region, with an average period of 8 days, that includes simultaneous eastward propagating longwaves across the East China Sea and northwestern Pacific, and equatorward propagating surge waves across the South China Sea. Composite analyses during strong events also reveal cross-equatorial surge influence present at low levels and increases in divergence over the maritime continent at 200 hPa.

MCC modes 3 and 4 calculated over a small spatial domain that includes the East China Sea describe 3-day eastward propagating waves with wavelengths on the order of 1500-2000 km. Associated with these shorter waves are modest surge waves that also propagate equatorward across the South China Sea.

Accesion For	
NTIS	CRA&I
DTIC	TAB
Unannounced	
Justification	
By _____	
Distribution / _____	
Availability Codes	
Dist	Avail and / or Special
A-1	

TABLE OF CONTENTS

I. INTRODUCTION	1
A. SYNOPTIC DISTURBANCES IN THE TROPICS	1
B. THE EAST ASIAN WINTER MONSOON	4
1. Cold Surges	4
2. Cyclones and Cyclogenesis in the East China Sea	5
II. DATA AND METHODOLOGY	9
A. DATA TYPE	9
B. ANALYSIS METHODS	10
1. Multiple-set Canonical Correlation Analysis	10
2. Composite and Single-point Correlation Analyses	13
C. DATA FILTERING	14
III. LEADING MCC MODES BASED ON SURFACE <i>V</i>	21
A. THE SOUTH CHINA SEA DOMAIN	21
B. THE EAST CHINA SEA DOMAIN	22
1. Modes 1 and 2	22
2. Modes 3 and 4	26
IV. STRUCTURE OF MOTIONS BASED ON CORRELATION AND COMPOSITE ANALYSES	63
A. SOUTH CHINA SEA MCC MODE 1	63
1. Single-point Correlation Analysis	63
2. Composite Analysis	64
a. Strong Cases	64
b. Medium Cases	66
c. Divergence	67

B. EAST CHINA SEA MCC MODE 3	68
1. Single-point Correlation Analysis	68
2. Composite Analysis	69
V. SUMMARY AND CONCLUSIONS	91
LIST OF REFERENCES	95
INITIAL DISTRIBUTION LIST	101

LIST OF FIGURES

Figure 1. Map showing the core South China Sea domain imbedded in the large western Pacific and eastern Indian ocean domain.	16
Figure 2. Map showing the core East China Sea domain imbedded in the large western Pacific and eastern Indian ocean domain.	17
Figure 3. Weighting function for MCC mode 1, East China Sea domain, of the surface meridional winds (v) for 12 consecutive twelve-hourly frames from 00h (T0) to 132h (T11). Contour interval is 0.03 and dashed lines correspond to northerly winds when MCC mode 1 amplitude is positive. No prior filtering was applied to the data.	18
Figure 4. Same as Fig. 3 except the data was time-differenced over a 24 hour period prior to analysis.	19
Figure 5. Weighting function for MCC mode 1, South China Sea domain, of the surface meridional wind (v) for 12 consecutive twelve-hourly frames from 00h (T0) to 132h (T11). Contour interval is 0.03 and dashed lines correspond to northerly winds when MCC mode 1 is positive. Data was passed through a 14-day high pass filter prior to analysis.	28
Figure 6. Same as Fig. 5 except for MCC mode 2.	29
Figure 7. Lag-correlation plots for MCC modes 1 and 2, South China Sea domain. The two modes correlated in each plot are labeled in the upper left corners. Each interval on the x-axis represents 2.0 days (4*12h).	30
Figure 8. Time series of the time-integrated amplitude coefficients of MCC modes 1 and 2, South China Sea domain, for the winters 1975 and 1976. The power spectrum for each time series is shown at the right with the 3, 6, 9, and 12 day periods labeled.	31
Figure 9. Same as Fig. 8 except for winters 1978 and 1979.	32
Figure 10. Same as Fig. 8 except for winters 1980 and 1981.	33
Figure 11. Same as Fig. 8 except for winters 1982 and 1983.	34
Figure 12. Same as Fig. 8 except for winters 1984 and 1985.	35

Figure 13. Same as Fig. 8 except for winters 1986 and 1987.	36
Figure 14. Same as Fig. 8 except for winter 1988.	37
Figure 15. Average power spectrum for 13 winters, MCC modes 1 and 2 combined, South China Sea domain, with the 6, 9, and 12 day periods labeled.	38
Figure 16. Weighting function for MCC mode 1, East China Sea domain, of the surface meridional wind (v) for 12 consecutive twelve-hourly frames from 00h (T0) to 132h (T11). Contour interval is 0.03 and dashed lines correspond to northerly winds when MCC mode 1 amplitude is positive. Data was passed through a 14-day high pass filter prior to analysis.	39
Figure 17. Same as Fig. 16 except for MCC mode 2.	40
Figure 18. Lag correlation plots for MCC modes 1 and 2, East China Sea domain. The two modes correlated in each plot are labeled in the upper left corners. Each interval on the x-axis represents 2.0 days (4*12h).	41
Figure 19. Time series of the time-integrated amplitude coefficients of MCC modes 1 and 2, East China Sea domain, for the winters 1975 and 1976. The power spectrum for each time series is shown at the right with the 3, 6, 9, and 12 day periods labeled.	42
Figure 20. Same as Fig. 19 except for winters 1977 and 1978.	43
Figure 21. Same as Fig. 19 except for winters 1979 and 1980.	44
Figure 22. Same as Fig. 19 except for winters 1981 and 1982.	45
Figure 23. Same as Fig. 19 except for winters 1983 and 1984.	46
Figure 24. Same as Fig. 19 except for winters 1985 and 1986.	47
Figure 25. Same as Fig. 19 except for winters 1987 and 1988.	48
Figure 26. Average power spectrum for 14 winters, MCC modes 1 and 2 combined, East China Sea domain, with the 6, 9, and 12 day periods labeled.	49
Figure 27. Coherence and transfer function phase plots for the amplitude coefficient time series of MCC mode 1, South China Sea domain, and MCC mode 1, East China Sea domain. 3, 6, and 12 day periods are labeled.	50

Figure 28. Weighting function for MCC mode 3, East China Sea domain, with the surface meridional wind (v) for 6 consecutive twelve-hourly frames from 00h (T0) to 60h (T5). Contour interval is 0.03 and dashed lines correspond to northerly winds when MCC mode 3 is positive. Data was passed through a 14-day high pass filter prior to analysis.	51
Figure 29. Same as Fig. 28 except for MCC mode 4.	52
Figure 30. Time series of the time-integrated amplitude coefficients for MCC modes 3 and 4, East China Sea domain, for the winters 1975 and 1976. The power spectrum for each time series is shown at the right with the 3, 6, 9, and 12 day periods labeled.	53
Figure 31. Same as Fig. 30 except for winters 1977 and 1978.	54
Figure 32. Same as Fig. 30 except for winters 1979 and 1980.	55
Figure 33. Same as Fig. 30 except for winters 1981 and 1982.	56
Figure 34. Same as Fig. 30 except for winters 1983 and 1984.	57
Figure 35. Same as Fig. 30 except for winters 1985 and 1986.	58
Figure 36. Same as Fig. 30 except for winters 1987 and 1988.	59
Figure 37. Lag correlation plots for MCC modes 1,2,3, and 4, East China Sea domain. The two modes correlated in each plot are labeled in the upper left corners. Each interval on the x-axis represents 2.0 days (4*12h).	60
Figure 38. Average power spectrum for 14 winters, MCC modes 3 and 4 combined, East China Sea domain, with the 2 and 4 day periods labeled.	61
Figure 39. Single-point correlation patterns of surface v with MCC mode 1, South China Sea domain, at 12 consecutive 12-hourly time lags. Contour interval is 0.1 and negative values are dashed.	71
Figure 40. Same as Fig. 39 except for MCC mode 1, East China Sea domain.	72
Figure 41. Same as Fig. 39 except for 700 hPa v	73
Figure 42. Same as Fig. 39 except for 200 hPa v	74

Figure 43. Surface wind vector plots based on composites of the 13 strongest cold surge cases at 6 consecutive 24-hourly time lags with the background mean included. Vector scale is shown at the top of each frame.	75
Figure 44. Surface wind vector plots based on composites of the 13 strongest cold surge cases at 12 consecutive 12-hourly time lags with the background mean removed. Vector scale is shown at the top of each frame.	76
Figure 45. Same as Fig. 44 except for 700 hPa.	77
Figure 46. Same as Fig. 44 except for 200 hPa.	78
Figure 47. 200 hPa wind vector plots based on composites of the 13 strongest cold surge cases at 6 consecutive 24-hourly time lags with the background mean included. Vector scale is shown at the top of each frame.	79
Figure 48. Surface wind vector plots based on composites of 54 medium-strength cold surge cases at 12 consecutive 12-hourly time lags with the background mean removed. Vector scale is shown at the top of each frame.	80
Figure 49. Same as Fig. 48 except for 700 hPa.	81
Figure 50. Same as Fig. 48 except for 200 hPa.	82
Figure 51. Spatially averaged 200 hPa anomaly divergence fields based on composites of the 13 strongest cold surge cases at 12 consecutive 12-hourly time lags. Contour interval is 0.000002 1/s.	83
Figure 52. Same as Fig. 51 except for 54 medium-strength cases.	84
Figure 53. Single-point correlation patterns of surface v with MCC mode 3, East China Sea domain, at 6 consecutive 12-hourly time lags. Contour interval is 0.1 and negative values are dashed.	85
Figure 54. Same as Fig. 53 except for 700 hPa.	86
Figure 55. Same as Fig. 53 except for 200 hPa.	87
Figure 56. Surface wind vector plots based on composites of 27 cases at 6 consecutive 12-hourly time lags with the background mean removed. Vector scale is given at the top of each frame.	88
Figure 57. Same as Fig. 56 except for 700 hPa.	89

ACKNOWLEDGEMENT

The author would like to express his appreciation and thanks to thesis advisor, Professor C.P. Chang, for his steady guidance, and co-advisor, Dr. J.M. Chen, who provided much needed assistance with FORTRAN programming. A special thanks also to my wife, Sabine, and children, Alex and Anna, for their patience and support.

This work was supported in part by the National Science Foundation Grant ATM-9106495. The Global Band Analysis data were provided by the Fleet Numerical Meteorology and Oceanography Center, Monterey, California.

I. INTRODUCTION

The purpose of this paper is to examine the statistical characteristics of some tropical and subtropical synoptic-scale phenomena occurring during the East Asian winter monsoon based on a 14-year dataset. The statistical analyses are carried out using the Multiple-set Canonical Correlation Analysis (MCCA) technique that was recently developed by Chen *et al.* (1994). A brief review of the history of synoptic tropical motions is provided in section A. In section B, two significant aspects of the East Asian winter monsoon, broad-scale cold surges that penetrate into the tropics, and cyclogenesis in the East China Sea, are reviewed. Chapter II contains a brief description of the data sets and an overview of the analysis techniques used including MCCA. Chapter III provides a discussion of results obtained when MCCA is applied to two separate domains: the East China Sea and the South China Sea. In Chapter IV, composite analysis and single-point correlation analysis are performed based on the structure of the leading MCCA modes for the two regions. Chapter V provides a summary and conclusions.

A. SYNOPTIC DISTURBANCES IN THE TROPICS

Although the existence of wave disturbances in the tropics has been recognized since the 1930's, detailed study of tropical synoptic processes was not possible until upper air soundings became widely available after World War II. Prior studies were done using only surface data (e.g., Piersig 1936; Regula 1936; Dunn 1940). Upper air data from the Caribbean area was used by Riehl (1945) in his "waves in the easterlies" model which describes westward moving, wave-like oscillations in the basic easterly current of the lower troposphere. Even with upper air soundings, the study of tropical dynamics was, and still is, difficult due to the limited amount of data.

In the late 1960's, spectral analysis was beginning to be used to pull information from rawinsonde data collected at widely dispersed observing stations. Yanai *et al.* (1968) applied spectral analysis to rawinsonde data over the equatorial Pacific and found

westward propagating waves with eastward vertical tilt having periods of 4 to 5 days. These waves with wavelengths on the order of 6000 to 10000 km were subsequently identified with mixed Rossby-gravity waves in the equatorial stratosphere (Maruyama 1967, 1968). Wallace and Chang (1969) and Chang *et al.* (1970) also found waves in the equatorial western Pacific with a dominant 4 to 5 day period. These waves in the lower troposphere have a zonal wavelength of 2000 to 4000 km and a vertical tilt that systematically changes from eastward in the central Pacific to slightly westward in the extreme western Pacific. This east-west variation in vertical structure was also seen later when comparing years with warm and cold sea surface temperatures over the central and eastern Pacific. Warm years show a more equivalent barotropic structure while cold years show a more easterly tilt with height (Chang and Miller 1978).

In 1979, results of the First GARP Global Experiment (FGGE) fueled further investigations into the behavior of tropical disturbances over areas where there were previously little or no station data available. Nitta *et al.* (1985) and Nitta and Takayabu (1985) conducted a global survey of the tropical transients using FGGE observations for July and August. Nitta and Takayabu (1985) and Tai and Ogura (1987) also used the FGGE analyses to show the existence of west-northwestward propagating disturbances in the eastern Pacific.

Since 1979, global datasets have been analyzed and archived at various operational centers around the world. The availability of these global datasets greatly enhances the ability to conduct empirical tropical studies. Studies are no longer restricted to sparse station data or observations taken within limited-area networks during intensive field experiments. Of course, numerical model analysis data, while having global coverage, may not always be reliable, especially in the tropical data-sparse areas. Nevertheless, they have proven to be very useful. Reed *et al.* (1988) studied the synoptic evolution of African wave disturbances appearing in the European Center for Medium Range Weather Forecasts (ECMWF) analyses for the summer of 1985. They found that independent satellite data confirmed the African wave features depicted by ECMWF analyses over data-sparse regions.

More recently, Liebmann and Hendon (1990) studied the 1980-1987 ECMWF analyses of the near equatorial wind field during the September-December season. Their focus was primarily on the behavior of synoptic-scale disturbances occurring within 10 degrees north and south of the equator. They found westward propagating and equatorial trapped features in their 850 hPa meridional wind field with periods less than 6 days. The features looked somewhat like mixed Rossby-gravity waves. Lau and Lau (1990) used twice daily ECMWF global gridded analyses for the northern summers of 1980-1987. They examined lag-correlation and regression statistics of tropical fluctuations with synoptic time scales. Their results confirmed that a substantial amount of synoptic-scale variability in the tropics during northern summer is associated with propagating wave-like disturbances that remain coherent for several days.

In addition to the synoptic-period disturbances discussed above, intraseasonal oscillations have also been studied and found to have significant influence on tropical weather. The most well-known of these is the Madden-Julian Oscillation (MJO, Madden and Julian 1971). This is an eastward propagating, planetary-scale wave with zonal wavenumber one and dominant oscillations in the east-west (u) wind component. Observational studies of the MJO have shown that it plays a key role in governing tropical convection, particularly in the Indian monsoon region (e.g., Lau and Chan 1983). Salby and Hendon (1994) investigated the spectral character of tropical convection in an 11 year record of outgoing longwave radiation from the Advanced Very High Resolution Radiometer. They found that the space-time spectrum of convection possesses a broad peak at wavenumbers 1-3 and eastward periods of 35-95 days. This broad signal is associated with a large-scale anomaly that moves across and modulates the "climatological convection" over the equatorial Indian Ocean and western Pacific. Cardenas Amores (1994) used Navy Operational Global Analysis and Prediction System (NOGAPS) data for the summers 1989-1991 to study intraseasonal oscillations other than the MJO. Using MCCA, he found a near 20 day oscillation with a zonal half-wavelength around 3000-4000 km. Chen and Chen (1993) found a similar 10-20 day intraseasonal monsoon mode when they studied the 1979 FGGE data and daily rainfall estimates over India.

Most of these previous observational studies of the tropical synoptic scale motions focused on the northern summer period. In this study the focus will be on the northern winter.

B. THE EAST ASIAN WINTER MONSOON

1. Cold Surges

Perhaps the most well known event that occurs during the East Asian monsoon is the cold surge. According to Boyle and Chen (1987), a cold surge starts when 500 hPa northwesterly flow over Lake Baikal sets up the larger scale flow upon which short waves propagate toward the mean longwave trough that typically resides along the East Asian coast. The shortwaves move into phase with and amplify the longwave which produces a circulation that pushes cold air southward from eastern Siberia. At the surface, an anticyclone develops over China as a result of the low-level cold air advection and upper-level vorticity advection. The result is an outbreak of very cold air that flows eastward off the China coast and southward into the South China Sea that can have a significant impact on regional weather (Ramage 1975). The cold surge generally follows isentropic surfaces so that by the time it reaches the South China Sea, the surge is relatively shallow and its signal is usually not detected above 850 hPa. Although there exist many definitions of surge criteria, general consensus is that the event is marked by rapidly dropping surface temperatures over southern China accompanied by an increase in the northeasterly wind both off the East Asian coast and in the South China Sea (Boyle and Chen 1987).

The cold surge events are a good example of the interaction that takes place between the midlatitudes and the tropics. Chang and Lau (1982) analyzed 200 hPa winds of four winters and found that during surge periods, the midlatitude and tropical circulation components vary in a coherent way. Several investigators have noticed that the cold surge is often followed by increased tropical convection over the maritime continent (e.g., Lau and Chang 1987). Studies of data taken during the Winter Monsoon Experiment

(WMONEX) for the winters 1978-1979 have shown that the degree of convective activity in the southern South China Sea is modulated significantly by diurnal forcing of land/sea breeze circulations (Houze *et al.* 1981; Johnson and Priegnitz 1981). Chu and Park (1984) studied a cold surge event from the WMONEX and found a rapid southward mass transport in the lower troposphere from the midlatitudes to the tropics. Chang *et al.* (1979) studied the structures of cyclonic vortices near Borneo and found that the cold surge actually deepens the vortex probably due to increased organization of cumulus convection. Chang and Chen (1992) conducted a statistical study of 103 surge cases during 14 winter seasons. They found a relationship between the occurrence of cold surges over the South China Sea and the variation of the 200 hPa and surface tropical divergence from the western Pacific to the eastern Indian Ocean.

In this study we use the MCCA method to isolate the horizontal structure of the cold surge through surface meridional wind analysis. The time variation of the three-dimensional structure is then deduced from single-point correlation and composite analyses.

2. Cyclones and Cyclogenesis in the East China Sea

The nearly stationary major longwave in the northern hemisphere is located along the eastern coast of Asia. Manabe and Terpstra (1974) showed that the longwave pattern observed is probably due to topographic effects. Although the presence of the longwave has little effect on the growth rate and phase speeds of the fastest-growing linear disturbances, its location plays a key role in producing regions favorable to cyclone development downstream (Frederikson 1979). Observation of the oceanic regions east of the Asian continent, including the Sea of Japan and the East China Sea, certainly bears this out. Most of the Pacific ocean storms begin in these regions. Weak shallow disturbances that move off of southern mainland China often deepen and may deepen rapidly if an upper level trough reaches the coast coincidentally.

Nitta and Yamamoto (1973) analyzed the cyclogenesis frequency over East Asia (20°N to 45°N , 105°E to 150°E) for the period 1966 to 1970 and identified two types of

cyclonic disturbances. The first type is the typical baroclinic wave in which growth is due to baroclinic instability triggered by an upper-level trough in the westerlies with wavelengths on the order of 3000-4000 km. The second type is an intermediate-scale wave that has a horizontal wavelength of 1000 to 2000 km and is mostly confined to the lower half of the troposphere. At the initial stage of formation, the disturbance does not couple with any trough in the upper troposphere. Nitta and Yamamoto (1974) analyzed the structure of these intermediate-scale disturbances and found that the most frequently observed type in the winter has the warm air to the east side of the cyclone and cold air to the west in the lower troposphere, with cold air occupying the midtroposphere above the cyclone center. Boyle and Chen (1987) summarized the characteristics of the intermediate-scale disturbances originally given in a report for the Air Mass Transformation Experiment (AMTEX) (GARP 1981) as follows:

1. The characteristic scale of the disturbance is 1000 to 2000 km in the zonal direction.
2. The characteristic time scale is short when compared with that of the typical baroclinic wave.
3. The disturbances become active in a moist lower troposphere under the condition of a less stable stratification.
4. These disturbances do not appear to be directly associated with an upper tropospheric trough, and their kinetic energy is confined to the lower portion of the troposphere.
5. According to the radar observations, cumulus activity seems to be closely associated with the generation and development of these disturbances.

Boyle and Chen (1987) also note that the cyclones apparently require heat and moisture fluxes that are found in the East China Sea in order to develop and be maintained. In order to develop into full-scale cyclones that exhibit the usual baroclinic wave structure, the additional ingredient of upper-level forcing is needed. Saito (1977)

studied three intermediate-scale cyclones that formed during AMTEX 1975 and observed that these systems developed when a preexisting vortex moved off the continent into the East China Sea. These cyclones were strongest in the lowest layers and formed in a large-scale frontal zone. Development was negligible above 850 hPa.

In this study the MCCA of the surface meridional wind also identifies an intermediate-scale wave disturbance over the East China Sea during northern winter. The characteristics of these disturbances resemble the ones studied previously, but there are some differences.

II. DATA AND METHODOLOGY

A. DATA TYPE

The wind data used in this study are the tropical Global Band Analyses (GBA) produced by the Fleet Numerical Meteorology and Oceanographic Center (FNMOC), Monterey, California during 1974-1988. These data are the same set used by Chang and Chen (1992) in their case study of the winter monsoon cold surge over the South China Sea. These data were produced four times daily using objective analysis on a Mercator grid which extends from 60°N to 40°S. Grid point spacing is 2 1/2 degrees latitude and longitude. The Mercator secant projection results in a change in distance between grid points from a minimum value of 140 km at 60°N to a maximum value of 280 km at the equator. The objective analysis scheme takes advantage of all the reports in the operational data base including surface synoptic, aircraft, pilot balloons, rawinsonde, and satellite data. The analysis was performed every six hours for the surface, 700, 400, 250, and 200 hPa levels using a successive corrections method. The six-hour persistence field is used as the first guess; no model forecast is used. The disadvantage in using a persistence field as a first guess is that the analysis suffers over data-void regions. Over such areas, with no new observations to update the field, persistence may last for days. On the other hand, the analysis is not dependent on any model dynamics. Both wind and temperature were analyzed and then adjusted by a set of numerical variational analysis equations which incorporated the dynamical constraints of the momentum equations with friction included in the surface layer (Lewis and Grayson 1972).

In this study only the surface, 700 hPa, and 200 hPa 12 hourly wind data are used. At the surface the GBA is a particularly rich data set when compared with other operational surface analyses for the same time period. It includes all Navy and commercial ship data as well as land-based data. The analyses are drawn closely to the observations as there is no model constraint. At 200 hPa the data set is enriched by frequent commercial aircraft reports over the tropical western Pacific. Since 1979 cloud

top winds derived from the Japanese Geostationary Meteorology Satellite have also been incorporated. The surface meridional winds are used to calculate leading MCCA modes that show the dominant horizontal structure of winter monsoon synoptic events. Data from 200 hPa is used to determine associated upper-level patterns as well as calculate divergence which can be used as an indicator of deep tropical convection.

The data are analyzed over a three month period that includes January, February, and March during the years 1975-1988. These particular three months were chosen for two reasons: First, we wish to minimize any effect from tropical cyclones which are periodically "bogussed" into the GBA data. January, February, and March typically have the fewest number of tropical cyclones (JTWC 1988). Also, the winter monsoon synoptic phenomena we wish to study (i.e. cold surges) occur most often during this time period.

B. ANALYSIS METHODS

1. Multiple-set Canonical Correlation Analysis

The statistical method of analysis used in this study, Multiple-set Canonical Correlation Analysis (MCCA), is a particular type of eigentechnique designed to extract statistical information from datasets with large dimensions and long time periods. One of the earliest and most commonly used techniques of this type is the Principal Component Analysis (PCA) sometimes called Empirical Orthogonal Function Analysis (EOF) (e.g., Hotelling 1933; Lorenz 1956; Preisendorfer 1988). The purpose of PCA is to concentrate the internal variation (or variance) within a particular field to the leading components. The first principal component (PC), a function of time, is a linear combination of a given variable over a set of grid points that has maximum possible variance. The coefficients associated with each grid point used in the linear combination are known as the "weighting function", a function of space only. The principal component, a function of time only, is sometimes referred to as the "amplitude". Subsequent PC's can be found under the same maximum variance requirement and under the condition that each weighting function is orthogonal to all previous PC weighting functions. If a data pattern

is proportional to a particular PC's weighting function, then all other PC's will vanish due to the spatial orthogonality. Therefore the weighting functions, often called EOF's in meteorological studies, can be viewed as spatial patterns associated with each PC. It is hoped that with PCA, the leading components (those with the largest variabilities) will represent different physical processes. Also, component truncation of the lowest modes can help delete noise and errors probably associated with small variabilities.

While PCA gives information about the variation within one data field, it offers no help in determining the relationship between different fields. Canonical Correlation Analysis (CCA) is designed to expose relationships between two fields in terms of their correlation coefficients (Hotelling 1935,1936; Glahn 1968; Prohaska 1976). With CCA the elements of each field are linearly combined to form the canonical components. A pair of spatial patterns, analogous to the EOF's in PCA, is also produced that correspond to each optimized correlation. Because conventional CCA only reveals maximum correlations between two fields without regard to variance significance, low order mode truncation using principal components is often recommended before CCA is carried out (Barnett and Preisendorfer 1987). False relationships due to highly correlated, low variability noise and errors are thus avoided.

The MCCA method is a generalization of the two field CCA to multiple fields (Chen et al. 1994). It seeks the optimal correlation among more than two data fields. The technique uses diagonalization of the product or squared product of correlation matrices between selected field pairs in seeking the optimal relationship between the data fields. The resultant canonical components approach the optimal geometrically averaged correlation among the data fields. Because it is unlikely for each correlation matrix to be diagonalized when the number of datasets is more than 2, there are non-zero cross component correlations called "residual correlations" for all selected pairs. If these residual correlations are large when compared to the canonical correlation coefficients, then the solutions obtained by the MCCA are doubtful. Chen and Chang (1994) completed a reliability case study to test the MCCA method and found that it is stable with respect to sampling changes when the data contain significant signals of physical

phenomena and not stable when the data are random.

In this study three spatial domains are used: two small core domains comprised of 255 grid points (15 by 17) imbedded in a large domain comprised of 1125 grid points (25 by 45) (Figs. 1 and 2). The first small domain covers the South China Sea and vicinity: 10°S-25°N, 90°E-130°E. Its choice is based on previous cold surge studies (e.g., Chang and Chen 1992) which show that the South China Sea is the main domain of surge activity. The second small domain covers the East China Sea and vicinity: 5°N-40°N, 110°E-150°E. This domain is chosen to study the eastward propagating baroclinic disturbances that occur during the northern winter surge season. The large domain spans most of the western Pacific and eastern Indian oceans: 20°S-40°N, 70°E-180°E. The MCCA modes are calculated over the small domains using the north-south (v) surface wind component. The structure over the large domain is then determined by single-point correlation and composite analyses with respect to the basic MCC modes. Surface v was chosen as the variable used to compute the modes for two reasons. First, surface data is, in general, more reliable because of the increased availability of observations. The second reason is that the variations in the north-south component of the wind (v) have a stronger signal than the east-west component (u) over our area of study.

Before MCCA is applied, data within the two core domains are first truncated to the first 18 principal components which retain 75% of the total variance for the South China Sea domain and 86% of the total variance for the East China Sea domain. The data is then processed through a 14-day high pass filter so that only phenomena with periods less than 14 days are retained. This filtering is necessary to ensure that the first-guess persistence which may mask signals of interest is removed. The MCCA is then applied to 12 datasets that are constructed by an overlapping sliding time window that contains 12 consecutive v fields. The 12 datasets from 0 h (time T0) to 132 h (time T11) are formed as the window is sliding forward at 12 hourly intervals. Thus, the analysis looks for correlated variations through multiple times (Chen and Chang 1994). The squared product of correlation matrices between fields of adjacent times is then optimized. After transformation matrices from principal components to canonical components are obtained,

spatial patterns of the v field at each time step are computed as weighting functions that convert the canonical components back to the original v field.

At any given time a mode contains both horizontal spatial and time structures, with the latter encompassing 12 consecutive twelve-hourly frames from day 0 to day 5.5. Therefore, the time variation of each mode is a space-time volume function that covers not only the horizontal spatial domain, but also a time domain of 5.5 days. To account for this time domain, a time-integrated amplitude coefficient is produced. This coefficient is the average amplitude of the 12 consecutive twelve-hourly structures and is plotted in the time domain according to the first day (day 0) time frame.

2. Composite and Single-point Correlation Analyses

After the MCC modes have been calculated over the small domains, the results can then be used to study phenomena over the large domain. One method is to use composites. Based on the time-integrated amplitude coefficient time series for a particular mode, a number of specific cases may be picked and then averaged together to give a composite plot. A sequence of composite plots may be produced by picking cases based on a given time lag or lead relative to the first plot time. Composite analysis is a zero-order technique; that is, we observe a mean anomaly pattern that may or may not be representative of any individual case. Because the cases have been selected based on a particular MCC mode, however, it is likely that each case is indeed similar and that the composite does provide a reasonable representation.

Another method of studying the effects of the three dimensional time variability of the basic MCC modes on the large domain is to use single-point correlation. Here the amplitude coefficient time series for a particular mode is correlated with the time series for each grid point in the large domain. Contours are drawn based on the grid point correlation values. A sequence of correlation plots based on different time lags may also be produced. Single-point correlation is a first-order analysis technique. The correlation plots produced give us some idea of how well the MCC mode is represented in the mean-removed data. It is expected that the correlation plot will show a similar spatial pattern

to the MCC mode weighting function for the same variable.

C. DATA FILTERING

As mentioned above, the original principal component data is processed through a 14-day high pass filter before MCCA is applied. Without this filtering, the leading MCCA modes are entirely dominated by long-period persistence that completely masks significant synoptic time scale events. Fig. 3 shows the weighting function of mode 1 when MCC analysis is applied to the East China Sea domain with no filtering. The large, nearly stationary feature depicted is due to a highly correlated, low-frequency background signal in the data field. Persistence in the original data comes from two sources. The first, physical persistence, is simply that component of the data that does not change from one time period to the next. The second source is artificial and is created when a six-hour persistence field is used as a first guess in the tropical GBA dataset. If physical changes occur in the actual field, but are not reflected in the available observation reports, persistence is artificially introduced.

One method of overcoming this problem is to "time-difference" the data before applying MCCA. Fig. 4 shows the weighting functions of mode 1 when MCC analysis is applied to the East China Sea with 24-hourly differenced data:

$$x'(t) = x(t+12 \text{ h}) - x(t-12 \text{ h})$$

Notice that applying time differencing acts like a high pass filter. Although this method is successful in eliminating the persistence problem, it is more difficult to interpret the weighting functions which now show first order acceleration fields rather than zero order velocity fields.

The second method of overcoming this "persistence problem" is to process the original data through a high pass filter prior to analysis. This will eliminate the long period, low frequency persistent components and leave the higher frequency, synoptic-

scale events. Because the events examined in this study occur with a maximum period of about 8 to 9 days, a 14-day high pass filter was chosen.

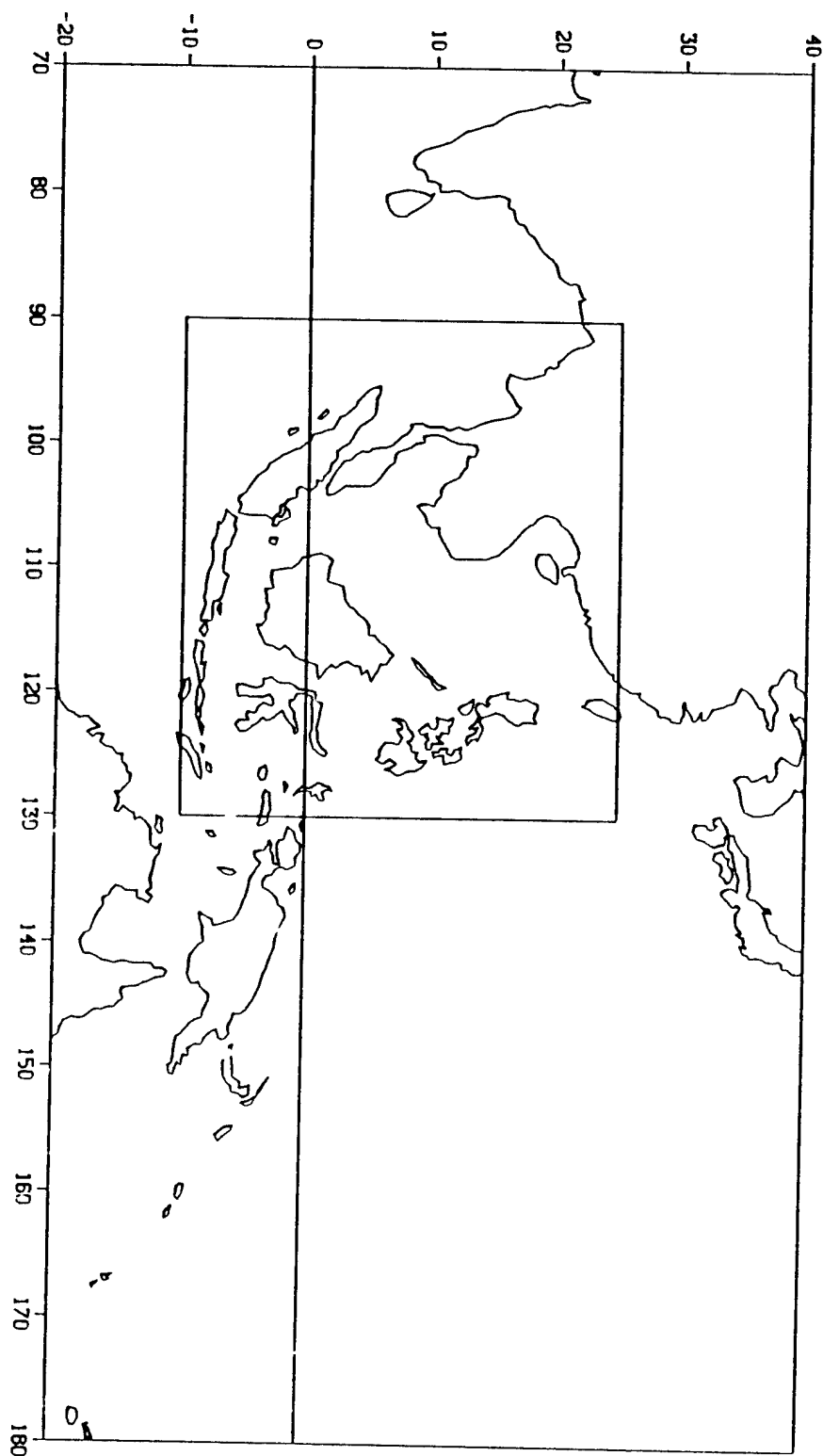


Figure 1. Map showing the core South China Sea domain imbedded in the large western Pacific and eastern Indian ocean domain.

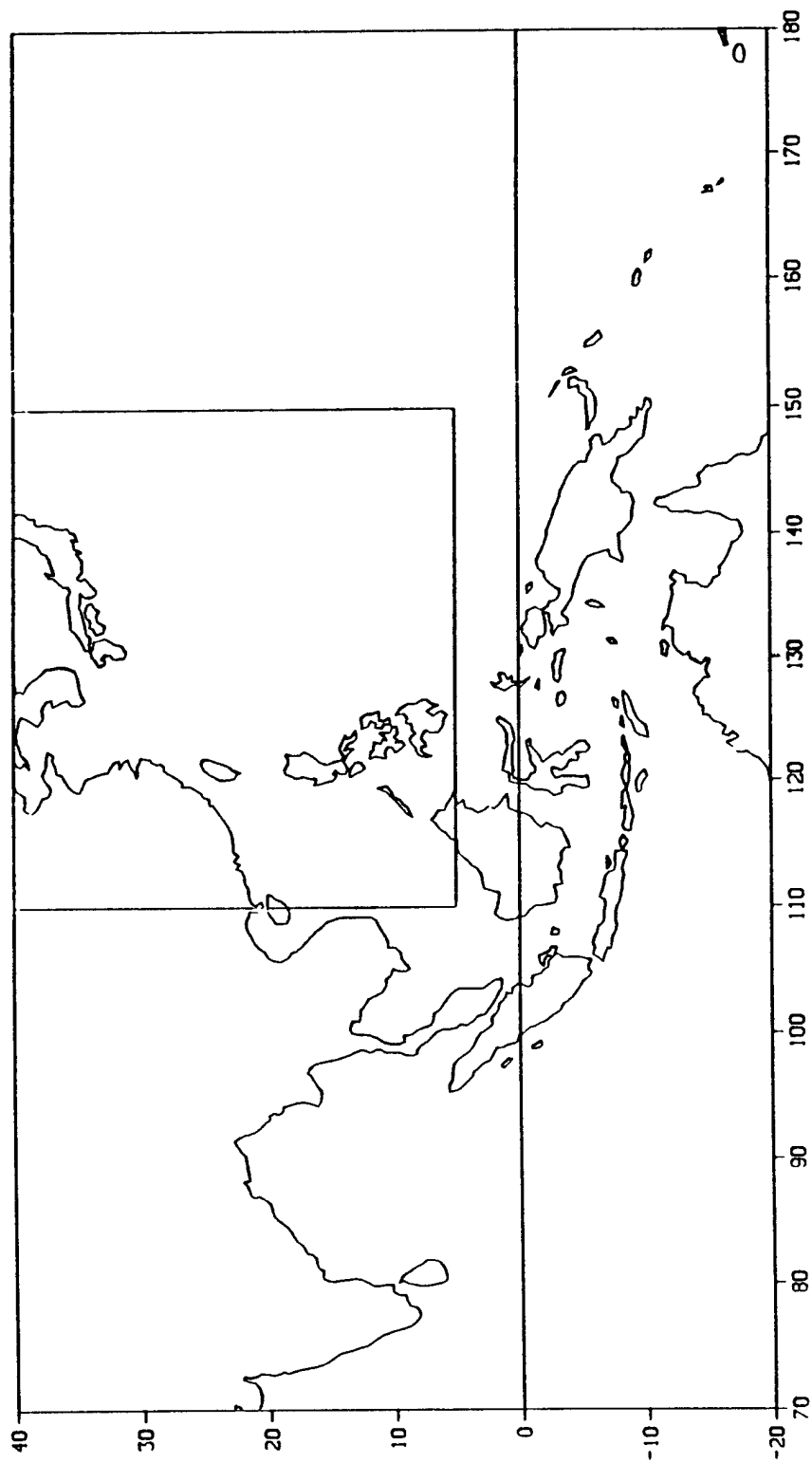


Figure 2. Map showing the core East China Sea domain imbedded in the large western Pacific and eastern Indian ocean domain.

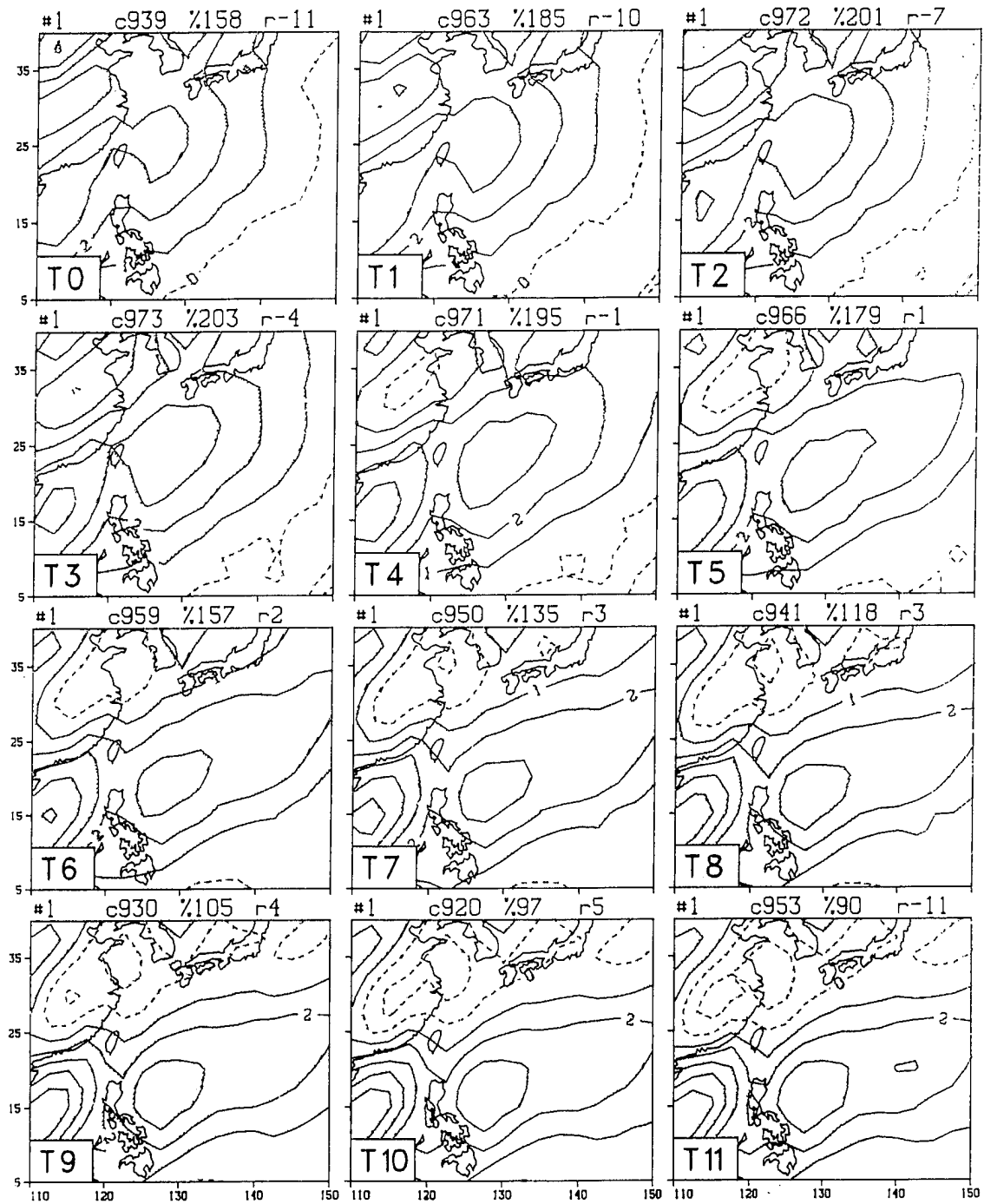


Figure 3. Weighting function for MCC mode 1, East China Sea domain, of the surface meridional winds (v) for 12 consecutive twelve-hourly frames from 00h (T0) to 132h (T11). Contour interval is 0.03 and dashed lines correspond to northerly winds when MCC mode 1 amplitude is positive. No prior filtering was applied to the data.

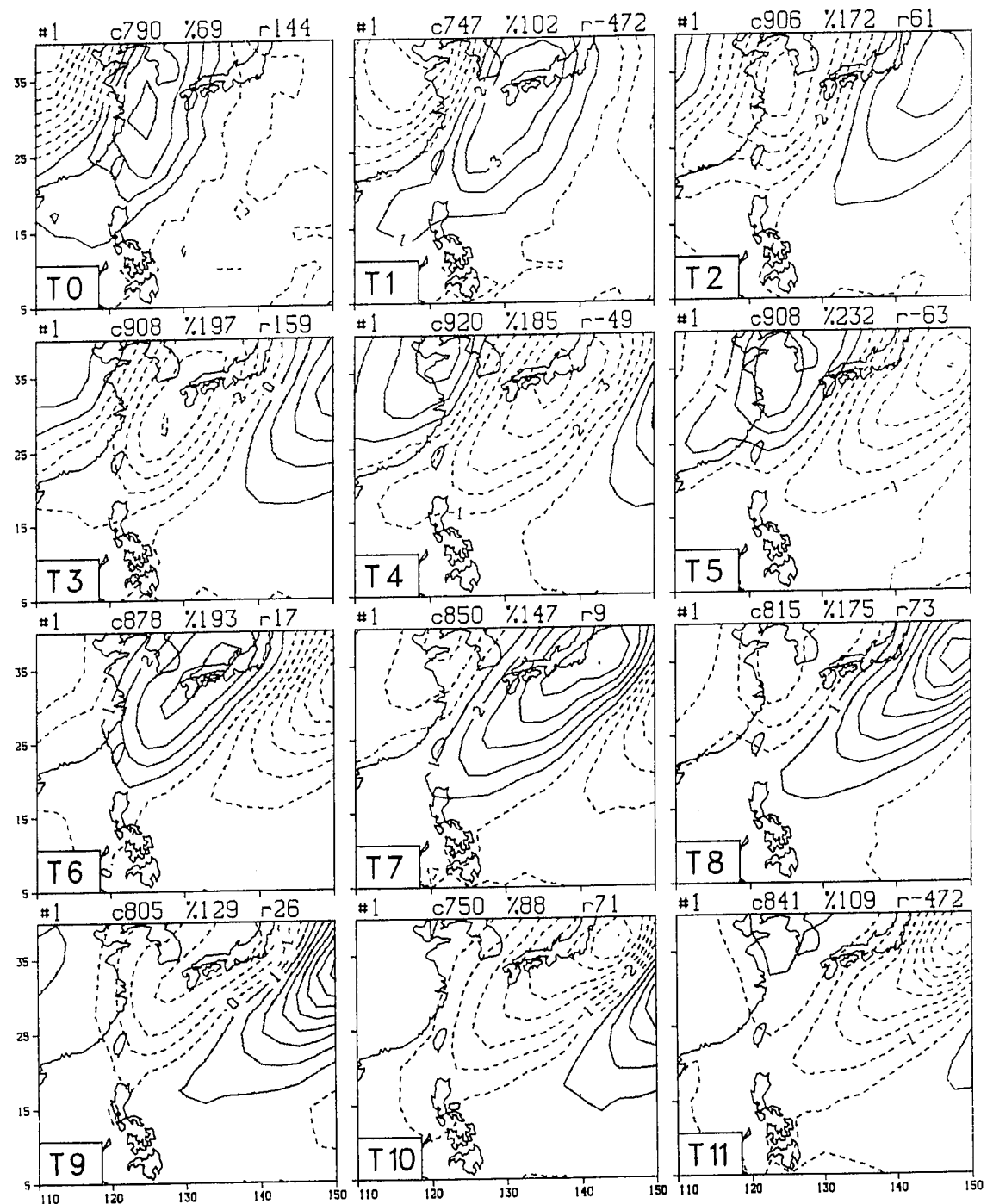


Figure 4. Same as Fig. 3 except the data was time-differenced over a 24 hour period prior to analysis.

III. LEADING MCC MODES BASED ON SURFACE v

A. THE SOUTH CHINA SEA DOMAIN

The weighting functions for MCC modes 1 and 2 derived from the surface v wind component are shown in Figs. 5 and 6, respectively. Each figure shows the structure of the surface v anomaly (mean removed) for 12 consecutive twelve-hourly time frames from 0 h (T0) to 132 h (T11) (5 1/2 days). For MCC mode 1 the average correlation between adjacent times is 0.82, with an average fractional variance of 21.2 % and a maximum residual correlation of 0.14. Recall that the smallness of the residual value compared to the average correlation value indicates that the solution is reliable (Chen and Chang 1994). For MCC mode 2 the average correlation is 0.80 with an average fractional variance of 20.1% and a maximum residual correlation of 0.14. A lag correlation between modes 1 and 2 was also calculated and the results shown in Fig. 7. The lag correlation plot indicates that modes 1 and 2 are a pair. At a time lag of about 3.0 (1 1/2 days) the correlation between the two modes is approximately 0.8. We can thus conclude that modes 1 and 2 show basically the same phenomena and differ only by a phase shift. This can also be seen by noting the similarity of the weighting function patterns for modes 1 and 2. The average fractional variance for the combined modes 1 and 2 then is 41.3%. The associated amplitude coefficient time series and power spectra for modes 1 and 2 are shown for each year in Figs. 8 through 14.

The weighting function pattern for mode 1, time T0, is characterized by two large-scale areas: a positive area centered near 25°N, 103°E that covers most of the Indochina peninsula and a broader negative area centered north of Taiwan that covers the northern half of the South China Sea. While the positive center descends only very slightly southward to near northern Thailand and weakens through time T5, the negative area propagates more rapidly and splits into two centers. A tight gradient over the Indochina peninsula is established between the positive and negative areas. This gradient may be due in part to the fact that the GBA surface data used in this study are not

discriminant of elevation so that observations taken over mountainous regions may have a stronger bias compared to sea-level observations. After the broad negative area splits, one center moves southward into the southern South China Sea while the other moves southeastward into the Philippine Sea. This pattern of propagation continues from times T6 through T11 in almost the exact same fashion as just described, but with areas of opposite sign. This indicates that the apparent "surge" we see moves rather like a wave that begins in the north and dissipates in the south and not an intrusion from the north that advances and then retreats. Notice that the pattern at time T11 is almost exactly the opposite of that at time T3. This indicates a half cycle of about 4 days, so that the total period of the event would be about 8 days. Indeed, the average power spectrum for all 13 years, modes 1 and 2 combined, confirms that the broad period spectral maximum is in a window between 6 and 12 days with a small peak at about 8 days (Fig. 15). Table 1 is a summary of the spectral peaks for each year. While there are year to year variations, the peaks generally stay within the 6-12 day window and most frequently occur at 8 days.

Lower order modes (modes 3, 4, etc.) were also calculated for the South China Sea domain, but because they each contribute so little to the total variance, they are not included in this study.

B. THE EAST CHINA SEA DOMAIN

1. Modes 1 and 2

The weighting function for MCC modes 1 and 2 derived from the surface v wind component over the East China Sea domain are given in Figs. 16 and 17, respectively. As before, the patterns show the structure of the surface v anomaly for 12 consecutive twelve-hourly time frames from 0 h (T0) to 132 h (T11). For mode 1 the average correlation between adjacent times is 0.86, with an average fractional variance of 11.3% and a maximum residual correlation of 0.22. For mode 2 the average correlation between adjacent times is 0.86, with an average fractional variance of 11.9% and a maximum

YEAR	PERIOD (DAYS)		
	10-12	8	6
1975	L		
1976			M
1977	This year not included due to erroneous data		
1978	L		
1979		L	
1980		L	
1981		S	
1982		S	
1983		S	S
1984			L
1985		L	
1986		M	M
1987			M
1988		M	

L= peak is large relative to other years
 M= peak is moderate relative to other years
 S= peak is small relative to other years

Table 1: Significant power spectrum peaks for the South China Sea modes 1 and 2

residual correlation of 0.20. As with the South China Sea domain, MCC modes 1 and 2 are a pair, differing only by a phase shift. This is verified upon examination of the lag correlation plot between the two modes (Fig. 18) which shows a correlation value of about 0.85 at a time lag of about 3.5 (1 3/4 days). The two modes together then account for approximately 23.2% of the total variance of the 14-day filtered data. Again, the centers of the anomalies lie in a band anywhere between the latitudes 25° N and 40° N which indicates that MCC modes 1 and 2 here probably represent the typical observed wintertime baroclinic waves of the western Pacific. The amplitude coefficient time series for modes 1 and 2 along with their power spectra for each year are shown in Figs. 19 through 25.

The weighting function patterns for MCC modes 1 and 2 show large anomalies with horizontal wavelengths on the order of 3000 to 4000 km. The anomalies have a northeast to southwest horizontal tilt and move from west to east with a period of about 7-8 days. The average power spectrum for all 14 years, modes 1 and 2 combined, is strongest between 6 and 12 days with a significant peak at about 8 days (Fig. 26). Table 2 is a summary of the spectral peaks for each year. Again there are year to year variations, but the peaks generally fall within the 6-12 day window and most frequently at about 8 days.

The horizontal spatial and time scales represented in modes 1 and 2 for the East China Sea domain look very similar to those in the South China Sea domain. Therefore, although calculated over different spatial domains, both pairs of modes probably are manifestations of the same event. To confirm this, coherence and phase calculations were carried out between the two pairs' amplitude coefficient time series (Fig. 27). Significant coherence values that range between about 0.65 and 0.80 are found for the 6 to 12 day period. The transfer function phase over this same period is nearly out of phase throughout the frequency domain. One may conclude then that the two mode pairs are essentially the same, except that the patterns isolated are out of phase. Therefore, only MCC mode 1 for the South China Sea domain will be studied.

YEAR	PERIOD (DAYS)		
	10-12	8	6
1975	L		
1976		M	M
1977		L	
1978	L		
1979	L	L	
1980		L	
1981		M	
1982		L	
1983	M	M	
1984			L
1985		L	
1986			M
1987			L
1988		L	

L= peak is large relative to other years
 M= peak is moderate relative to other years
 S= peak is small relative to other years

Table 2: Significant power spectrum peaks for the East China Sea modes 1 and 2

2. Modes 3 and 4

Unlike the South China Sea domain, MCC modes 3 and 4 for the East China Sea domain contain a significant percentage of the total variance. The weighting functions are given in Figs. 28 and 29, respectively. The associated amplitude coefficient time series and power spectrum plots for each year are given in Figs. 30 through 36. Because the phenomenon isolated in modes 3 and 4 is well correlated over a shorter time period, a 6-frame (2.5 days) overlapping sliding window was used. For mode 3 the average correlation between adjacent times is 0.79, with an average fractional variance of 9.8% and a maximum residual correlation of 0.14. For mode 4 the average correlation between adjacent times is 0.73, with an average fractional variance of 6.2% and a maximum residual correlation of 0.27. Examination of the lag correlation plots given in Fig. 37 reveals that modes 3 and 4, like modes 1 and 2, are a pair with a correlation value of about 0.8 at about 2.0 time intervals (1 day). As a pair, modes 3 and 4 account for 16% of the total variance of the 14-day filtered data. The plots also show that the two mode pairs isolate separate events; correlation values between the two pairs are low (between modes 1 and 3 for example).

The weighting function patterns for MCC modes 3 and 4 are characterized by elongated anomalies that tilt from northeast to southwest and have horizontal wavelengths on the order of 1500 to 2000 km. The centers of the anomalies lie in a band of latitudes between 20 N and 40 N and move to the east-northeast with a period of about 3 days. In general, the weighting functions for this pair of modes looks somewhat similar to those of the modes 1 and 2 in that they all show eastward propagating wave patterns. The primary difference appears to be in the spatial and temporal scales both of which are smaller for the mode 3 and 4 pair. Table 3 provides a summary of the significant spectral peaks for each year. Every year has a peak within a 2-4 day window, with most occurring right at 3 days. A few years also have peaks at longer periods. Comparison of the average power spectrum plot for modes 3 and 4 (Fig. 38) with that of modes 1 and 2 (Fig. 26) reveals that the longer time scale events of modes 1 and 2 and the shorter time scale events of modes 3 and 4 do not overlap. There is a spectral gap between 4 and 6 days.

YEAR	PERIOD (DAYS)		
	8	6	3
1975			L
1976			L
1977	M		M
1978			M
1979			L
1980	S	S	S
1981			S
1982			S
1983	S		S
1984			L
1985	S		S
1986			M
1987			M
1988	S		S

L= peak is large relative to other years
 M= peak is moderate relative to other years
 S= peak is small relative to other years

Table 3: Significant power spectrum peaks for the East China Sea modes 3 and 4

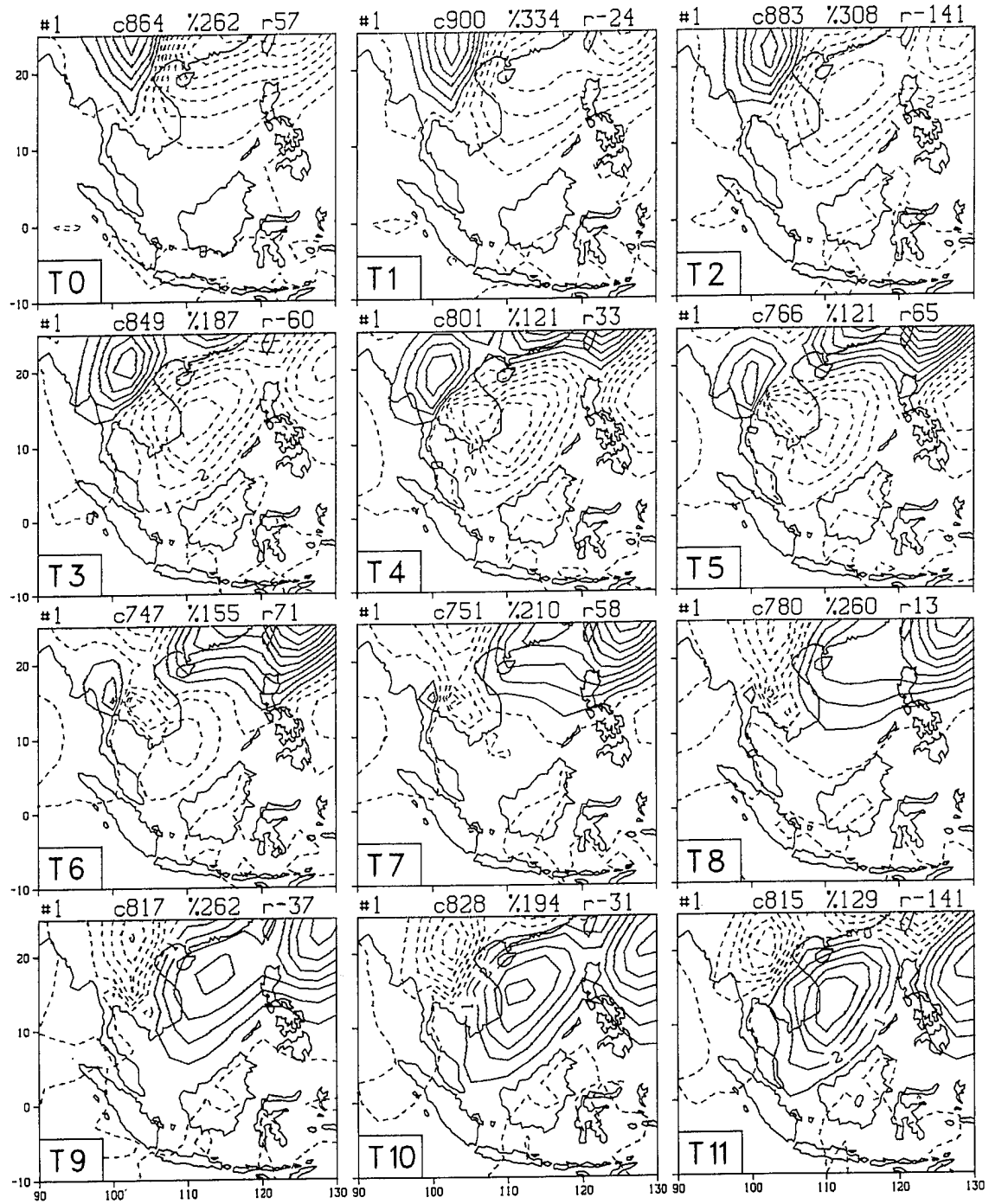


Figure 5. Weighting function for MCC mode 1, South China Sea domain, of the surface meridional wind (v) for 12 consecutive twelve-hourly frames from 00h (T0) to 132h (T11). Contour interval is 0.03 and dashed lines correspond to northerly winds when MCC mode 1 is positive. Data was passed through a 14-day high pass filter prior to analysis.

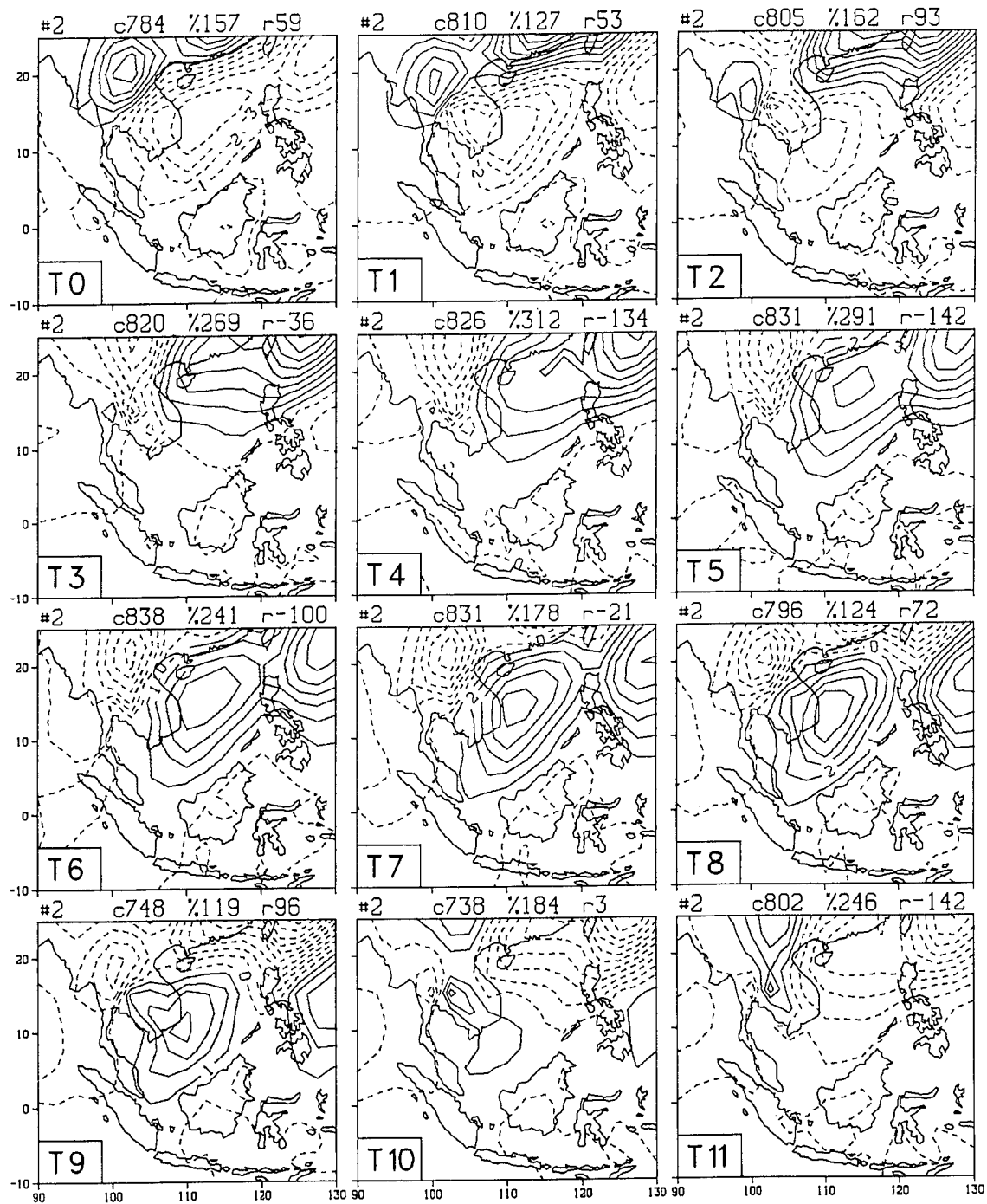


Figure 6. Same as Fig. 5 except for MCC mode 2.

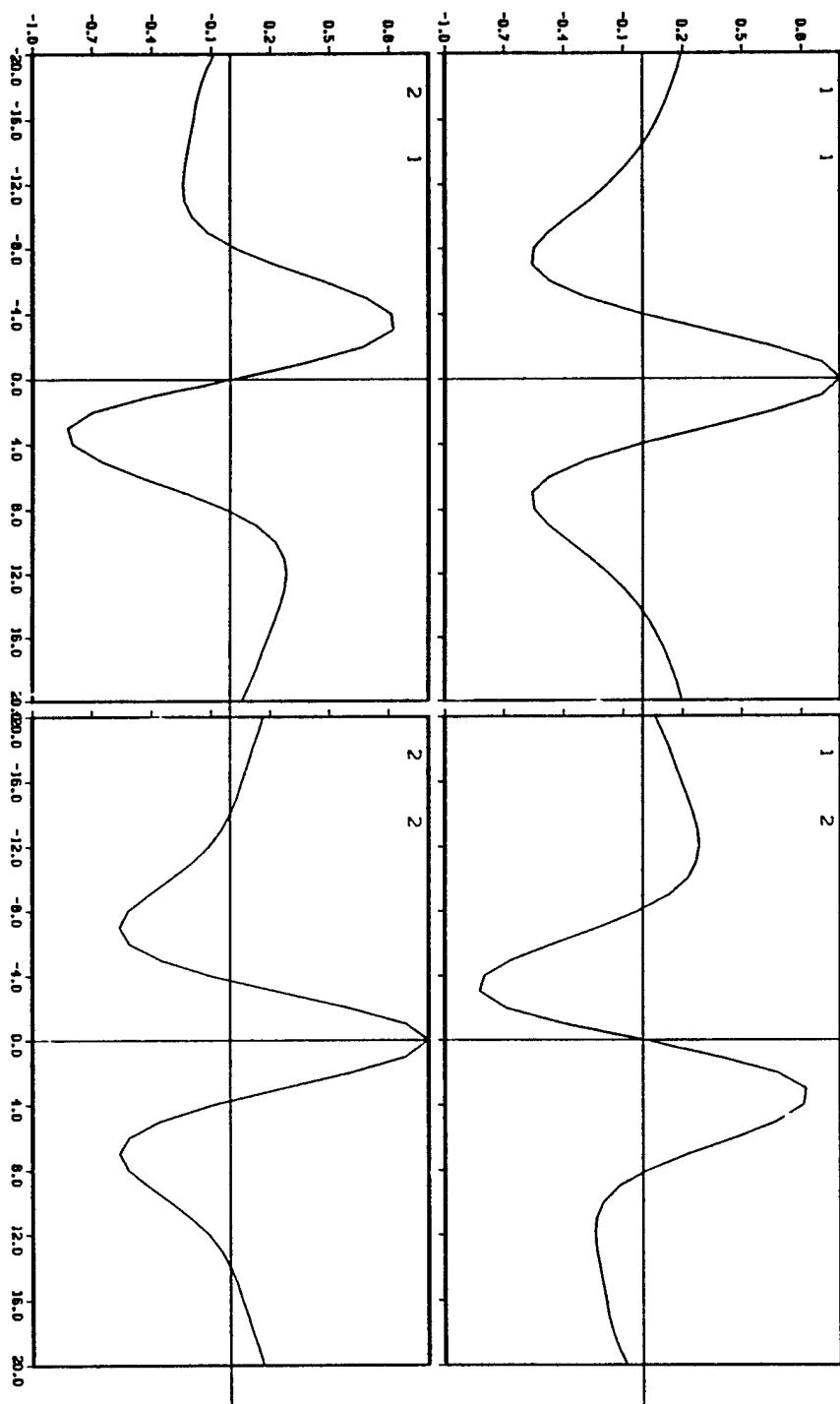


Figure 7. Lag-correlation plots for MCC modes 1 and 2, South China Sea domain. The two modes correlated in each plot are labeled in the upper left corners. Each interval on the x-axis represents 2.0 days (4*12h).

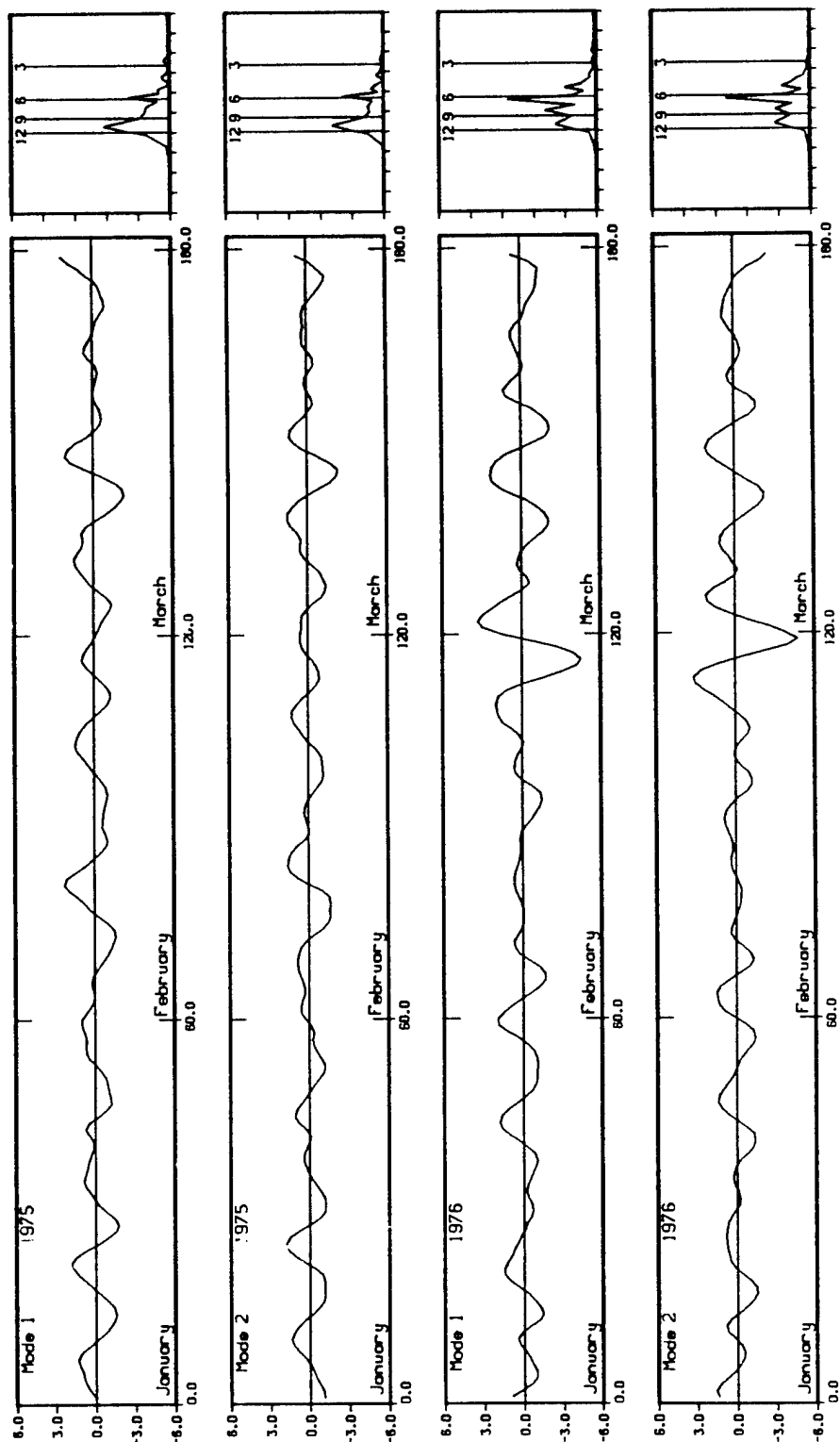


Figure 8. Time series of the time-integrated amplitude coefficients of MCC modes 1 and 2, South China Sea domain, for the winters 1975 and 1976. The power spectrum for each time series is shown at the right with the 3, 6, 9, and 12 day periods labeled.

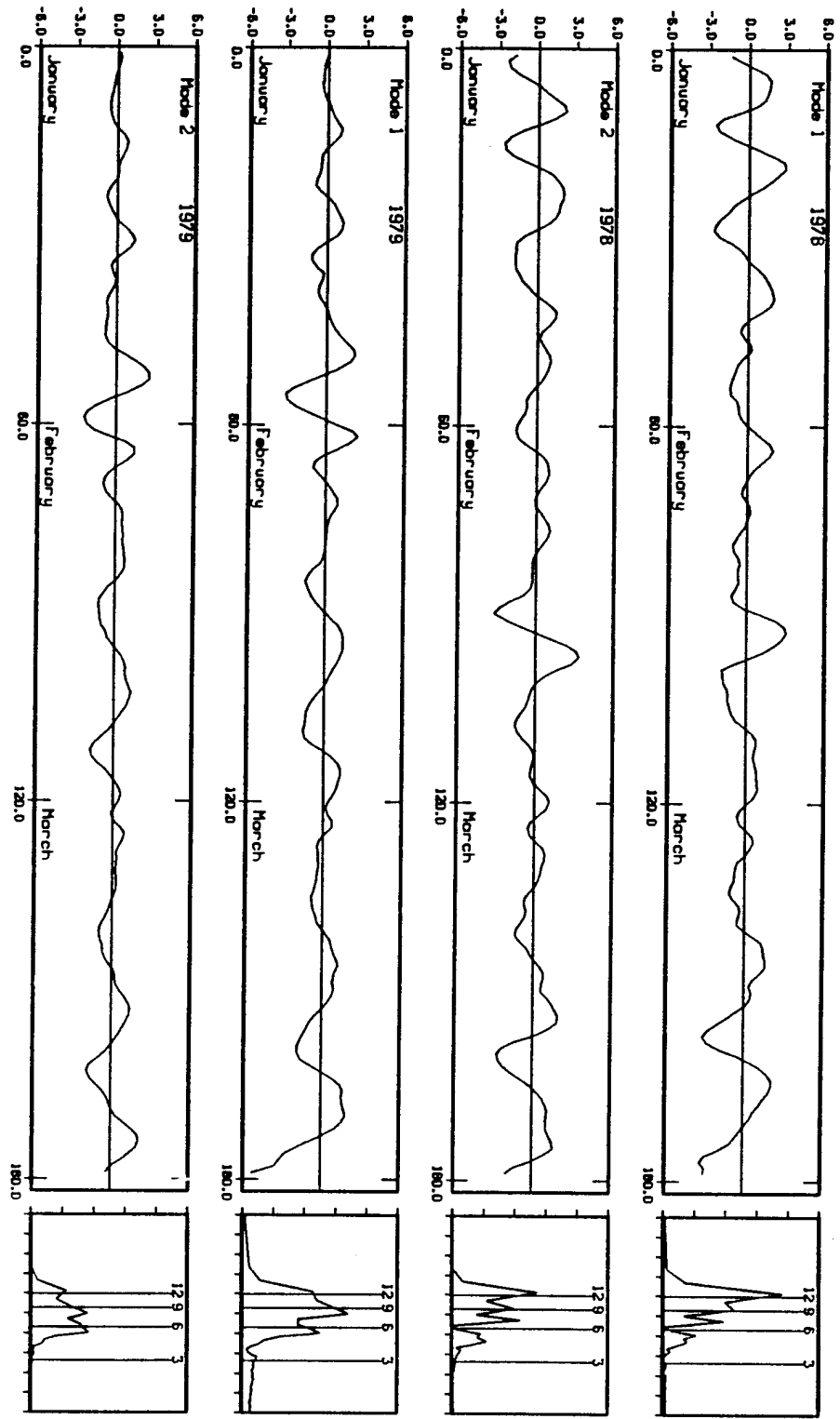


Figure 9. Same as Fig. 8 except for winters 1978 and 1979.

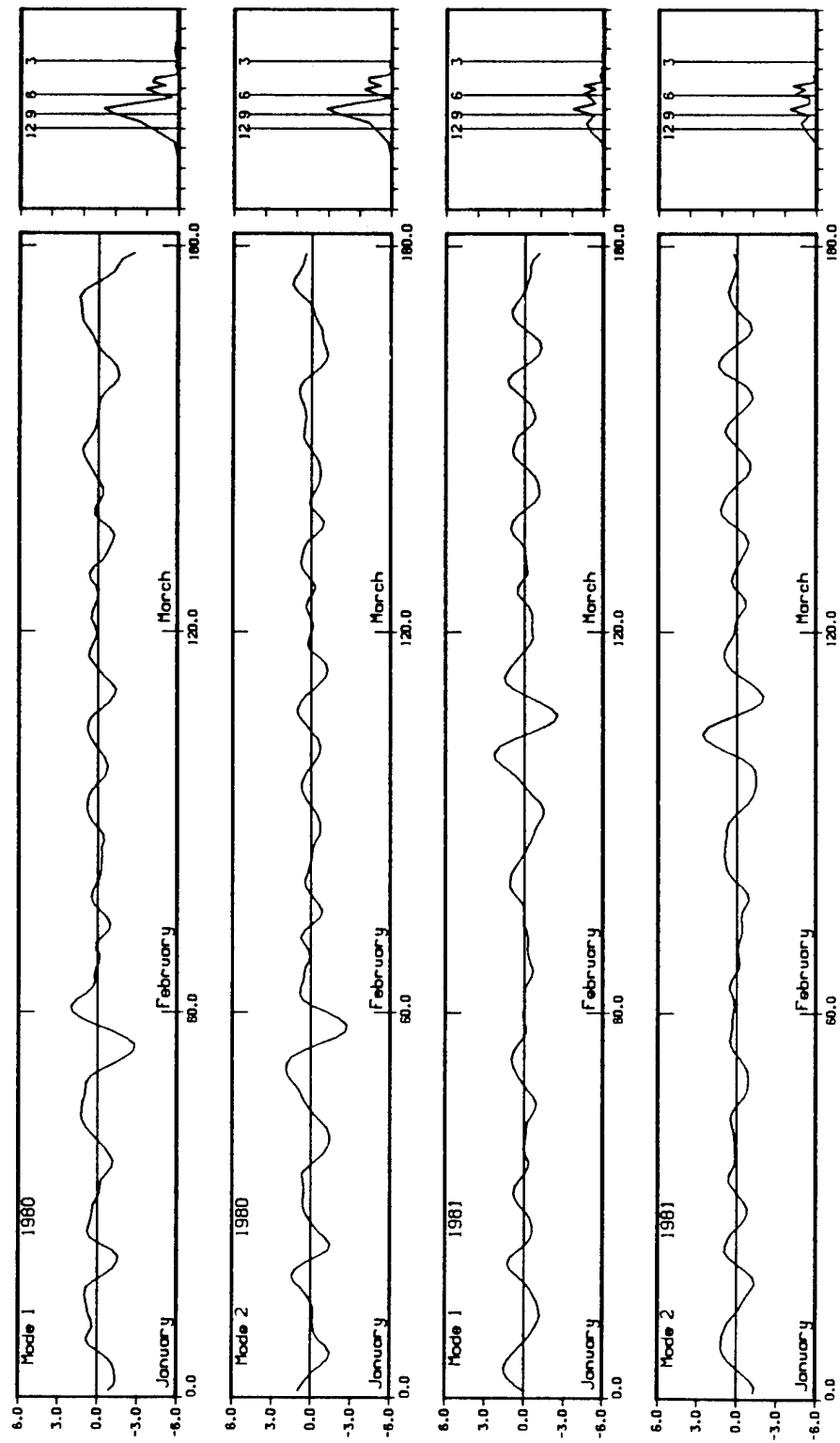


Figure 10. Same as Fig. 8 except for winters 1980 and 1981.

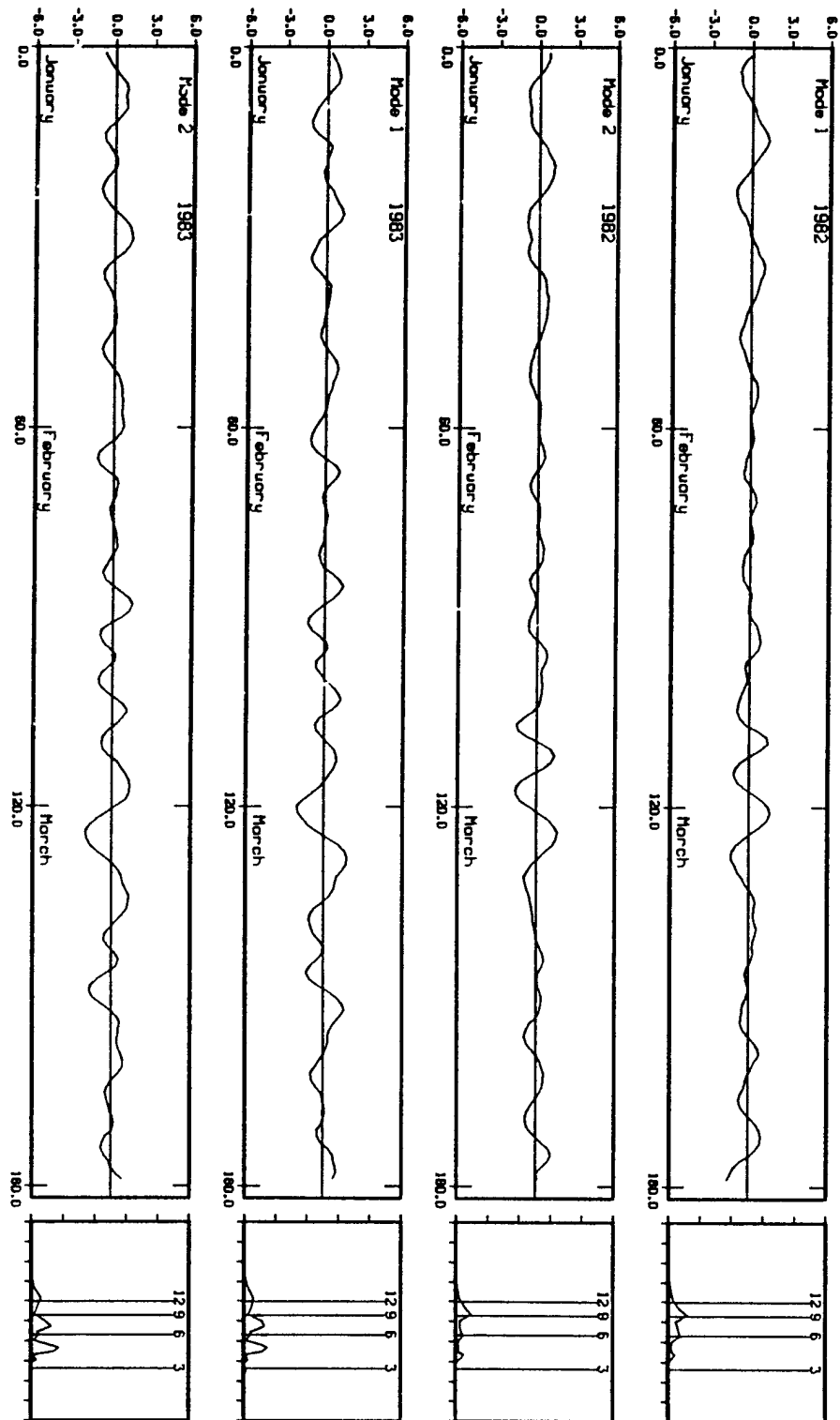


Figure 11. Same as Fig. 8 except for winters 1982 and 1983.

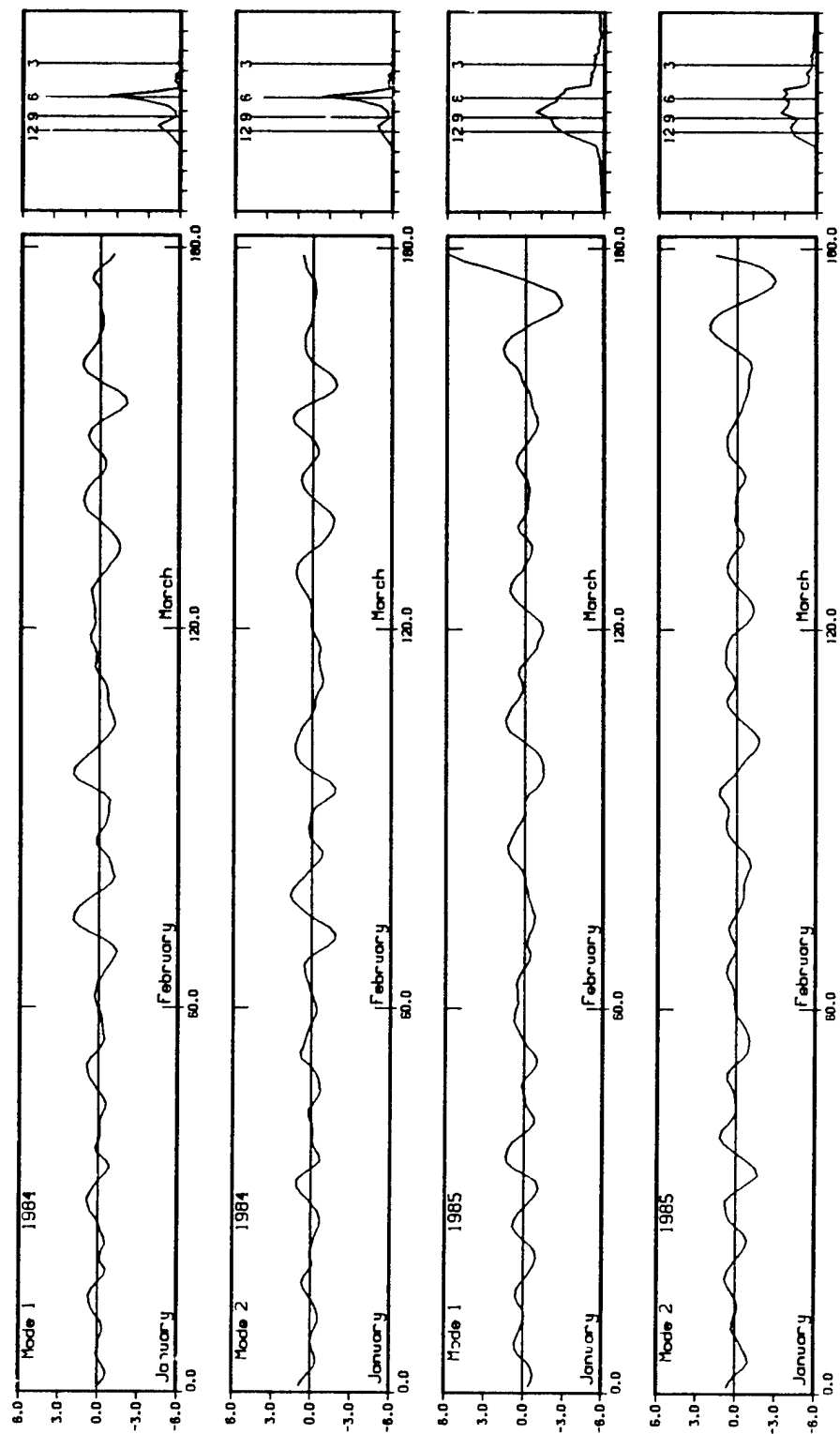


Figure 12. Same as Fig. 8 except for winters 1984 and 1985.

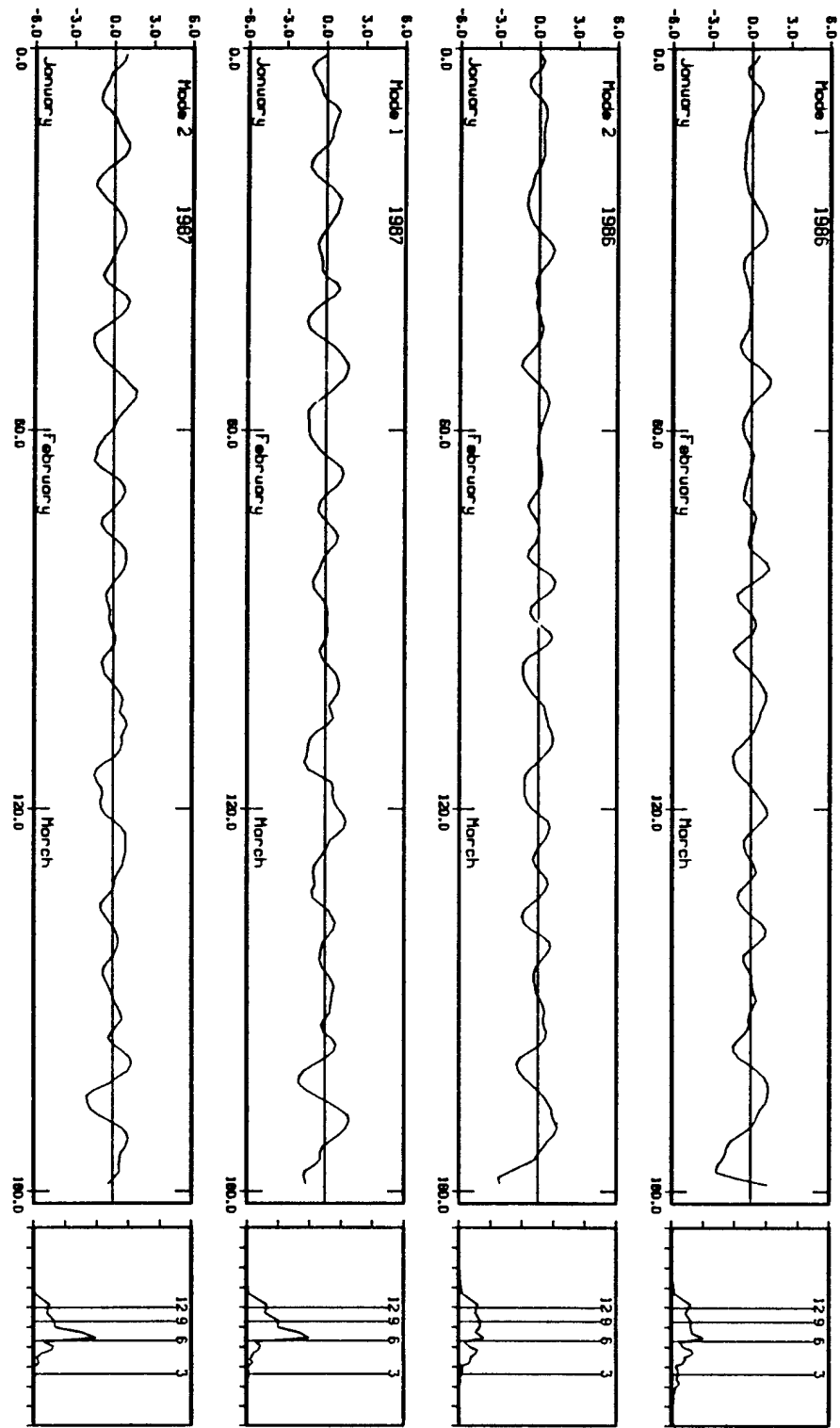


Figure 13. Same as Fig. 8 except for winters 1986 and 1987.

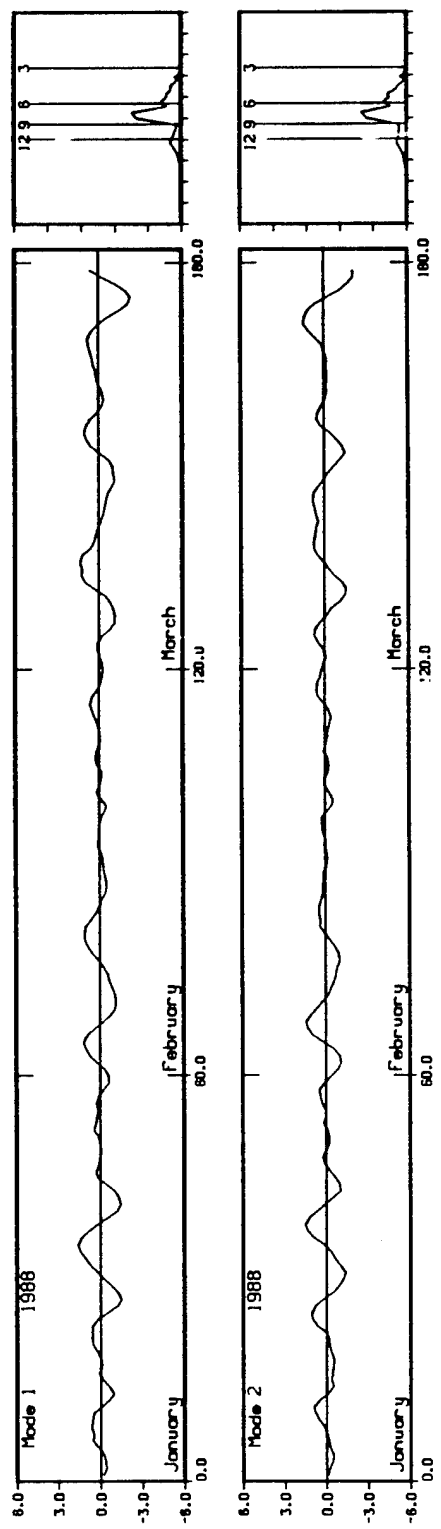


Figure 14. Same as Fig. 8 except for winter 1988.

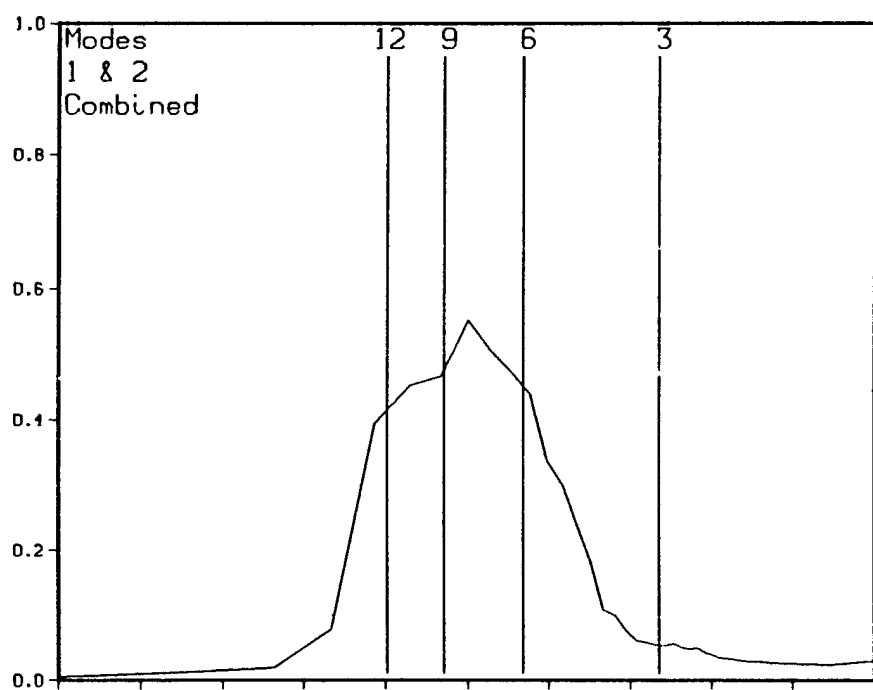


Figure 15. Average power spectrum for 13 winters, MCC modes 1 and 2 combined, South China Sea domain, with the 6, 9, and 12 day periods labeled.

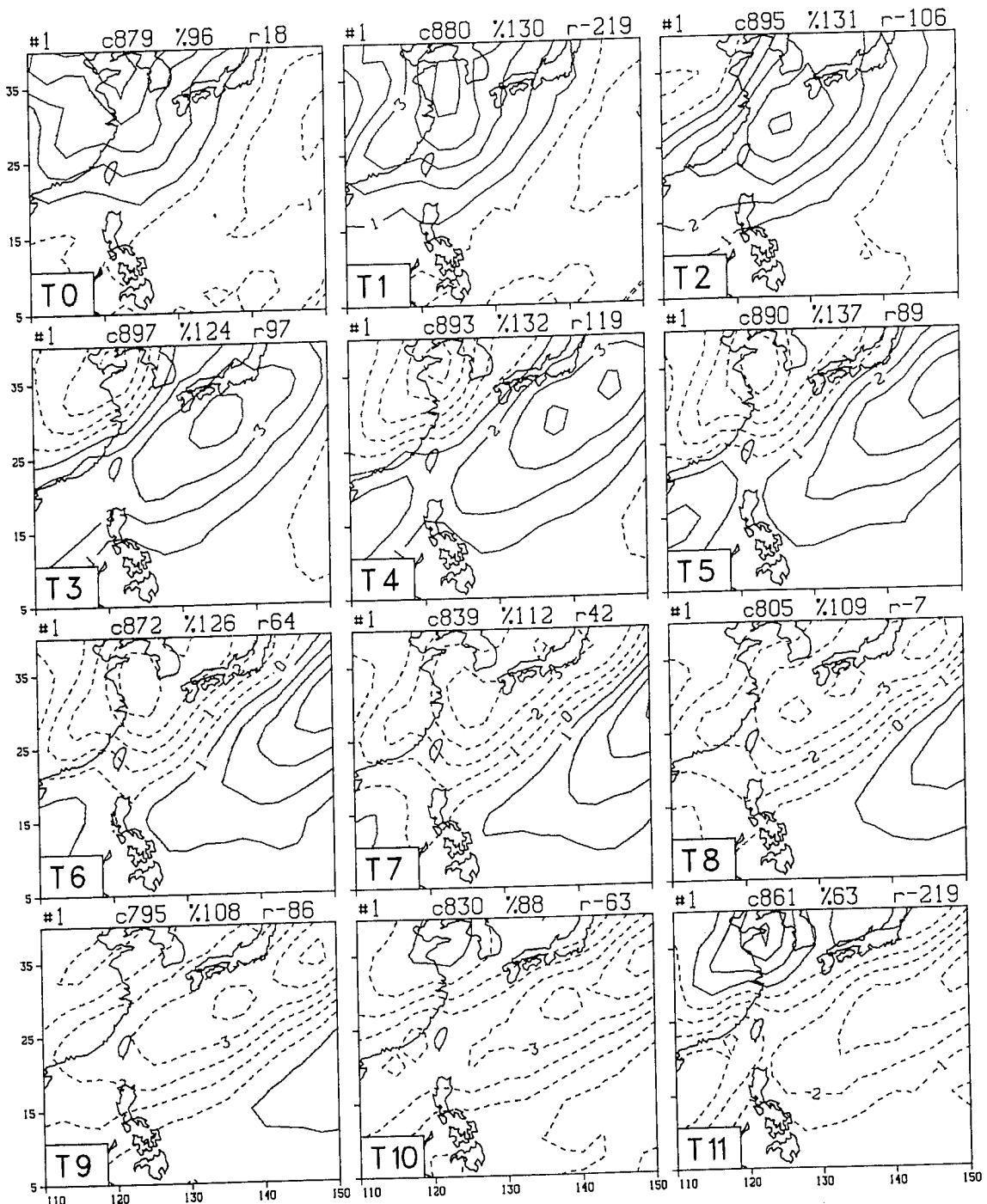


Figure 16. Weighting function for MCC mode 1, East China Sea domain, of the surface meridional wind (v) for 12 consecutive twelve-hourly frames from 00h (T0) to 132h (T11). Contour interval is 0.03 and dashed lines correspond to northerly winds when MCC mode 1 amplitude is positive. Data was passed through a 14-day high pass filter prior to analysis.

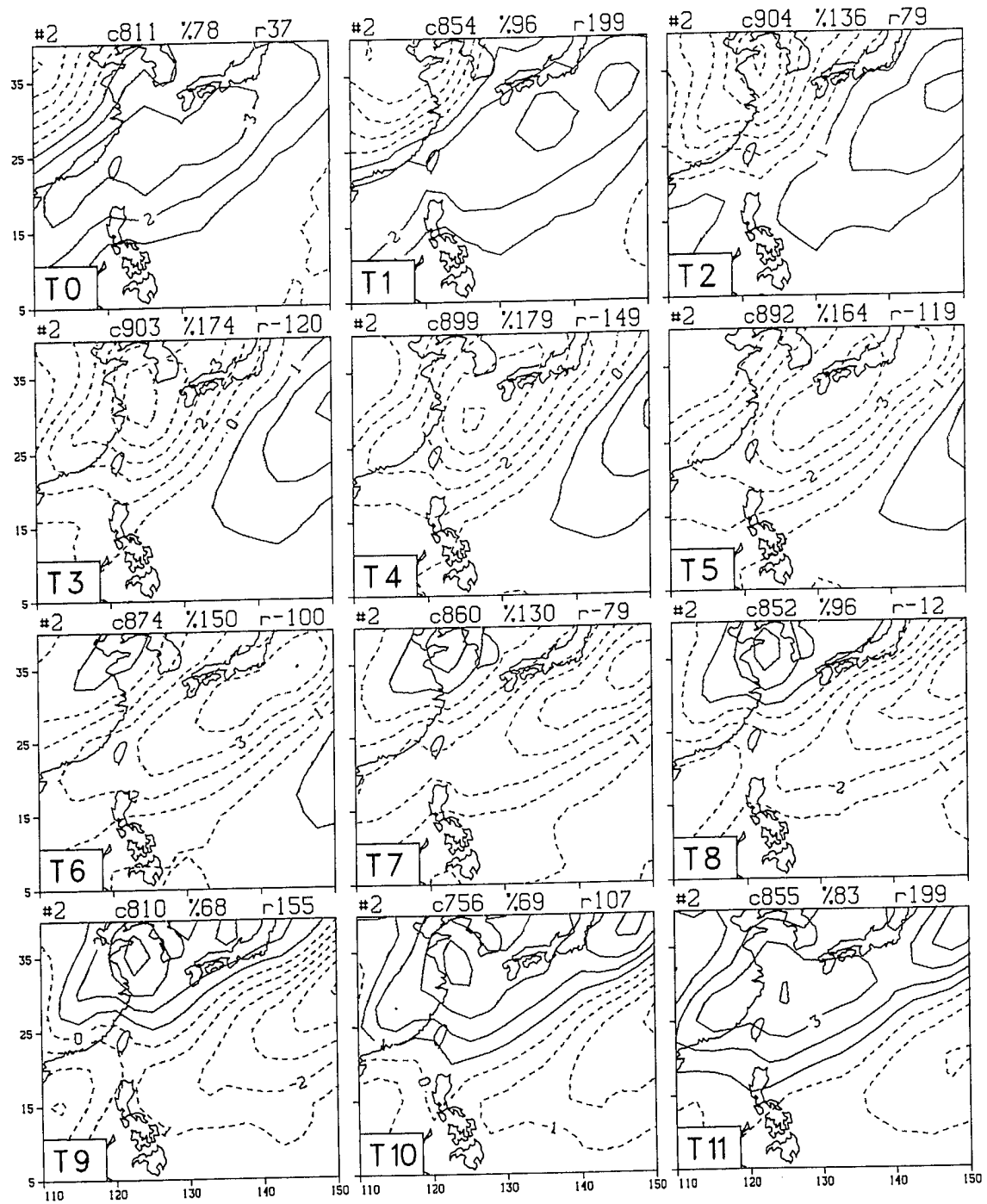


Figure 17. Same as Fig. 16 except for MCC mode 2.

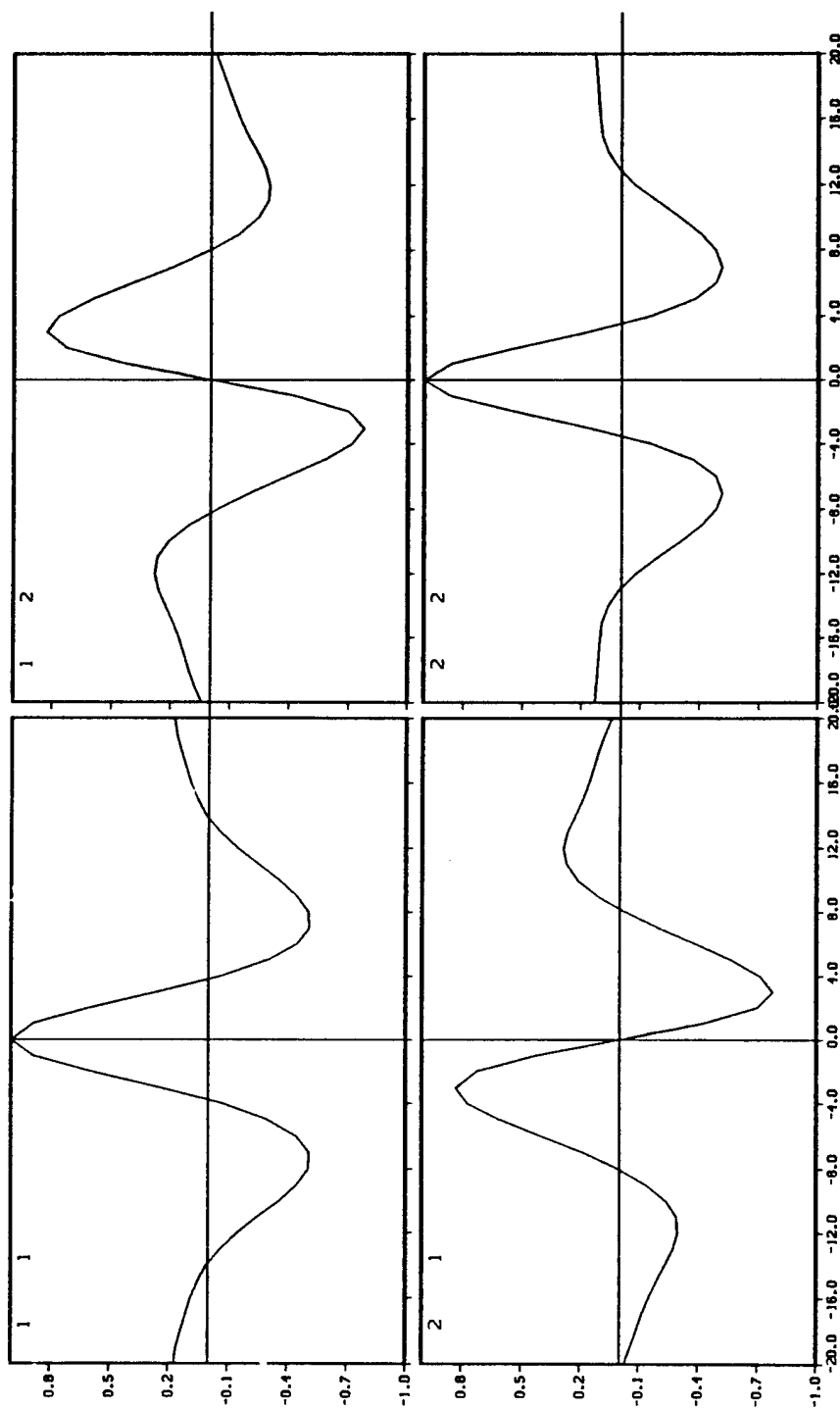


Figure 18. Lag correlation plots for MCC modes 1 and 2, East China Sea domain. The two modes correlated in each plot are labeled in the upper left corners. Each interval on the x-axis represents 2.0 days (4*12h).

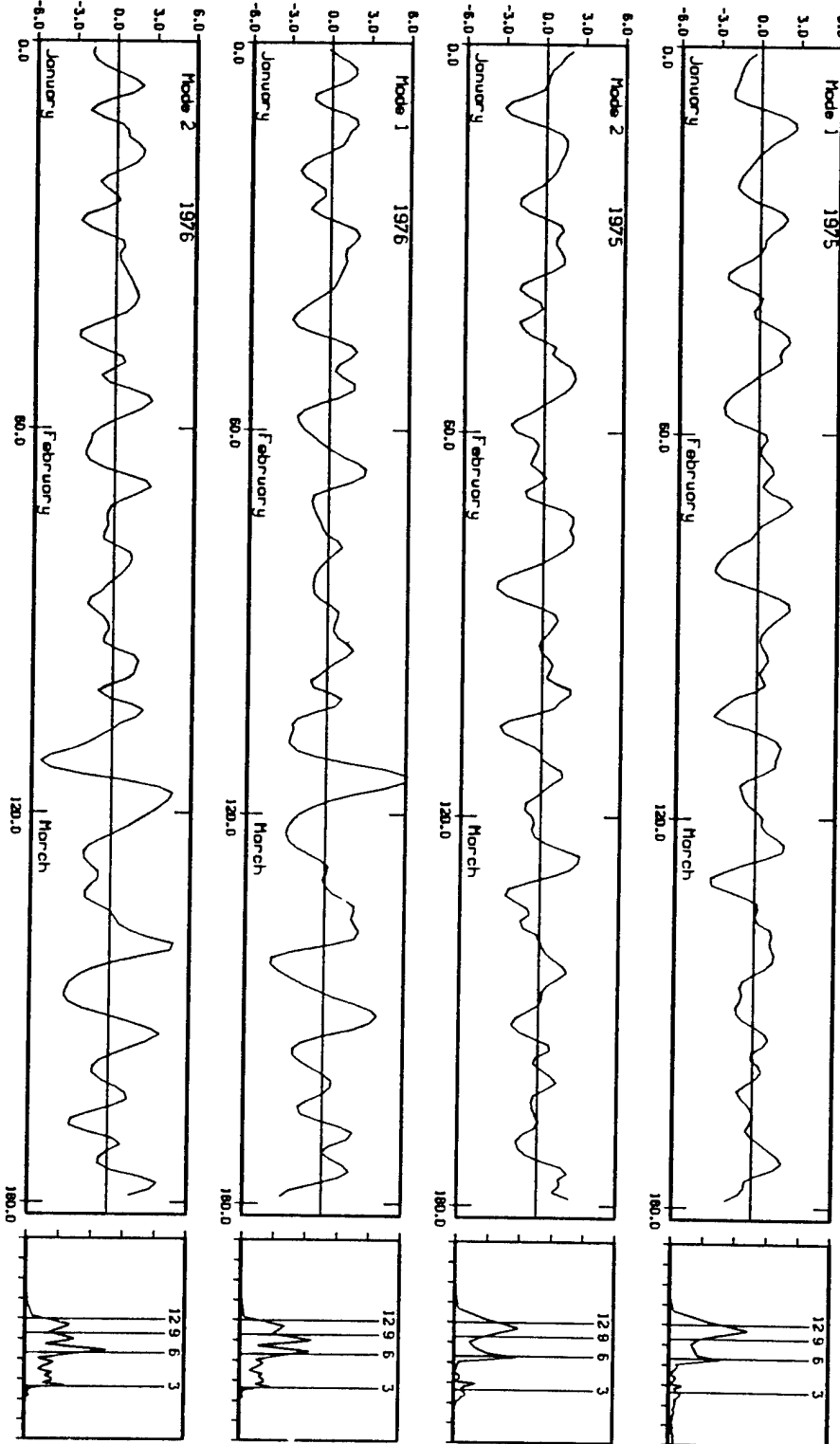


Figure 19. Time series of the time-integrated amplitude coefficients of MCC modes 1 and 2, East China Sea domain, for the winters 1975 and 1976. The power spectrum for each time series is shown at the right with the 3, 6, 9, and 12 day periods labeled.

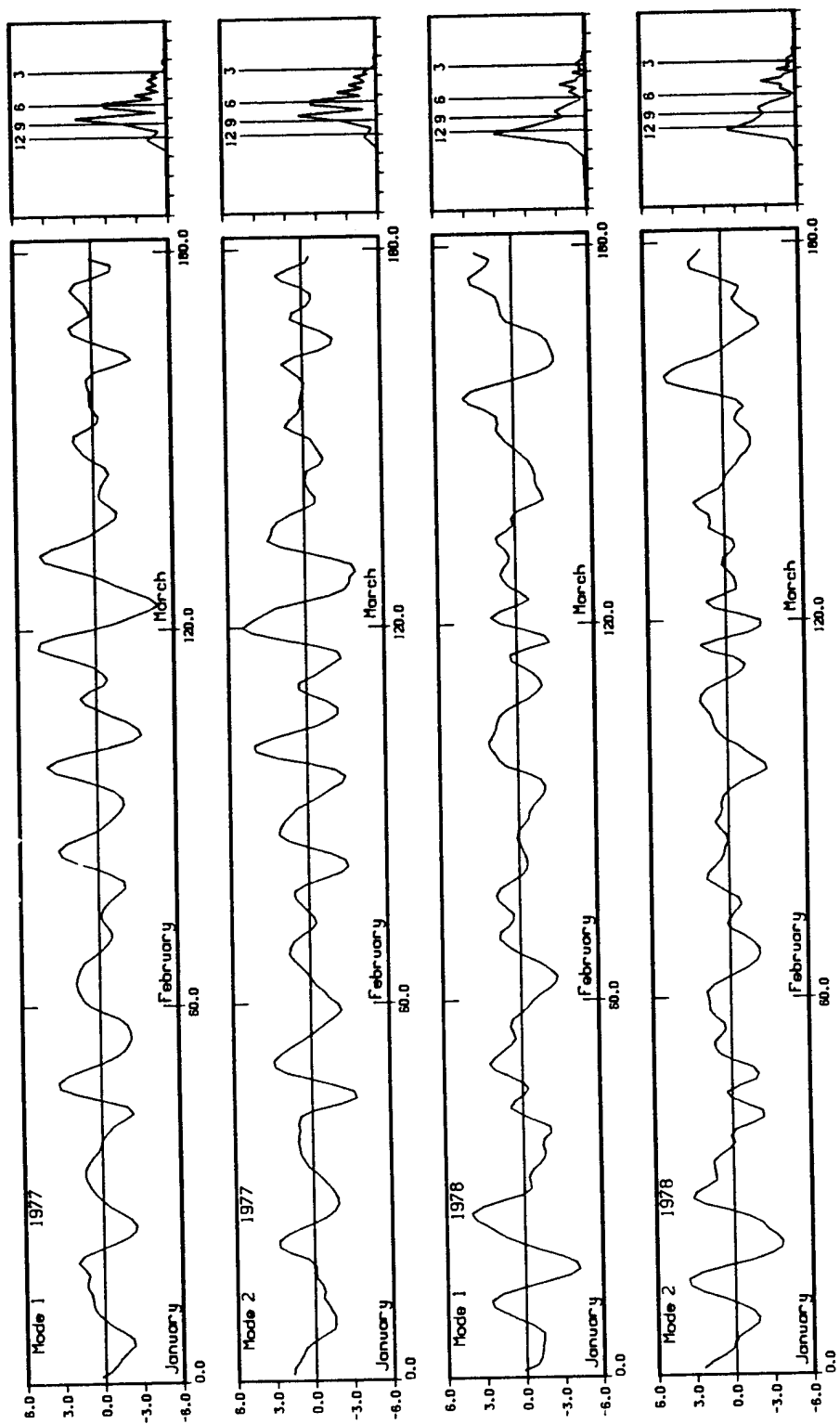


Figure 20. Same as Fig. 19 except for winters 1977 and 1978.

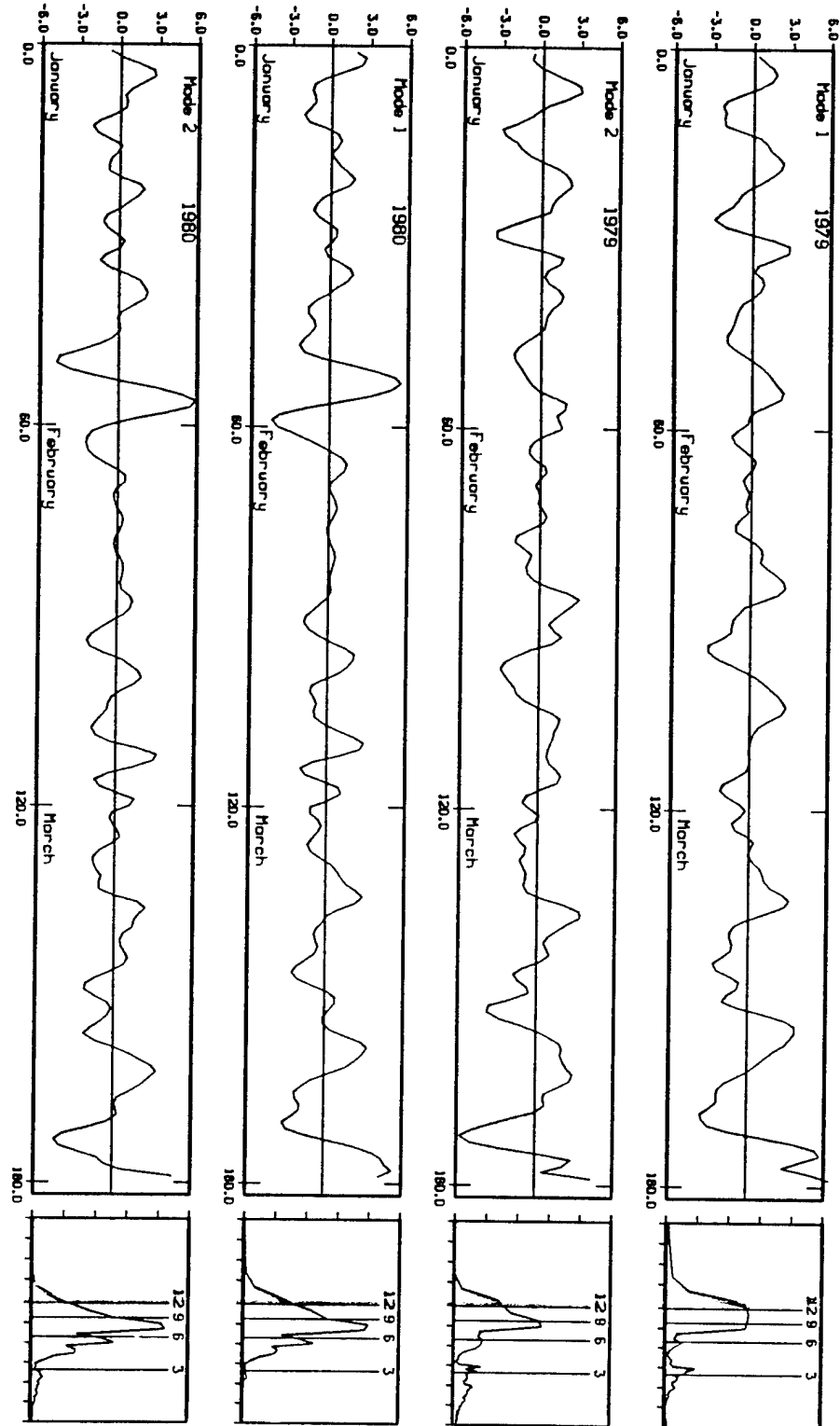


Figure 21. Same as Fig. 19 except for winters 1979 and 1980.

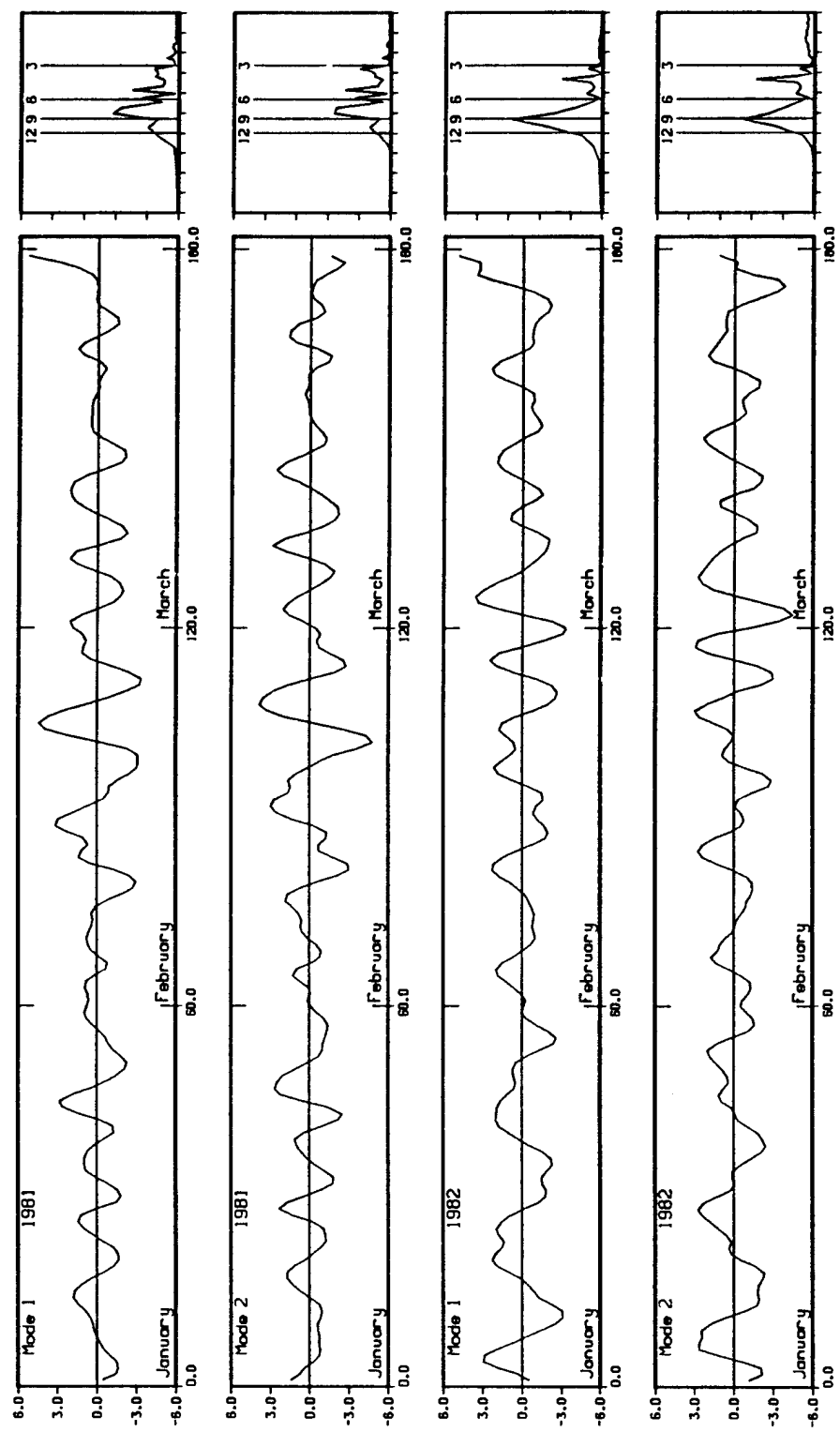


Figure 22. Same as Fig. 19 except for winters 1981 and 1982.

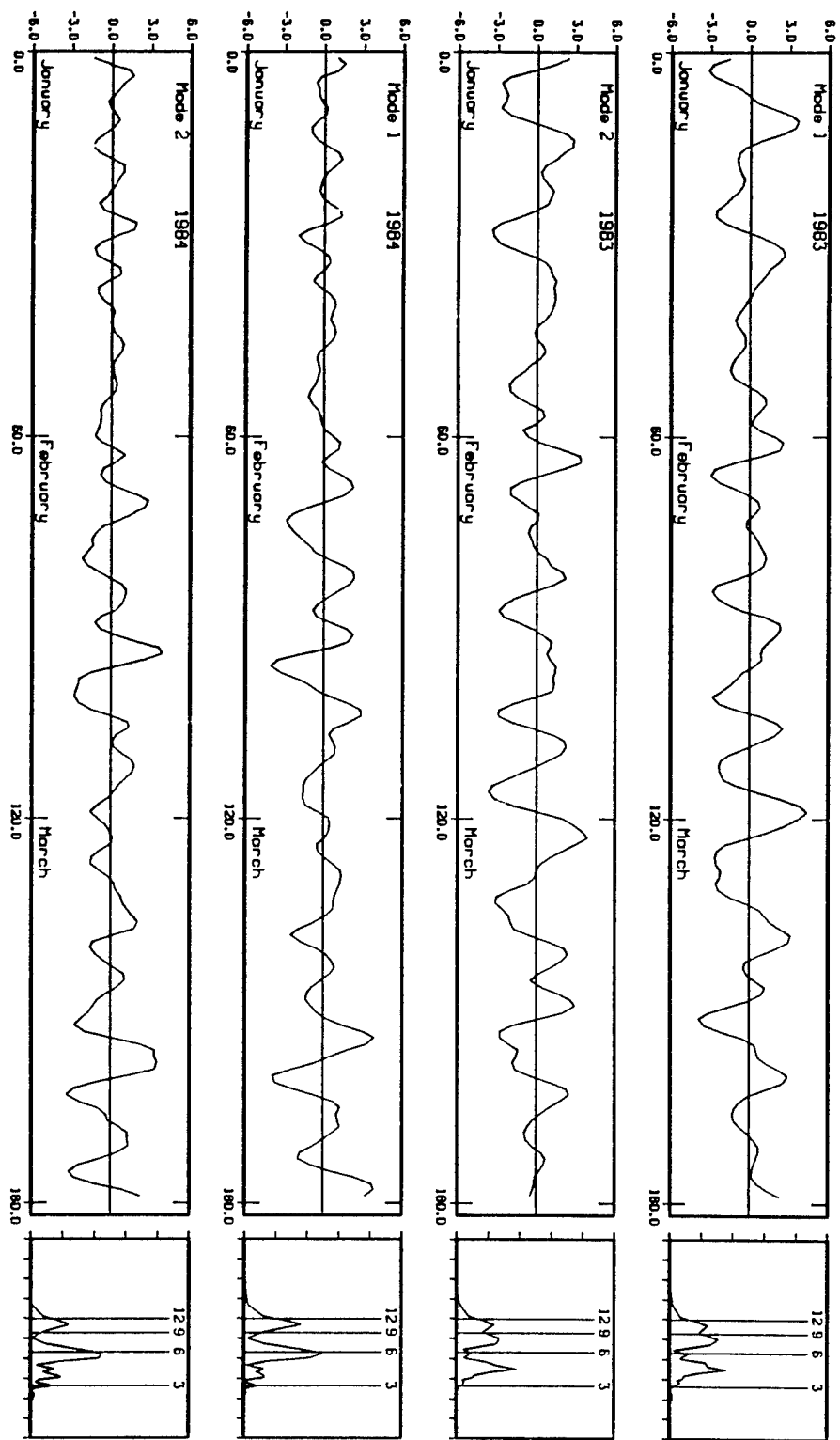


Figure 23. Same as Fig. 19 except for winters 1983 and 1984.

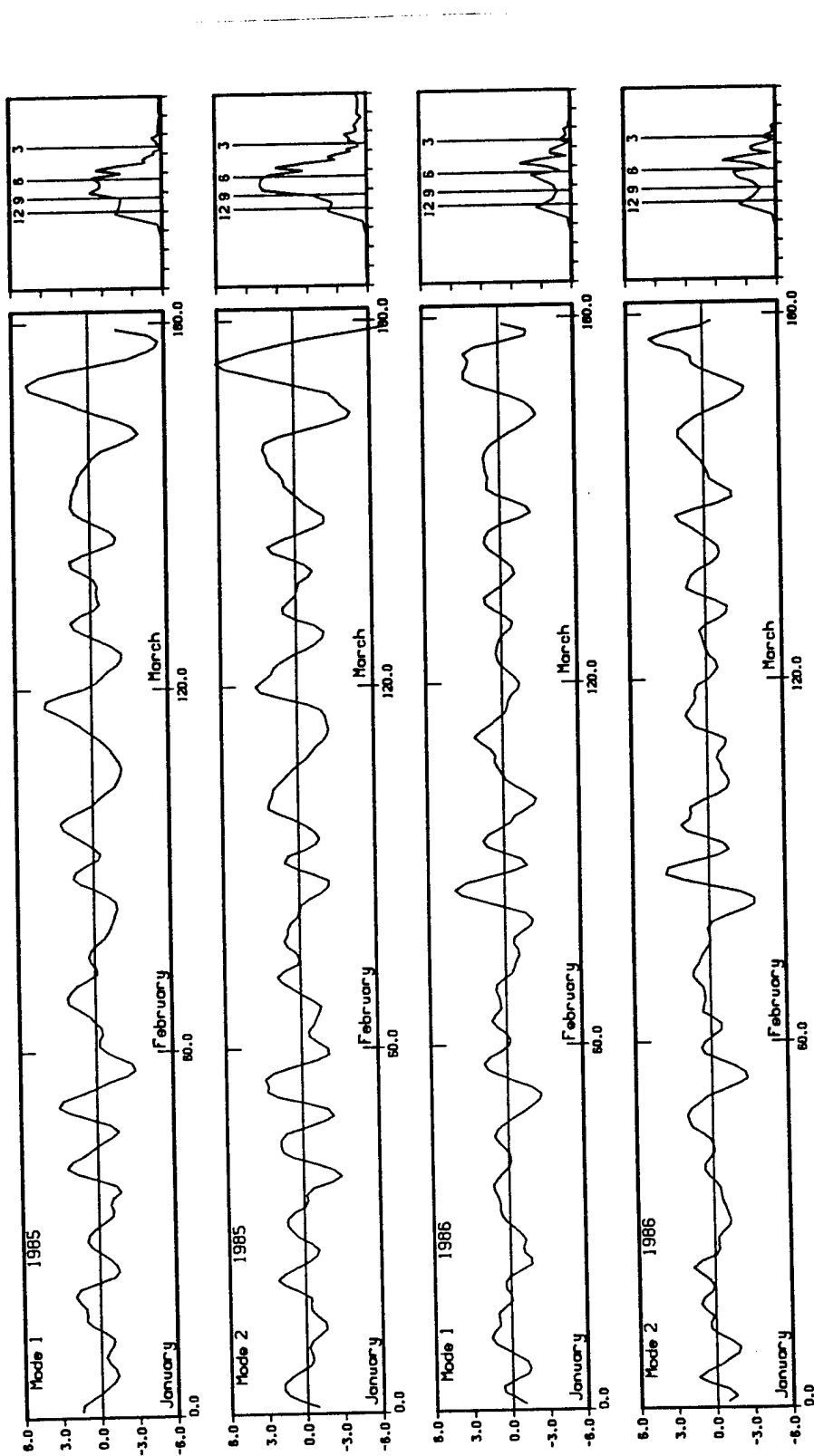


Figure 24. Same as Fig. 19 except for winters 1985 and 1986.

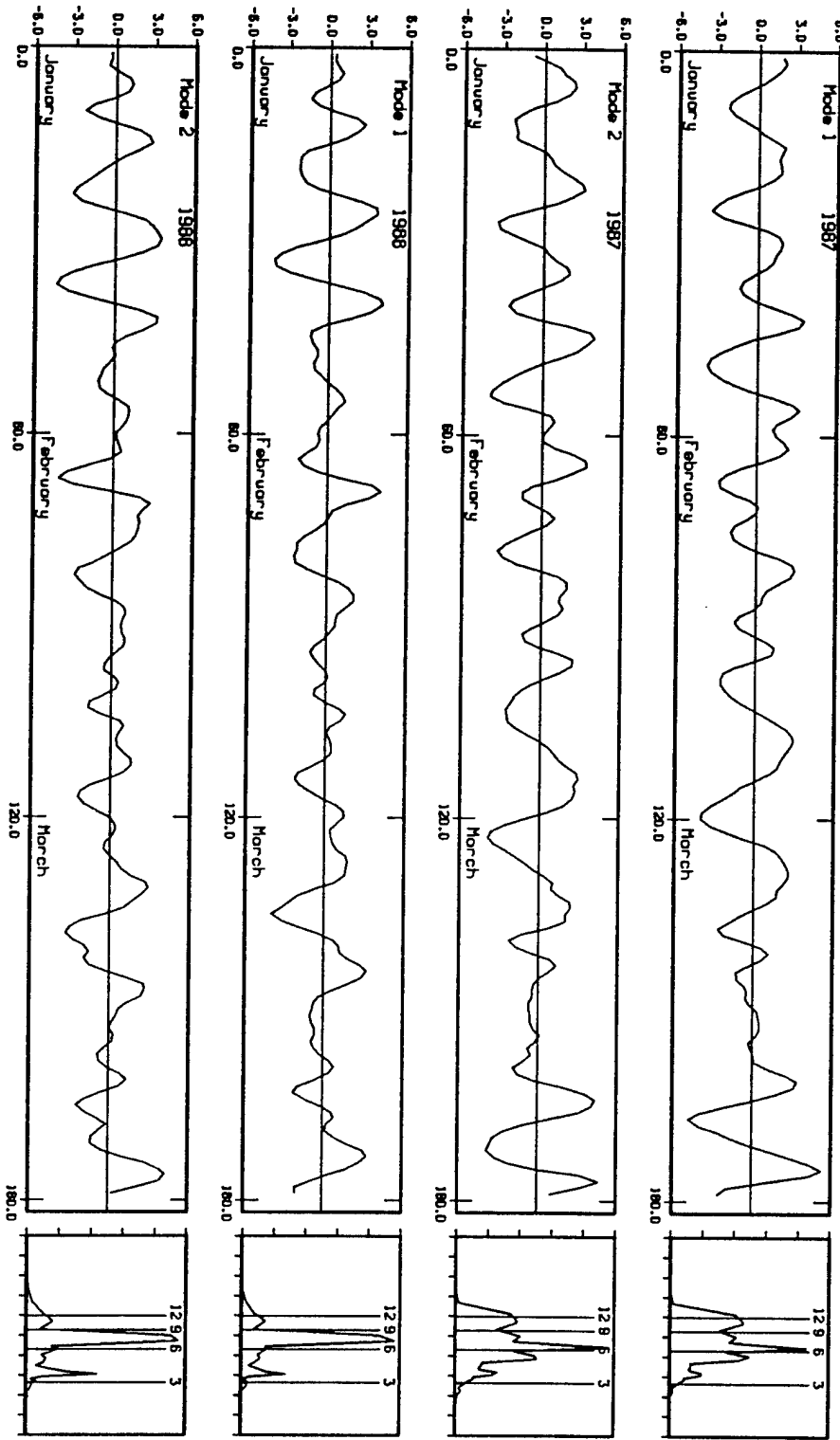


Figure 25. Same as Fig. 19 except for winters 1987 and 1988.

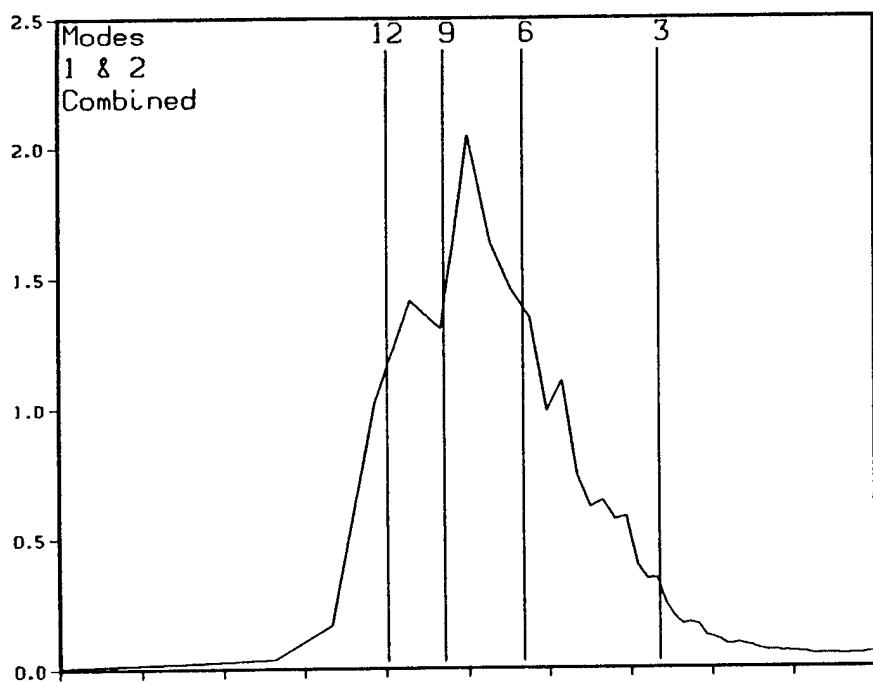


Figure 26. Average power spectrum for 14 winters, MCC modes 1 and 2 combined, East China Sea domain, with the 6, 9, and 12 day periods labeled.

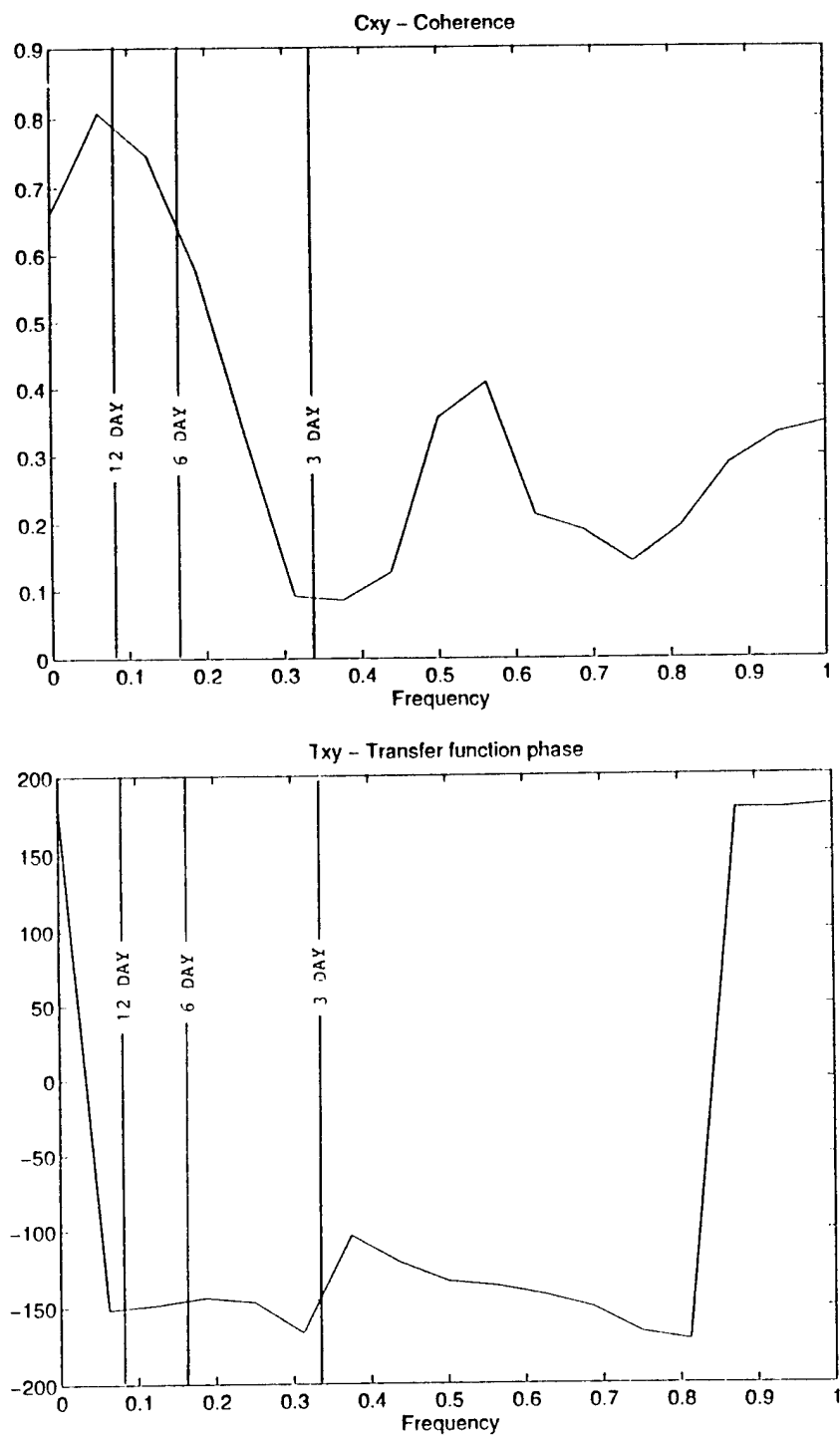


Figure 27. Coherence and transfer function phase plots for the amplitude coefficient time series of MCC mode 1, South China Sea domain, and MCC mode 1, East China Sea domain. 3, 6, and 12 day periods are labeled.

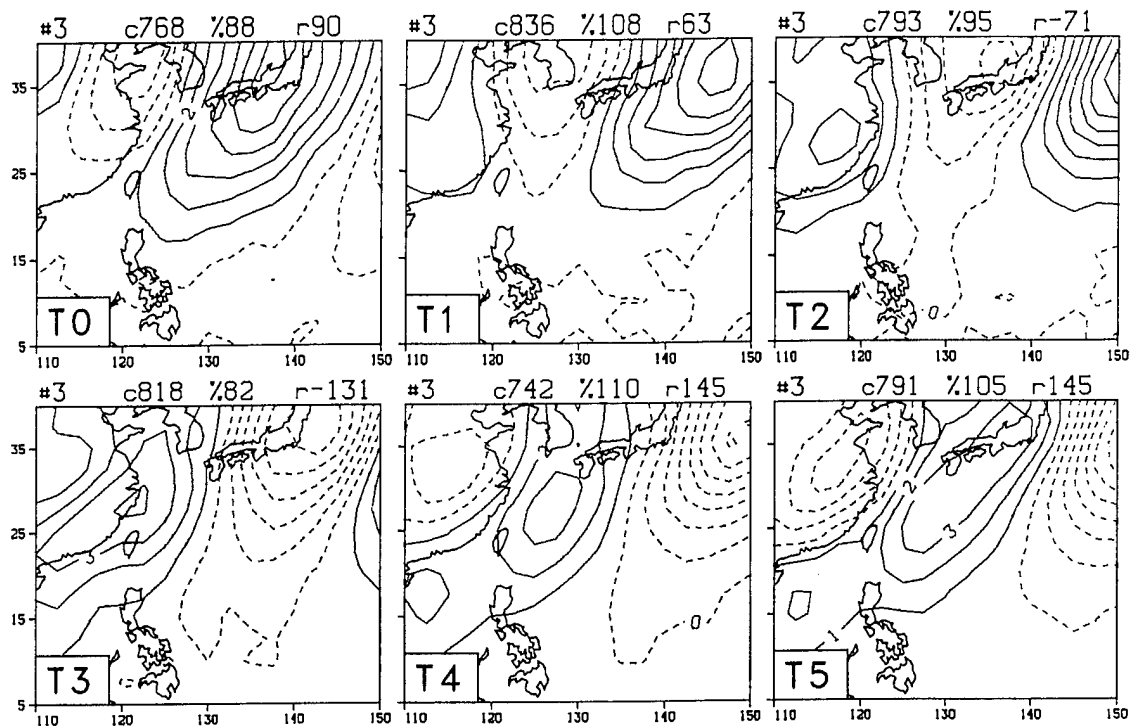


Figure 28. Weighting function for MCC mode 3, East China Sea domain, with the surface meridional wind (v) for 6 consecutive twelve-hourly frames from 00h (T0) to 60h (T5). Contour interval is 0.03 and dashed lines correspond to northerly winds when MCC mode 3 is positive. Data was passed through a 14-day high pass filter prior to analysis.

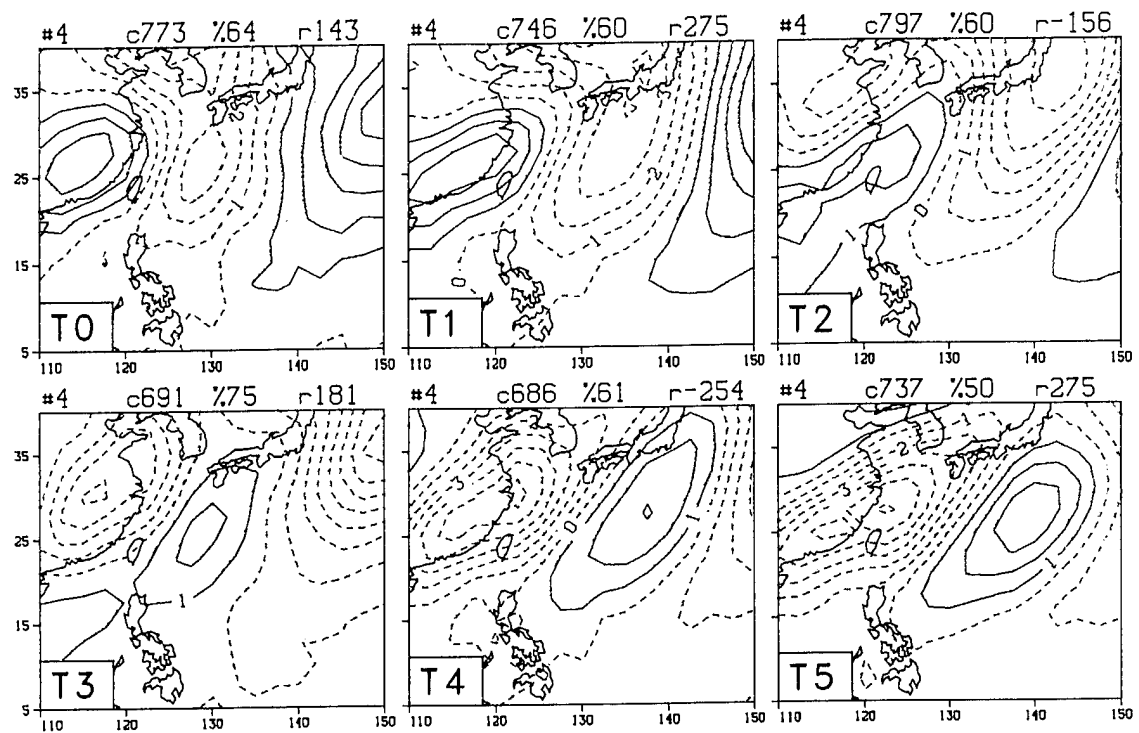


Figure 29. Same as Fig. 28 except for MCC mode 4.

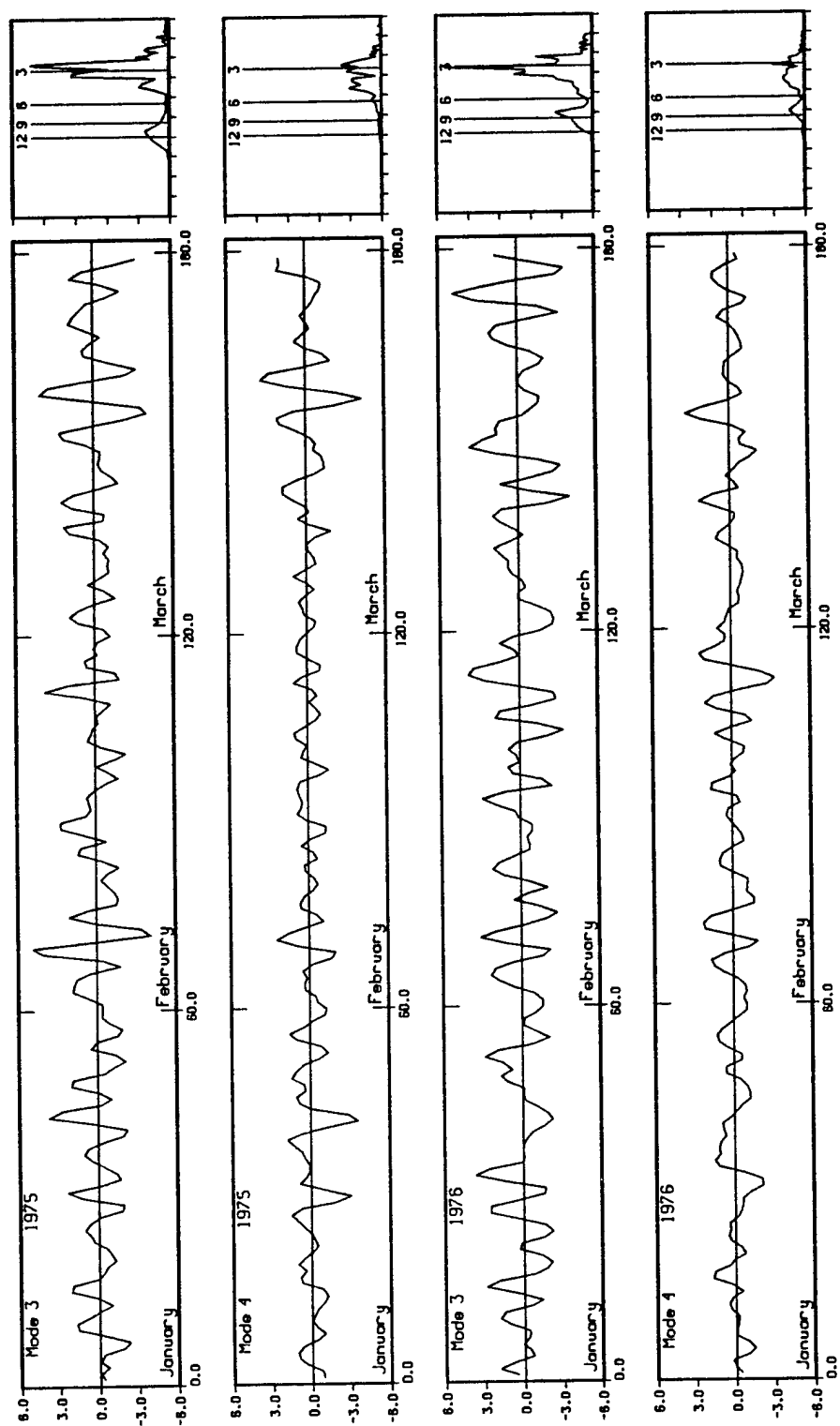


Figure 30. Time series of the time-integrated amplitude coefficients for MCC modes 3 and 4, East China Sea domain, for the winters 1975 and 1976. The power spectrum for each time series is shown at the right with the 3, 6, 9, and 12 day periods labeled.

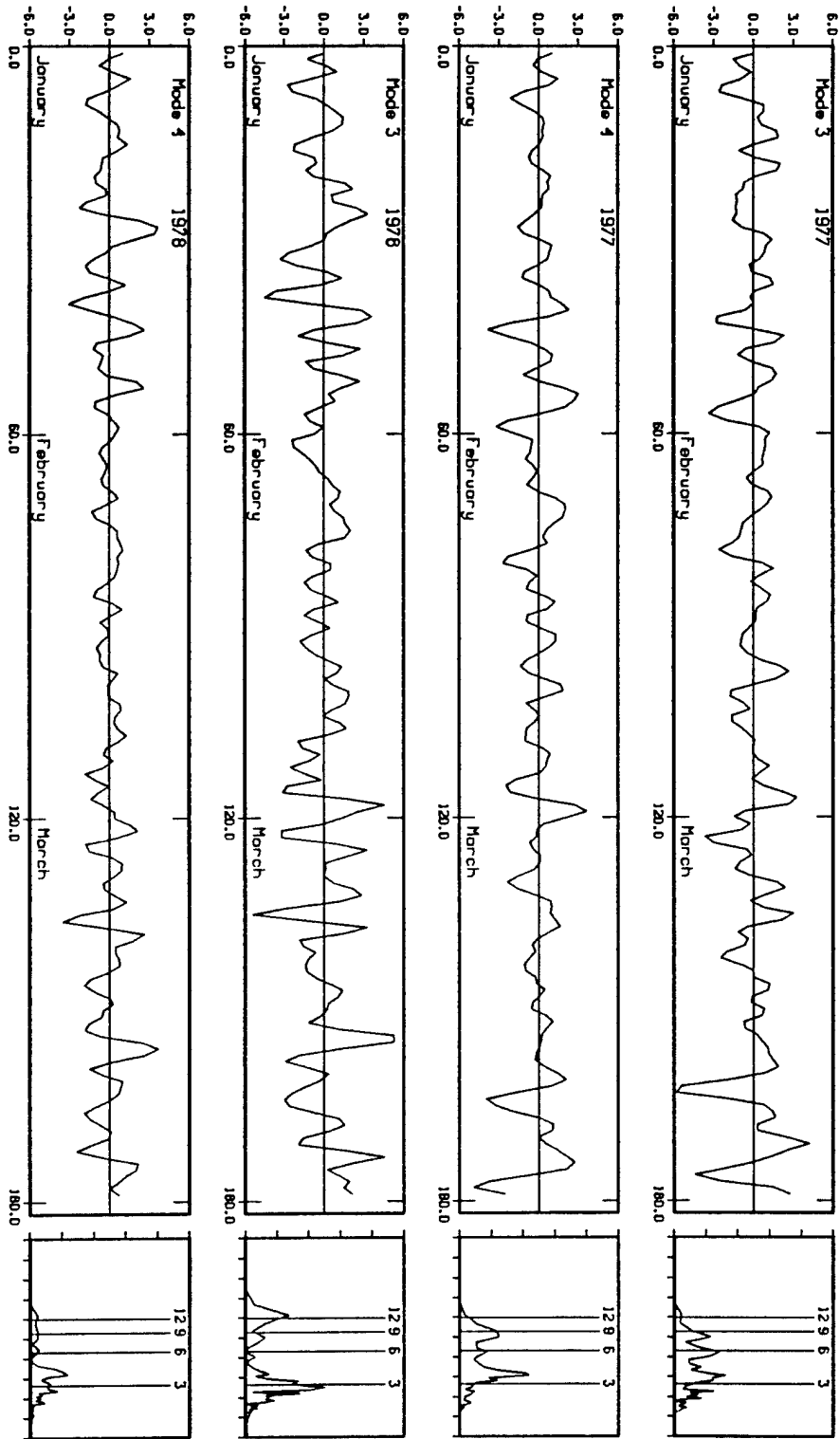


Figure 31. Same as Fig. 30 except for winters 1977 and 1978.

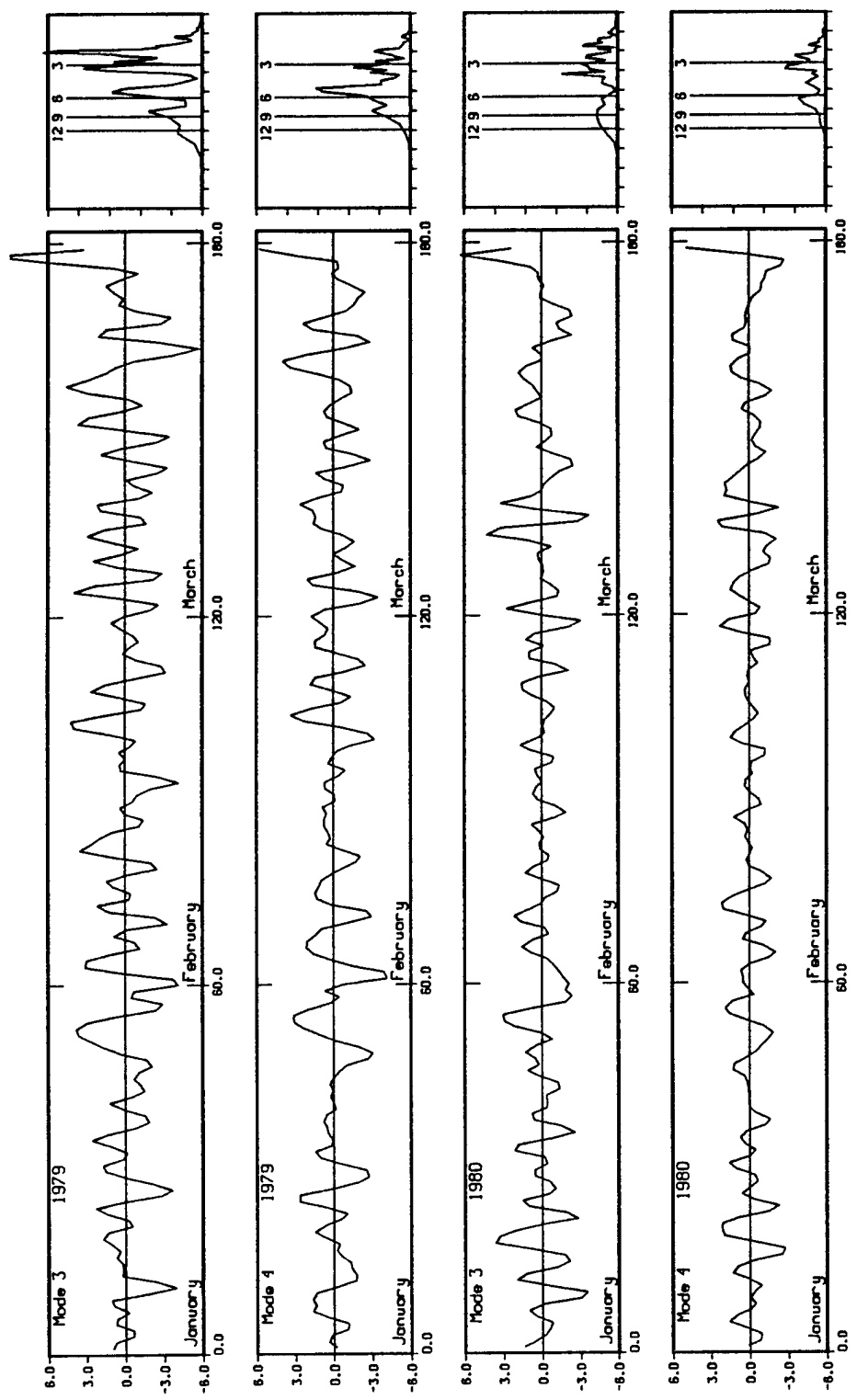


Figure 32. Same as Fig. 30 except for winters 1979 and 1980.

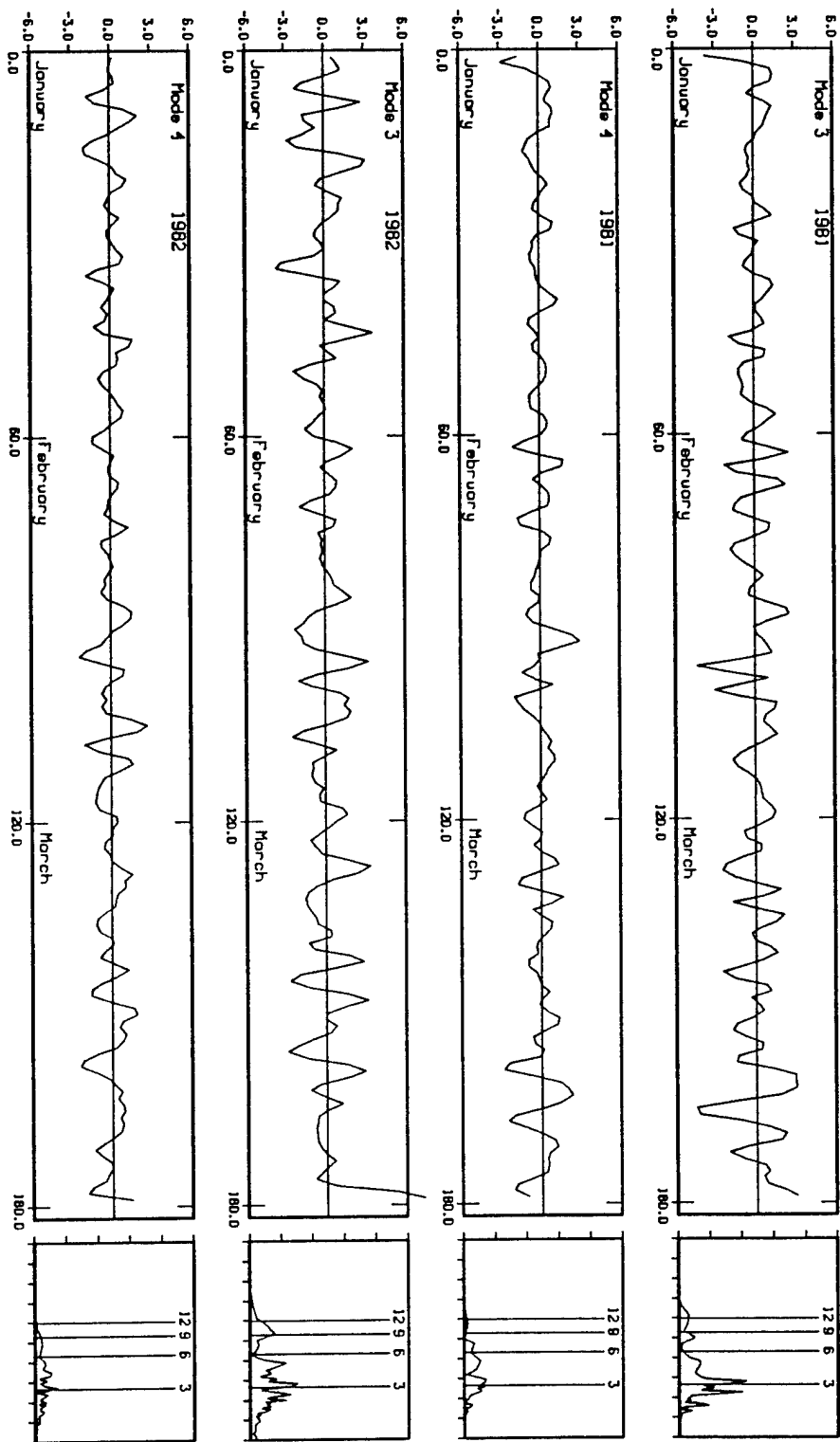


Figure 33. Same as Fig. 30 except for winters 1981 and 1982.

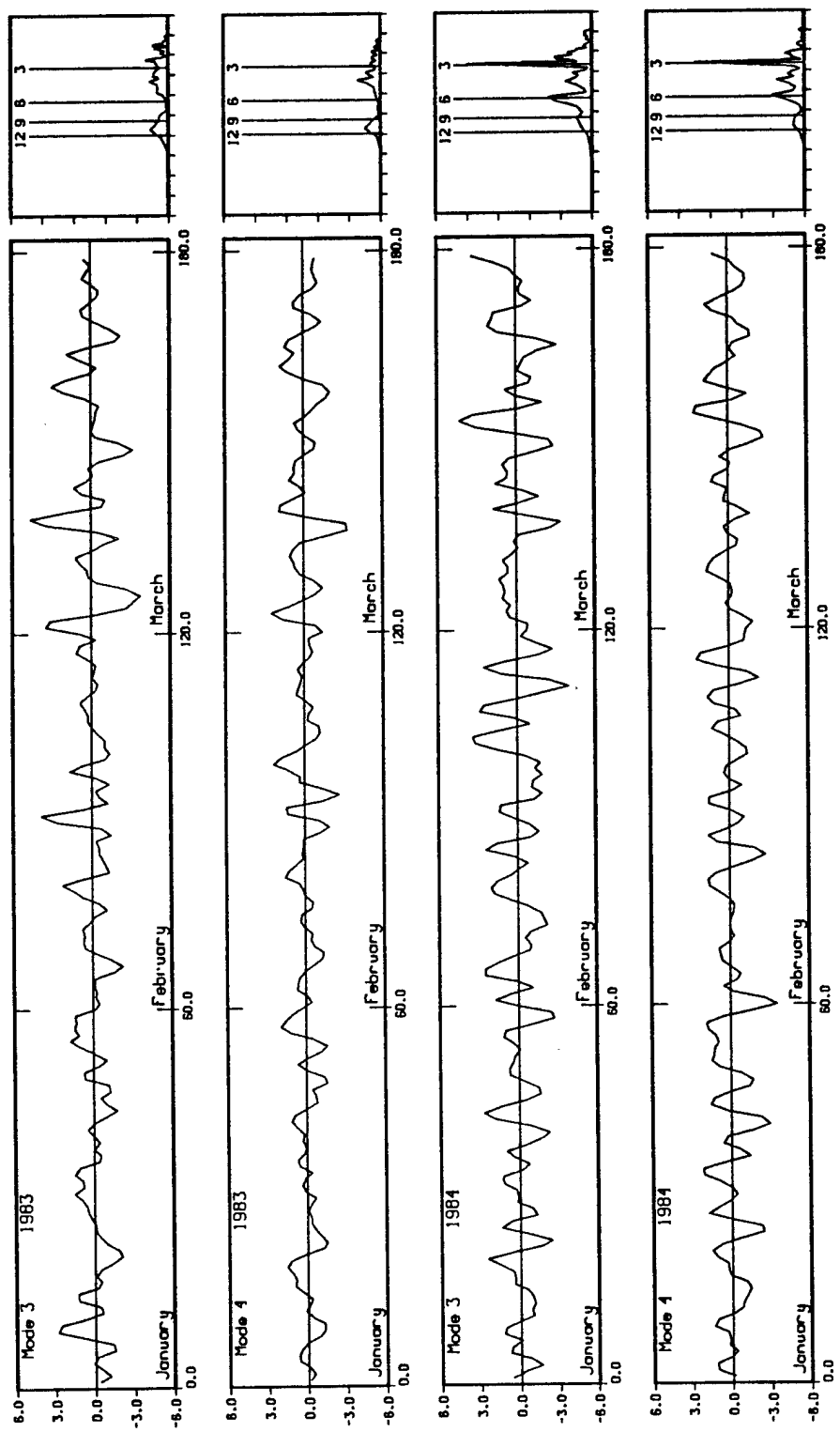


Figure 34. Same as Fig. 30 except for winters 1983 and 1984.

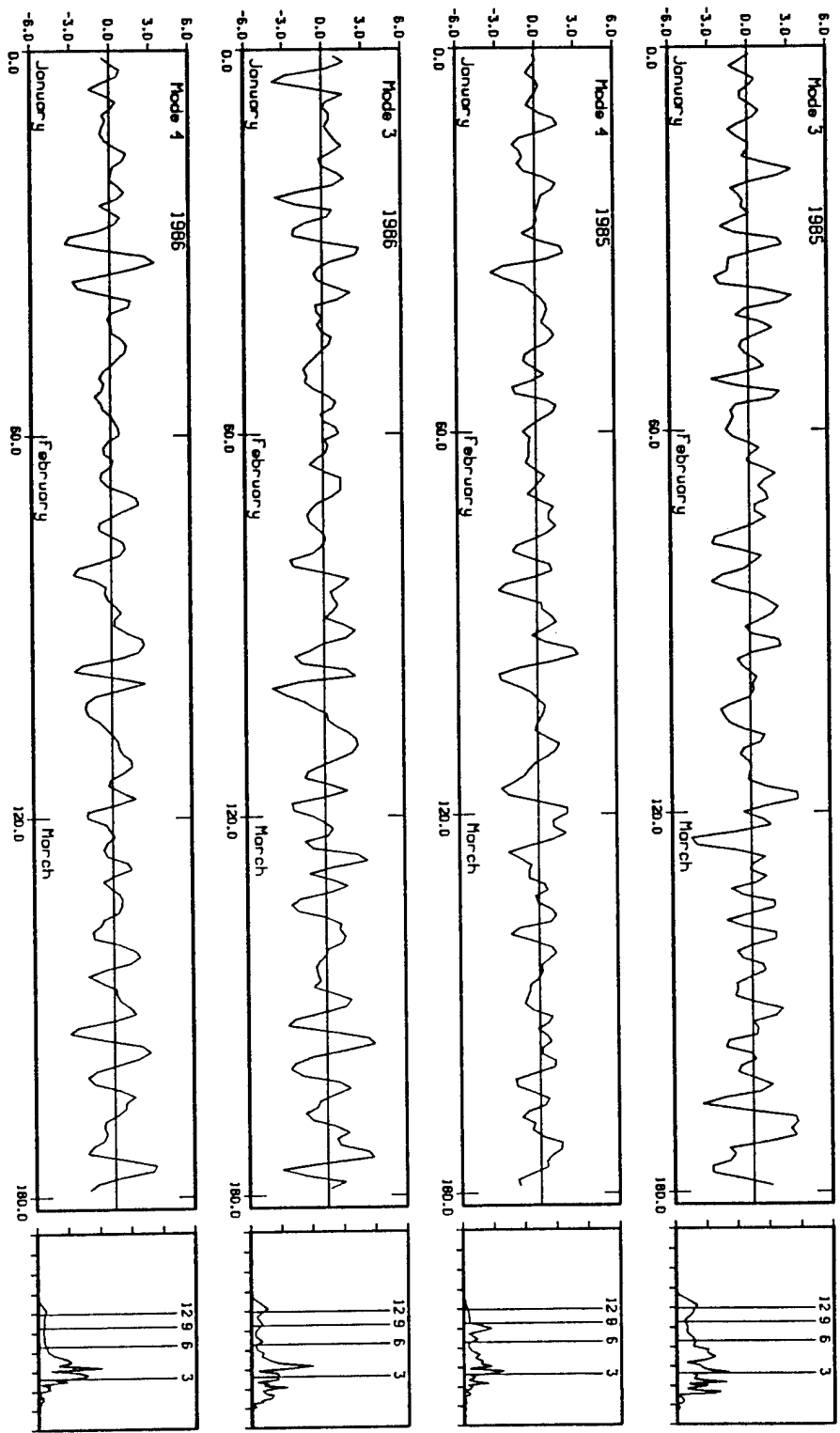


Figure 35. Same as Fig. 30 except for winters 1985 and 1986.

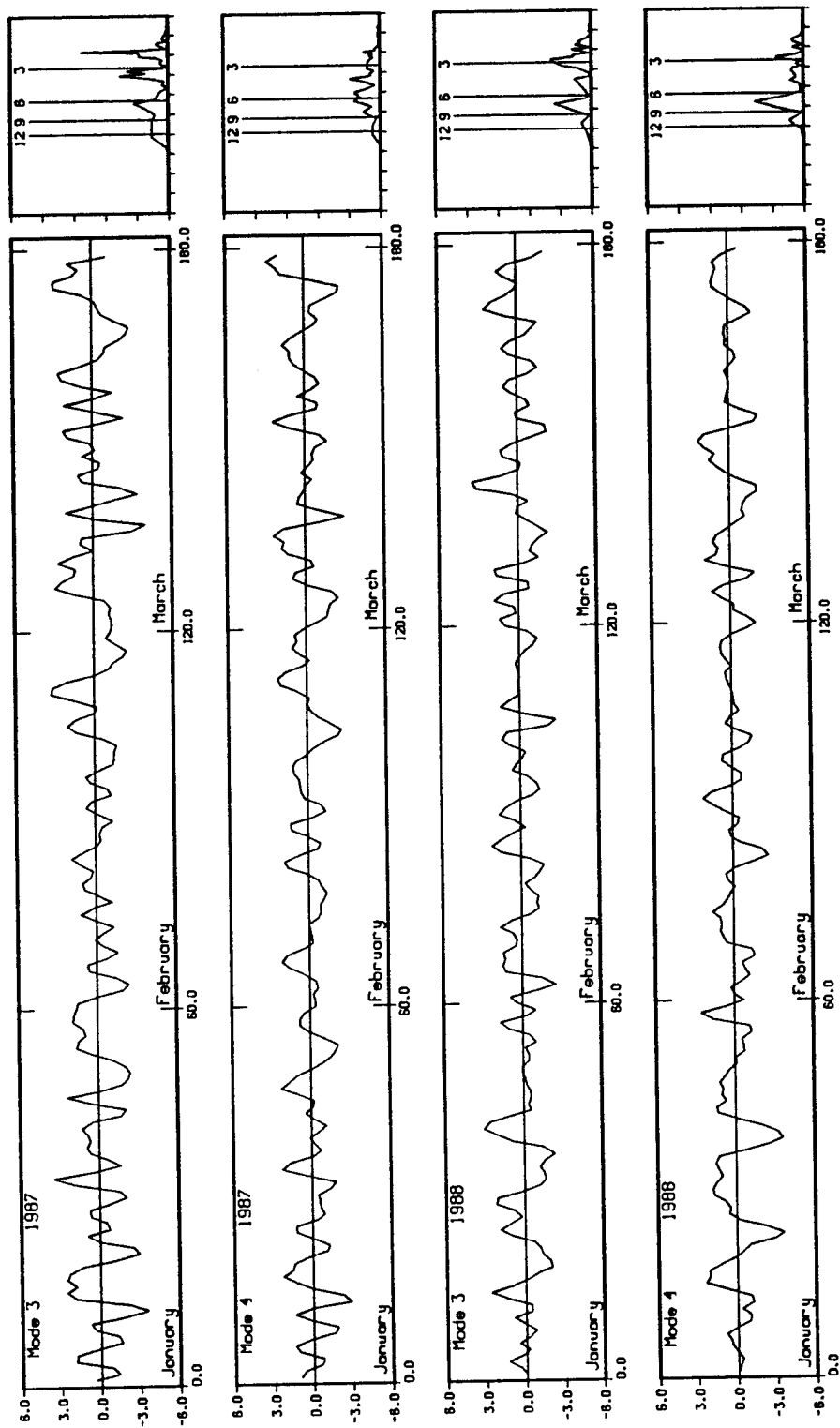


Figure 36. Same as Fig. 30 except for winters 1987 and 1988.

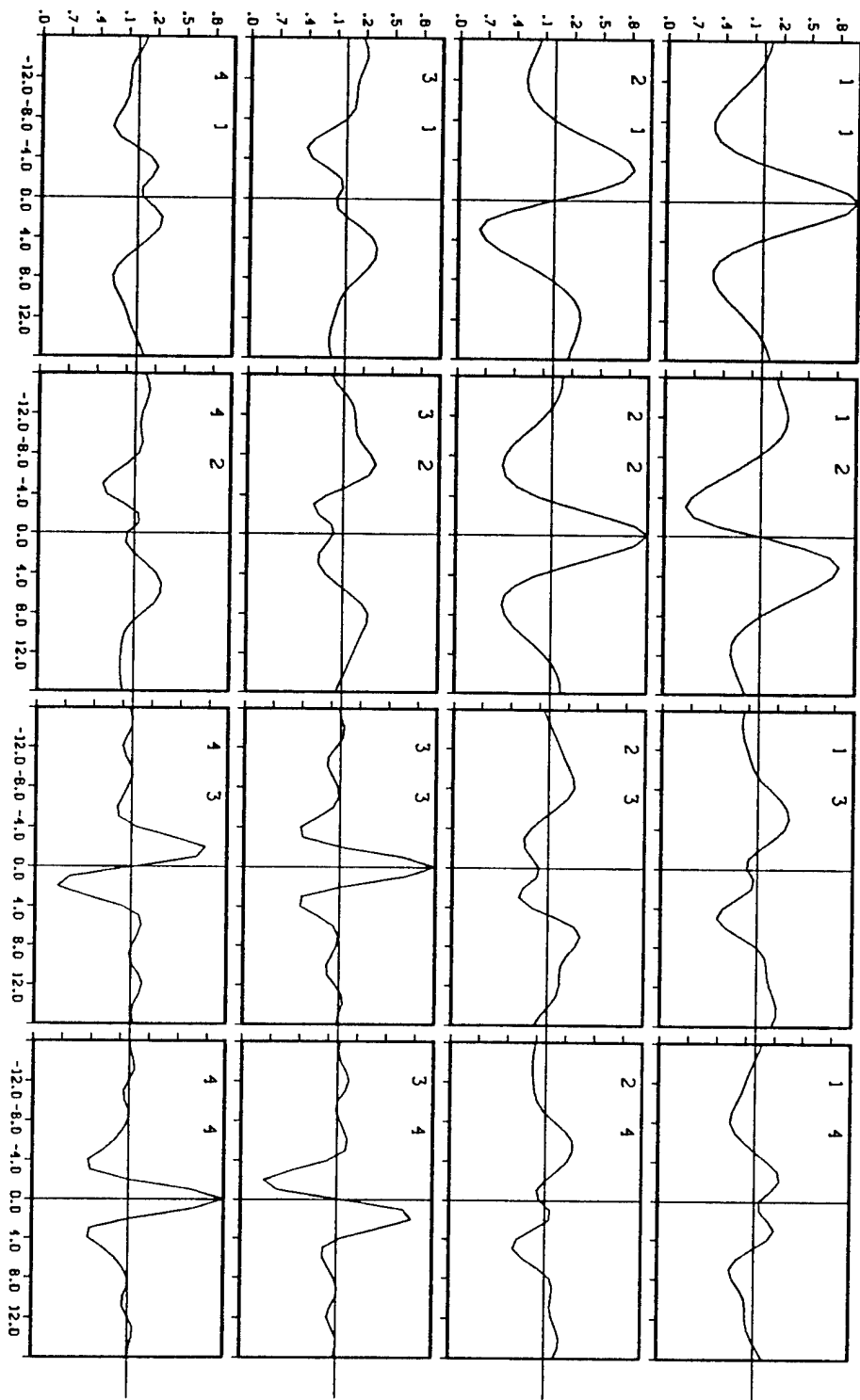


Figure 37. Lag correlation plots for MCC modes 1,2,3, and 4, East China Sea domain. The two modes correlated in each plot are labeled in the upper left corners. Each interval on the x-axis represents 2.0 days (4*12h).

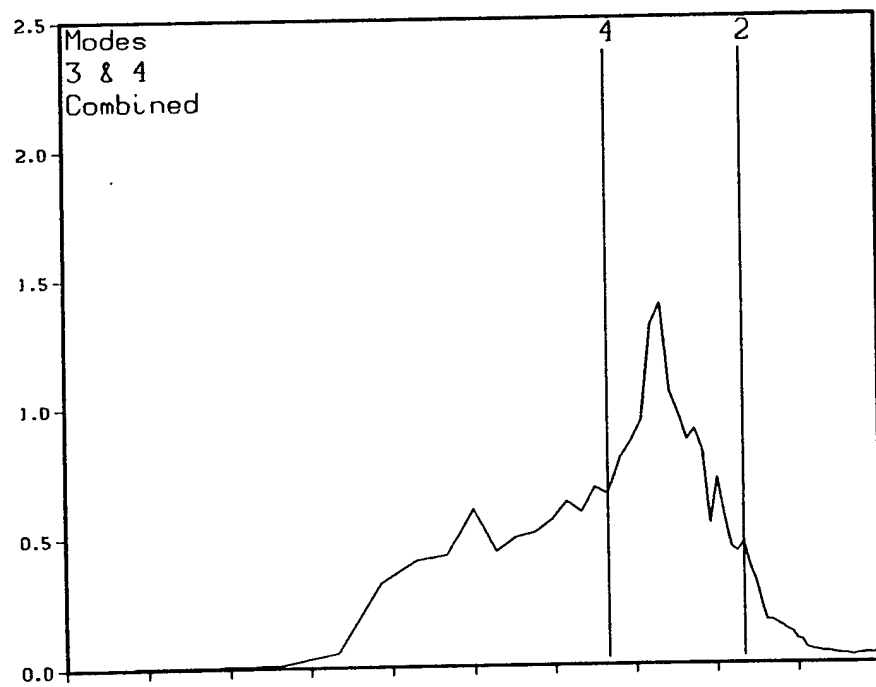


Figure 38. Average power spectrum for 14 winters, MCC modes 3 and 4 combined, East China Sea domain, with the 2 and 4 day periods labeled.

IV. STRUCTURE OF MOTIONS BASED ON CORRELATION AND COMPOSITE ANALYSES

A. SOUTH CHINA SEA MCC MODE 1

1. Single-point Correlation Analysis

The single-point correlation analysis plots of the surface meridional wind (v) with MCC mode 1, South China Sea domain, is given in Fig. 39. As expected, the surface v correlation patterns over the core domain look very similar to the MCC mode 1 weighting function. Recall that the MCC analysis was performed using surface v data. Over the 5 1/2 day period we again see a "surge cell" move southward into the South China Sea and dissipate by T7 followed by a similar cell of opposite sign. The tight gradient over the Indochina peninsula found in the weighting function patterns is also present here. The correlation pattern over the large domain contains large-scale anomalies with wavelengths on the order of 3000-4000 km that have northeast to southwest horizontal tilts and move from east to west with a period of about 8 days. As mentioned previously, these anomalies probably represent typical wintertime baroclinic waves. As further confirmation that MCC mode 1 for the South China Sea domain is essentially the same as MCC mode 1 for the East China Sea domain, surface v data is correlated with the latter and plotted in Fig. 40. Both plots contain the same basic features.

The single-point correlation analysis plots of the 700 hPa meridional wind with MCC mode 1, South China Sea domain, is given in Fig. 41. Here the correlation values are slightly smaller ranging from -0.3 to +0.3 compared to -0.4 to +0.5 for the surface case. At 700 hPa the core domain also shows a negative phase anomaly propagate southward into the South China Sea through T5 followed by a positive one through T11. Unlike the surface, however, the anomalies do not penetrate as far south to the equator. The primary feature in the large domain at 700 hPa is the 8-day, 3000-4000 km wave that propagates eastward from the Asian continent. The 200 hPa meridional wind correlation with MCC mode 1 also shows a longwave pattern with similar characteristics indicating that the phenomenon has large vertical extent (Fig. 42). In this case correlation values

range from -0.3 to +0.3 and there is no significant surge signal over the South China Sea.

2. Composite Analysis

a. Strong Cases

The 13 strongest cases of cold surge over the 14 year period from 1975-1988 were selected based on the highest peaks of the time-integrated amplitude coefficient time series for MCC mode 1 shown in the previous chapter (Figs. 8-14). Surface vector plots over the large domain based on composites of these 13 strong cases are given in Fig. 43. Each of the 6 frames is separated by 24 hours (vice 12 hours as in previous charts). The sequence shows a strengthening of northeasterly winds over the South China Sea from T0 to T8 and then a slight weakening at T10. The subtropical ridge pushes eastward from mainland China across the East China Sea at T0, breaks off as a closed anticyclone or "bubble high" by T2, and then continues its eastward propagation through T10. Notice that the strengthening of the northeasterly winds is mainly confined to the South China Sea region.

In order to see more of the detail hidden in this sequence of charts, the composites are calculated for 12 twelve-hourly frames with the background mean removed so that just cold surge anomalies are depicted (Fig. 44). The most prominent feature at T0 is the large cyclonic circulation anomaly centered over China producing strong southwesterly flow over the northern South China Sea and northwesterly flow over Indochina. A weak ridge sits just north of the cyclone near Mongolia. Weak anticyclonic anomalies are present over the Tibetan plateau and just east of Japan. Through T5 the large cyclonic anomaly over China becomes elongated into a trough and moves eastward over the western Pacific. Behind it, the weak Mongolian ridge anomaly strengthens and becomes a closed anticyclone. The weak Tibetan plateau cyclone loses its identity while the anticyclone east of Japan moves further eastward. The strong southwesterly flow anomaly over the South China Sea weakens considerably and is beginning to be replaced by northeasterlies descending from the north. During times T6 through T11 we observe almost exactly the opposite sequence of events. The anticyclone centered over central

China at T6 becomes elongated and moves eastward to just south of Japan by T11. It is replaced by a broad-based trough that moves in over China from the northwest. Northeasterly flow strengthens over the South China Sea through T8 and then weakens through T11. Although the magnitude is small, there may also be some evidence of cross-equatorial influence of the surge at times T10 and T11. As the surge weakens over the South China Sea, there is an increase in northeasterlies off the northwest coast of Australia.

The 700 hPa vector composite plots for the same 13 strong cases are shown in Fig. 45. Again the background mean has been removed to reveal detail in the anomalies. Over the South China Sea core region we again see southwesterly flow weaken and shift to northeasterly flow, however the transition occurs about 24 hours earlier and the overall magnitude is smaller than at the surface. In the 700 hPa large domain a large cyclonic circulation over China at T0 dissipates by T3 as a ridge moves in from the west and takes its place. The ridge becomes a weak semi-closed circulation at T5. Meanwhile, a large anticyclone centered over Japan moves eastward into the western Pacific and is replaced by a cyclonic circulation at T7. The cyclone follows the anticyclone out to sea through T11 ahead of another ridge that develops over the Yellow Sea. As seen at the surface, there again appears to be possible evidence of cross-equatorial surge influence during time T10 and T11 when northwesterly flow across the northwest coast of Australia increases in response to a developing cyclone over the Timor Sea.

The 200 hPa anomaly vector composite plots for the strong cases depict the expected longwave pattern propagation across the subtropical latitudes (Fig. 46). Over the core domain weak anomalous flow from the northeast begins about 48 hours earlier than at the surface and shifts to southwesterly flow at T7. One particularly interesting feature of this 200 hPa composite sequence are the circulations north of the Bay of Bengal. A weak anticyclone centered near Bangladesh at T1 strengthens through T4 and then becomes a ridge that drifts eastward across southern mainland China and then northeastward along the China coast to the East China Sea by T11. Meanwhile, over

Bangladesh, a cyclonic circulation is firmly established by T8 and remains relatively stationary while strengthening through T11.

Whether these circulations are a subtropical response to the cold surge or simply a reflection of the midlatitude triggering mechanisms is unknown and warrants further study. Chang and Lau (1982) studied 200 hPa winds of four winters and found a relationship between the acceleration of midlatitude jet streaks and the cold surge, but did not observe these circulations. The reason for this is that the circulations are not detectable when masked by the mean flow. Fig. 47 shows the same 200 hPa composites with the mean flow included. Here the time difference between each frame is 24 hours. Propagation of jet streaks across the midlatitudes is clearly shown, but there is no evidence of the circulations. There is also no cold surge signal detectable over the South China Sea as was the case with the anomaly plots.

b. Medium Cases

In order to determine whether the features of the cold surge described in the previous section are common not only to a few strong events over a 14 year period, but also to cold surges in general, the time-integrated amplitude coefficient time series for MCC mode 1 was again used as a basis to select 54 "medium-strength" cases over the same period. Vector anomaly composite plots were again produced for the surface, 700 hPa, and 200 hPa levels (Figs. 48, 49, 50, respectively). Most of the characteristics of the surge found in the strong cases are also present in the medium cases with a few subtle differences. At the surface the magnitude of the northeast and southwest wind anomalies over the South China Sea are slightly smaller in the medium case composites. Also, possible cross-equatorial surge influence is manifested differently with the medium cases. If we focus on an area just north of 20°S between 100°E and 110°E, we notice slight southerly flow from T0 through T5 transition to northerly flow through T11. Although the magnitude of these anomalies is small, the manner and period of change exactly match those of the cold surge.

At 700 hPa the patterns for the medium cases are essentially the same as

those for the strong cases. Again, the difference between the two is magnitude, with the strong case anomalies being slightly larger. Also, the northeast and southwest anomalies over the South China Sea do not reach quite as far south in the medium cases, so cross-equatorial influence does not appear to occur.

At 200 hPa the differences between the strong and medium cases are again subtle. Although the anomalies in the medium cases are smaller in magnitude, they still show the same midlatitude longwave propagation pattern. The anomalous circulations centered over Bangladesh found in the strong cases are also present here.

c. Divergence

As mentioned in the introduction, cold surge events may have a significant impact on tropical convection. To investigate this, 200 hPa divergence fields were calculated over the large domain using the u and v anomaly fields. The following calculation was performed at each grid point:

$$D(i, j) = \frac{u(i+1, j) - u(i-1, j)}{\Delta x} + \frac{v(i, j+1) - v(i, j-1)}{\Delta y}$$

The resulting divergence fields were then spatially averaged and composited based on the time-integrated amplitude coefficient time series for MCC mode 1 exactly as before.

The composite sequence based on the 13 strongest cases is given in Fig. 51. The sequence shows three noticeable features. The first is in the area defined by 0° to 20°S and 70°E to 90°E. This region contains a convergence anomaly from T0 to T5 that is strongest at T2. At T6 a positive divergence anomaly becomes established and persists through T10. The second notable feature is found in the vicinity of Borneo. Weak 200 hPa convergence over Borneo between T0 and T7 gives way to strong divergence through T9. The divergence center is particularly strong at T9. In both areas the increases in 200 hPa divergence is evident in the second half of the sequence. This coincides with the time of maximum northeast surge anomaly over the South China Sea described in the

previous section and is consistent with the findings of Lau and Chang (1987). The difference in Lau and Chang's study is that they used velocity potential fields which smooth out any synoptic scale divergence. Our results show anomalies with a much smaller zonal scale. The third interesting feature is a positive divergence anomaly positioned along the equator near 150°E at time T0. This positive anomaly persists through the entire 12 frame sequence and slowly moves eastward to near 175°E by T11. This feature might be associated with an equatorial Kelvin wave.

A composite sequence of 200 hPa divergence fields based on the 54 medium-strength cold surge cases was also produced (Fig. 52). The most striking difference between this and the strong cases sequence is the lack of significant magnitude anomalies. In fact, the maximum values shown are probably well within the range of error inherent in kinematic divergence calculations. We might conclude then that the medium-strength cold surge does not produce enough of an impact on 200 hPa divergence to be detectable in the data.

B. EAST CHINA SEA MCC MODE 3

1. Single-point Correlation Analysis

The single-point correlation analysis plots of the surface meridional wind (v) with MCC mode 3, East China Sea domain, is given in Fig. 53. Again, as expected, the surface v correlation patterns look very similar to the MCC mode 3 weighting function. Correlation values range from -0.4 to +0.4. Over the 2 1/2 day sequence, elongated anomalies that tilt from northeast to southwest with wavelengths on the order of 1500 to 2000 km move generally eastward with periods of about 3 days. The anomalies appear to develop over the Asian continent and then move out into the East China Sea before tracking more northeasterly to the north-central western Pacific.

The single-point correlation analysis plots of the 700 hPa meridional wind with MCC mode 3 is given in Fig. 54. Again correlation values range from -0.4 to +0.4. The pattern here looks exactly as the surface case except the anomalies are more round and

do not extend as far southward. The 200 hPa meridional wind correlation with MCC mode 3 also shows the same characteristic anomalies, but here the centers are displaced to the north along 40°N (Fig. 55). Correlation values at 200 hPa also range from -0.4 to +0.4.

2. Composite Analysis

The time-integrated amplitude coefficient time series for MCC mode 3 over 14 winters from 1975 to 1988 (Figs. 30-36) was used as a basis to select cases for composite analysis. 27 cases were selected and composited to yield 6 twelve-hourly surface anomaly vector plots shown in Fig. 56. The sequence is characterized by a trough at T0 centered over the Sea of Japan that propagates eastward over the central western Pacific by T5. Behind it, a ridge anomaly located along the China coast at T0 becomes a closed anticyclone near Korea at T2 and moves almost due east to near 150°E by T5. One particularly interesting feature in this sequence is the reversal of wind anomalies over the South China Sea region from northerlies between T0 and T2 to southerlies from T3 through T5. This indicates that there is also some effect, albeit small, over the South China Sea area associated with smaller, shorter time scale events in the midlatitudes. This implies that the strong cold surge over the South China Sea may be expected when MCC modes 1 and 3 are in phase, and weak surges may be expected if they are out of phase.

The 700 hPa anomaly vector composite plots for the same 27 cases are shown in Fig. 57. The same features seen in the surface plots are also present here except they are displaced slightly to the west indicating they have a backward tilt with height, which is characteristic of baroclinic systems. There is no apparent signal over the South China Sea region at 700 hPa.

At 200 hPa, the anomalies again have the same spatial and temporal scale as the lower levels with a small displacement to the west (Fig. 58). The reversal in wind anomalies over the South China Sea region seen in the surface plots is also present here. Note that southwest anomalies at T0 appear to be a weak southwestern extension of the midlatitude jet streak centered over Japan. As the jet streak moves east of Japan through

T2, the magnitude of the anomalies decreases to near zero. This phenomenon is also evident in the 200 hPa MCC mode 1 composite sequences for both the strong and medium-strength cases although it is not as obvious.

The fact that these shorter wavelength, shorter time scale anomalies are present at 700 hPa and 200 hPa and have westward vertical tilt indicates they are baroclinic with large vertical extent. Recall that the intermediate-scale cyclones observed by Nitta and Yamamoto (1973) discussed in Chapter I, were of the same horizontal spatial and temporal scales as these here, but are described as being shallow with no significant development above about 850 hPa. It is possible that the shorter scale disturbances represented here begin as weak shallow depressions over the east Asian continent and then gain upper level support as they move out over the ocean. This scenario is consistent with the findings of Saito (1977) mentioned earlier.

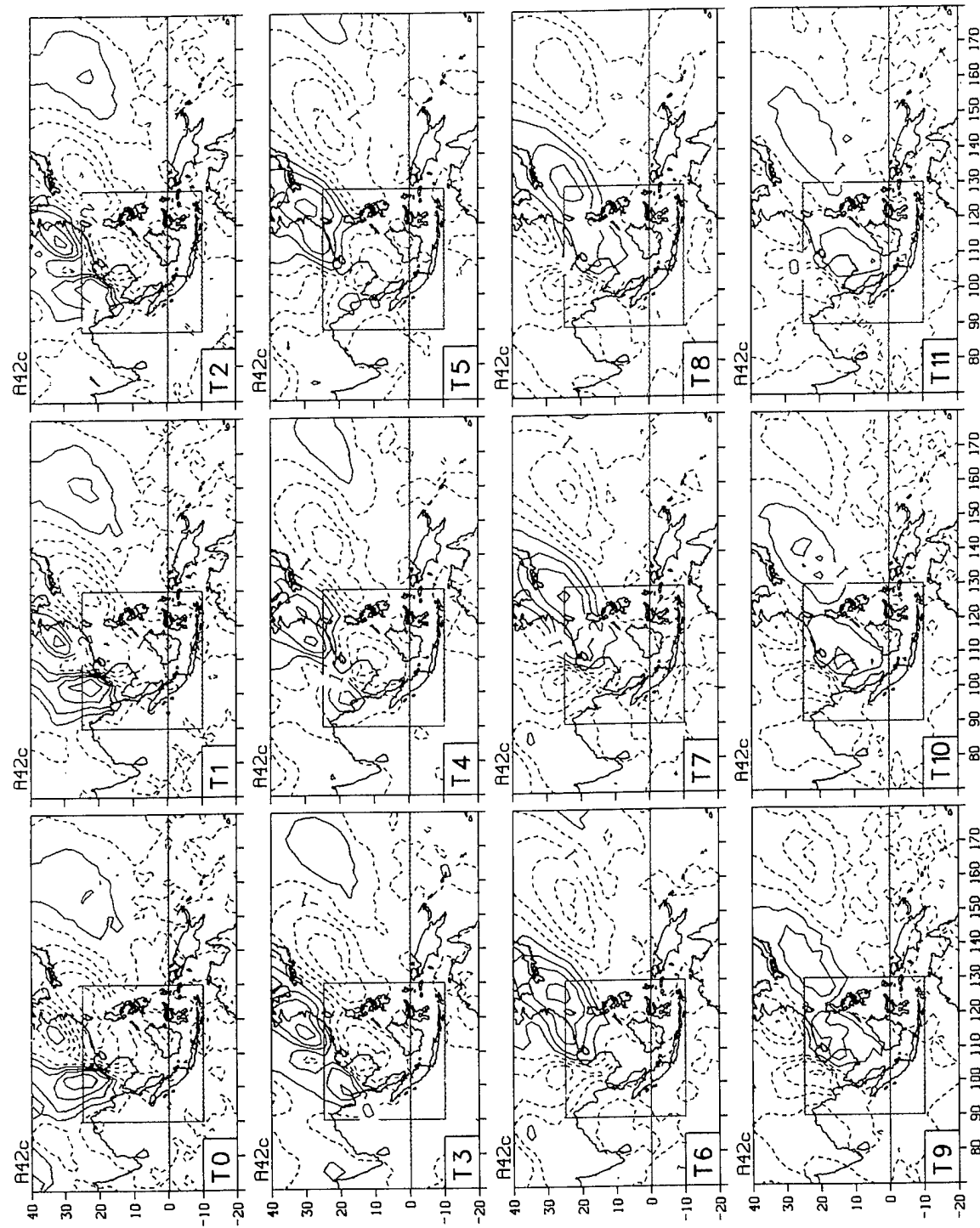


Figure 39. Single-point correlation patterns of surface v with MCC mode 1, South China Sea domain, at 12 consecutive 12-hourly time lags. Contour interval is 0.1 and negative values are dashed.

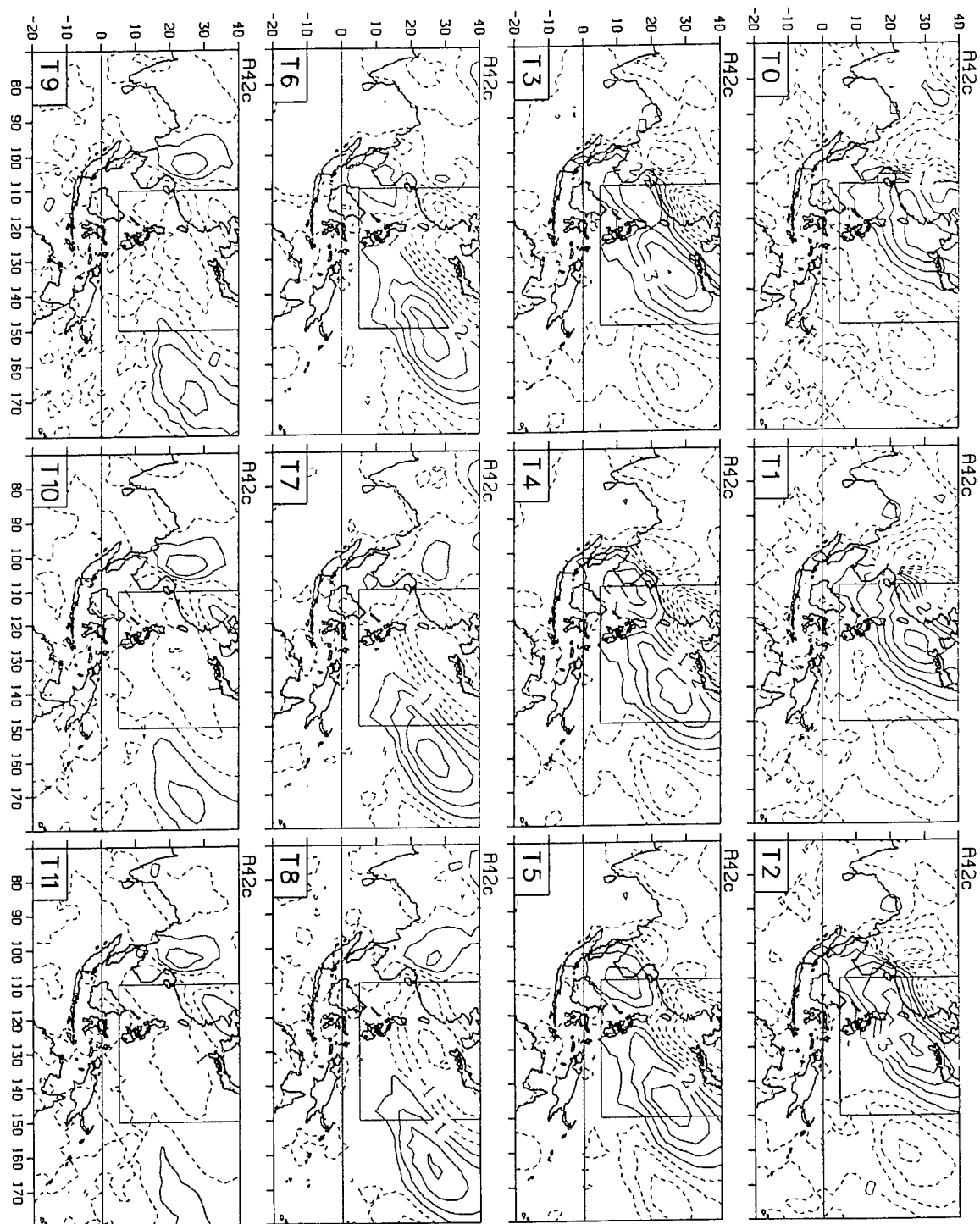


Figure 40. Same as Fig. 39 except for MCC mode 1, East China Sea domain.

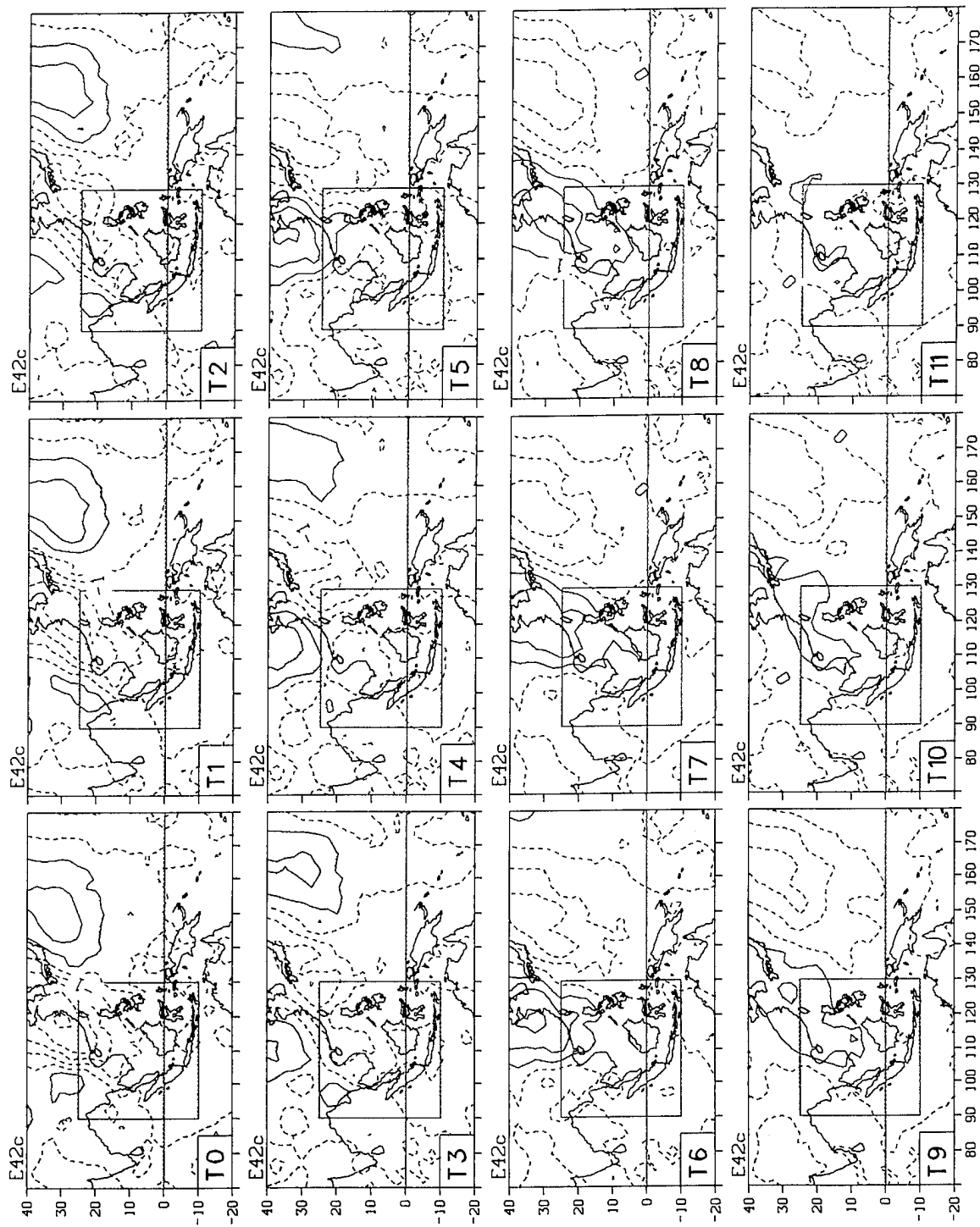


Figure 41. Same as Fig. 39 except for 700 hPa v .

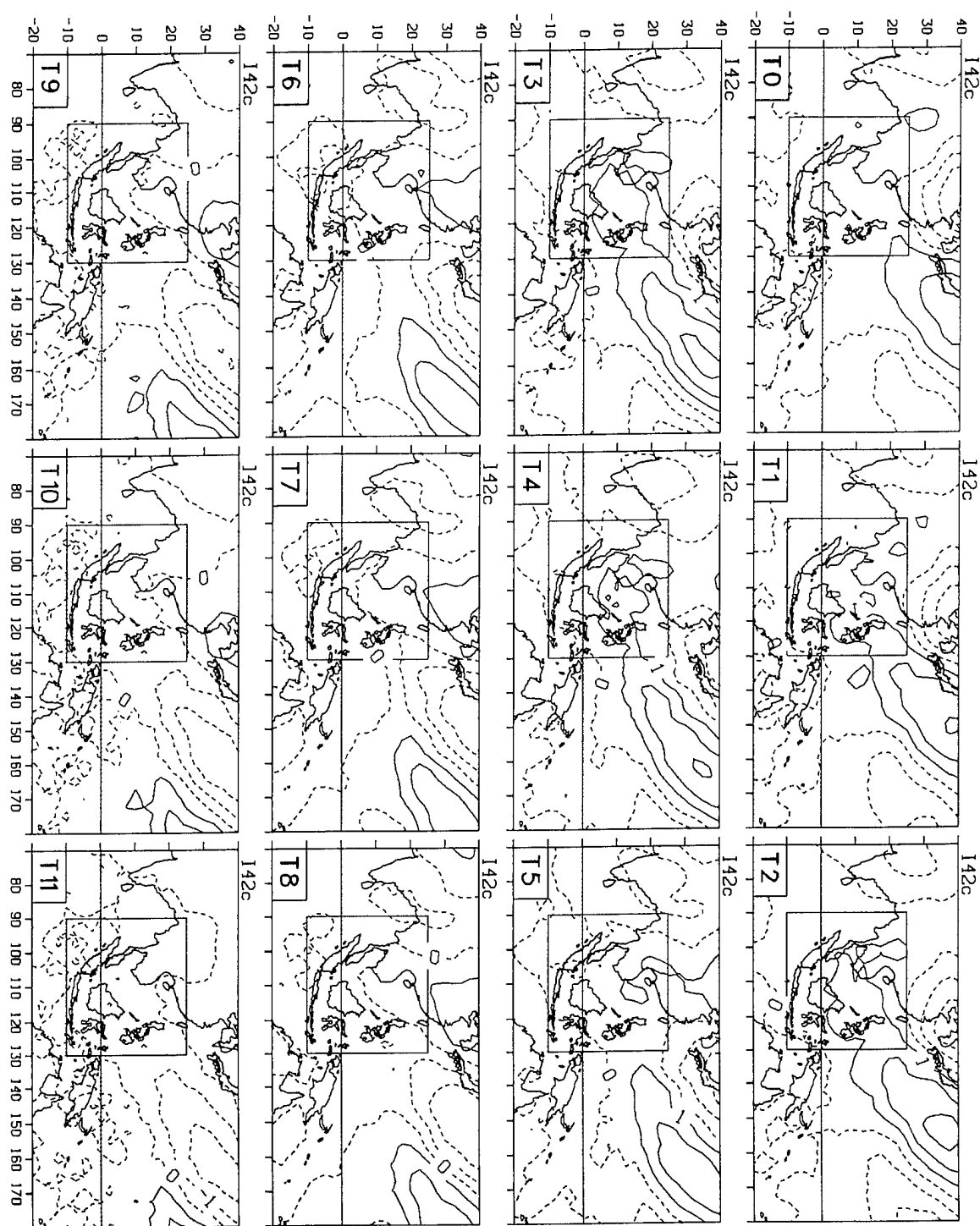


Figure 42. Same as Fig. 39 except for 200 hPa v .

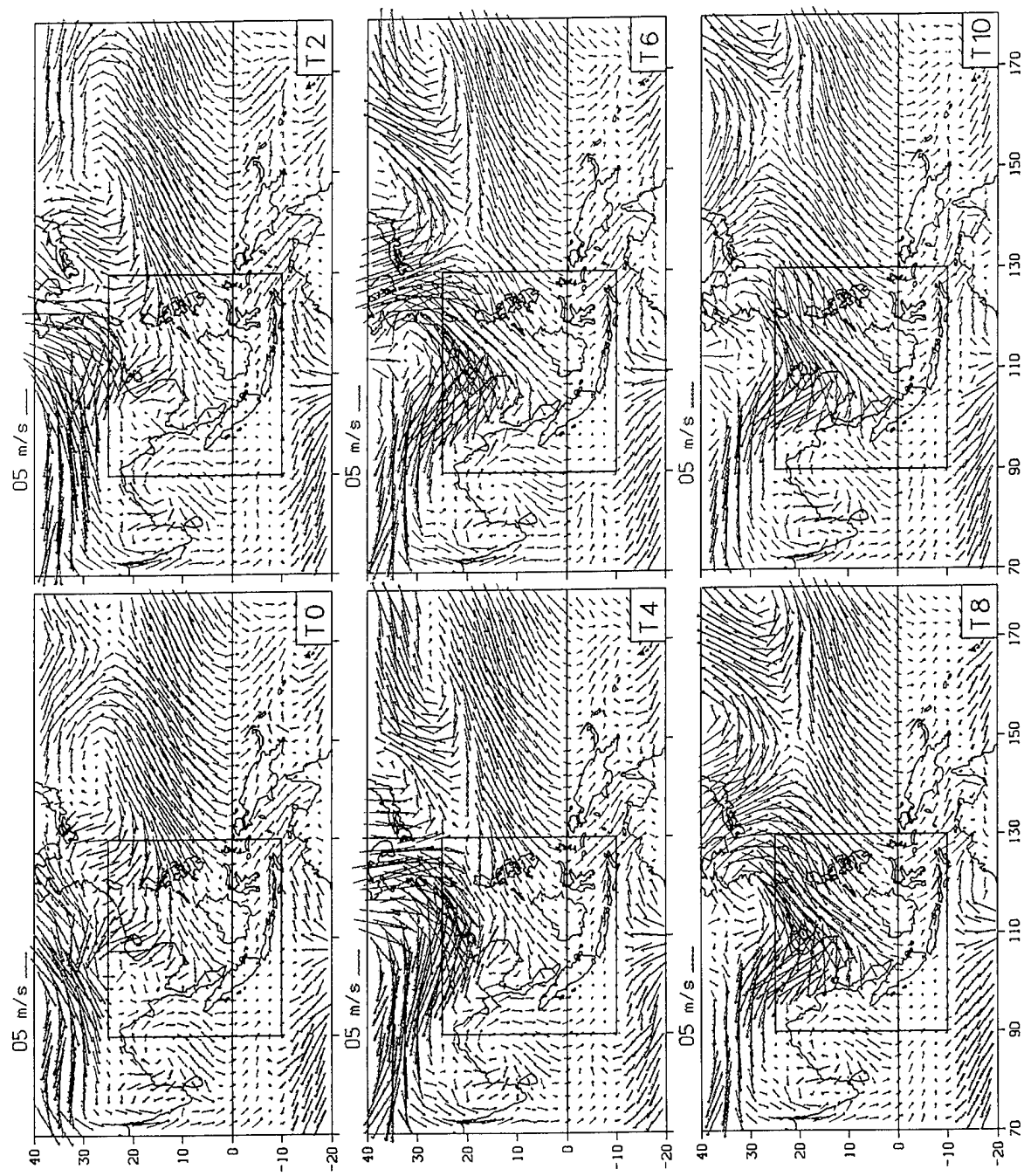


Figure 43. Surface wind vector plots based on composites of the 13 strongest cold surge cases at 6 consecutive 24-hourly time lags with the background mean included. Vector scale is shown at the top of each frame.

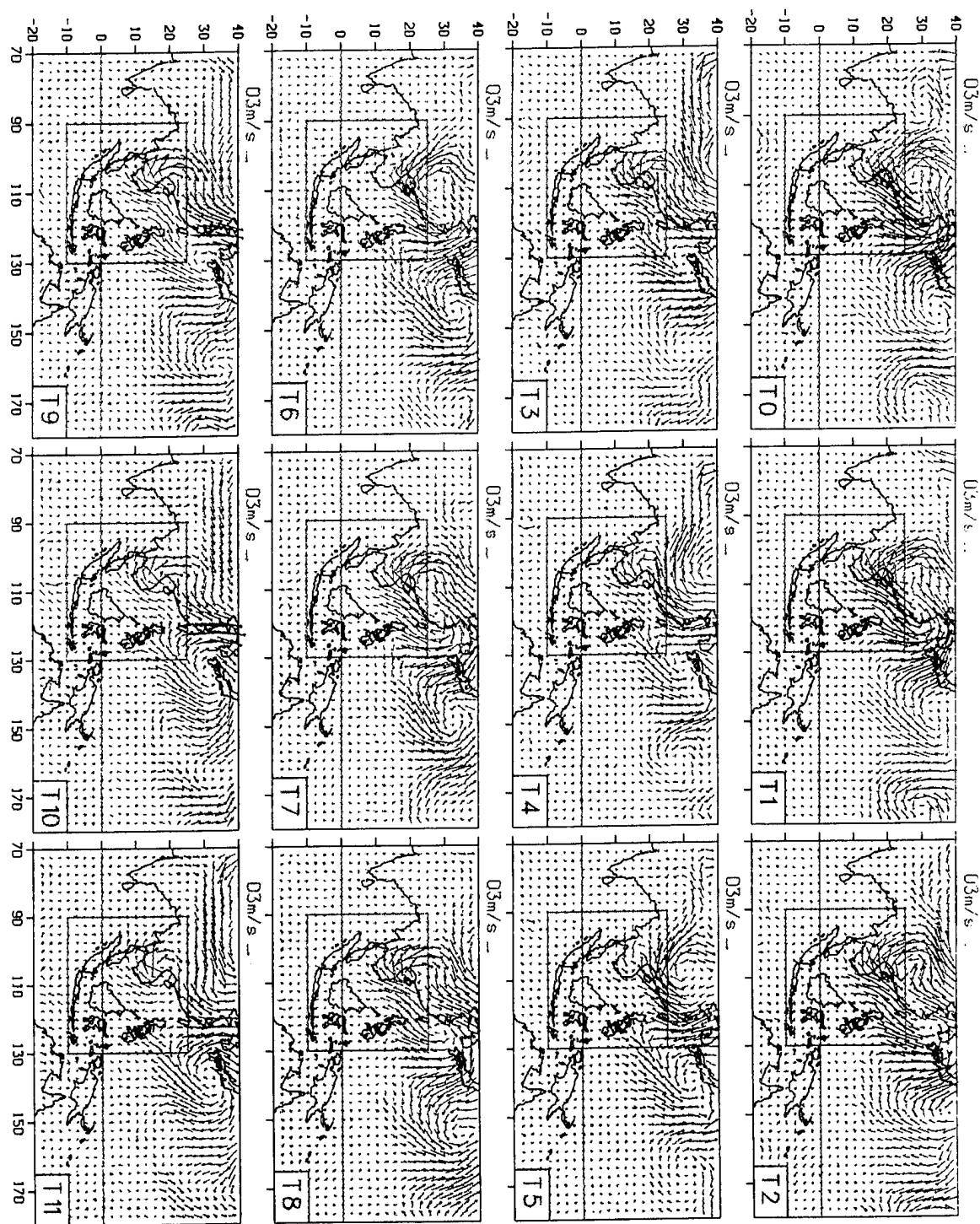


Figure 44. Surface wind vector plots based on composites of the 13 strongest cold surge cases at 12 consecutive 12-hourly time lags with the background mean removed. Vector scale is shown at the top of each frame.

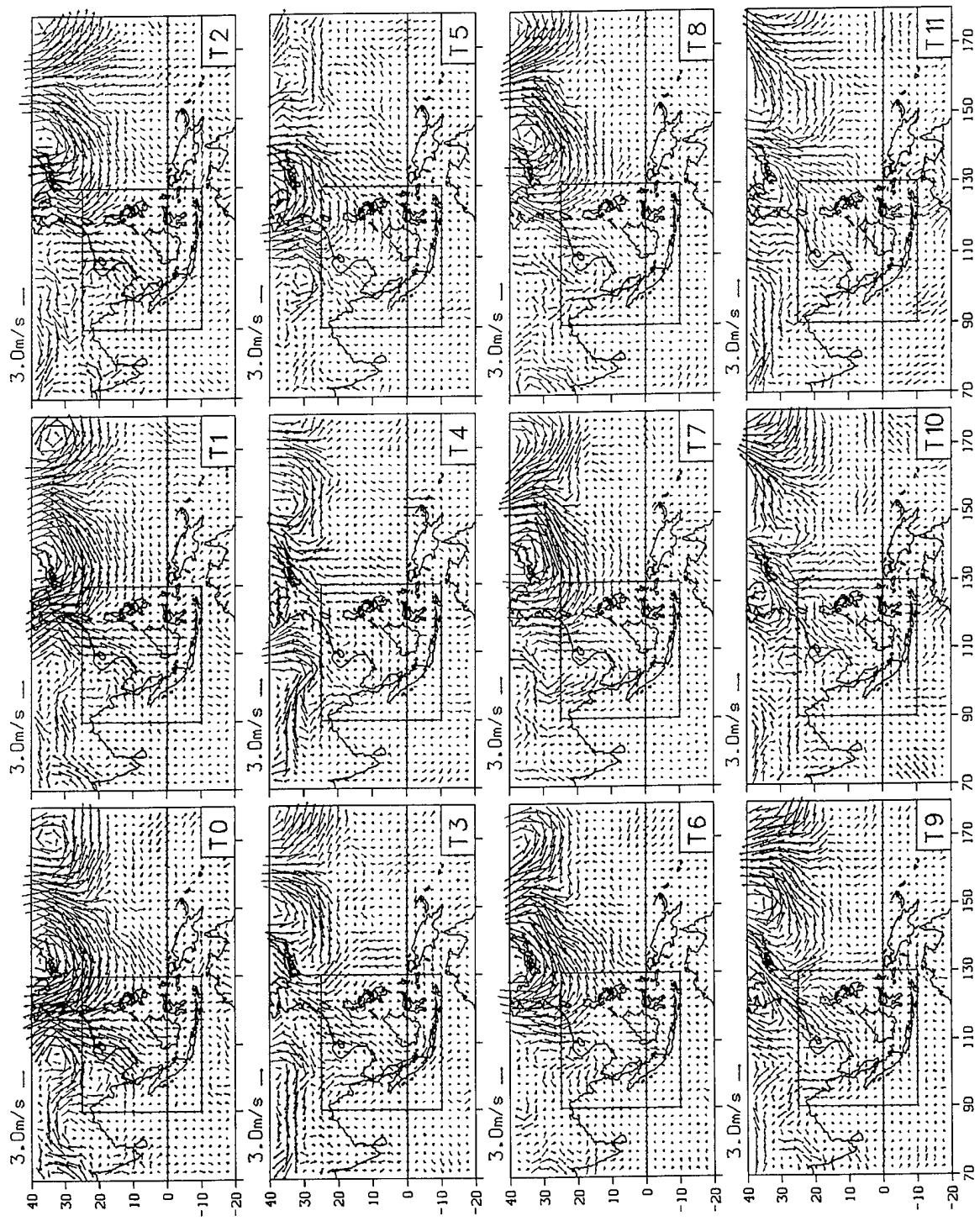


Figure 45. Same as Fig. 44 except for 700 hPa.

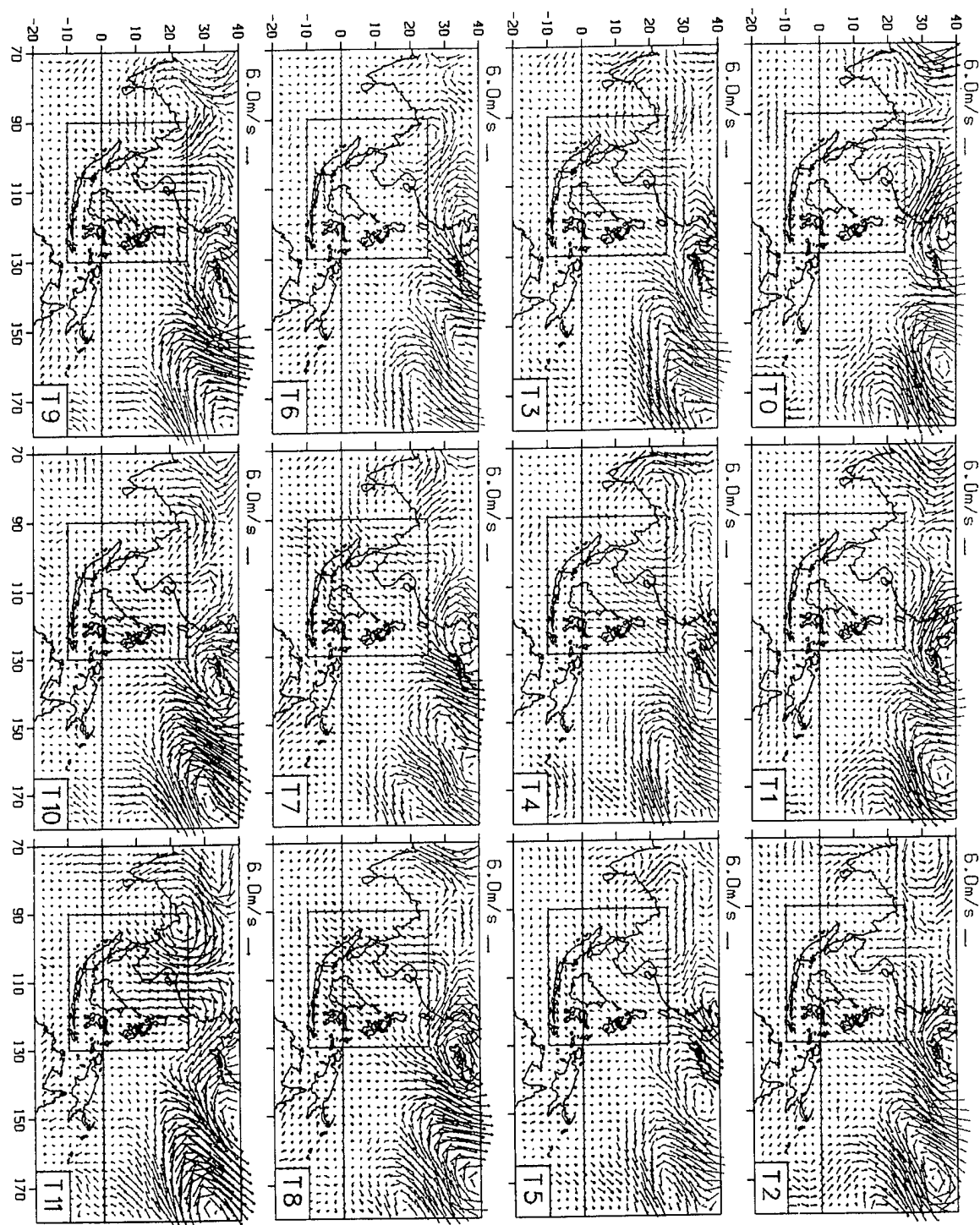


Figure 46. Same as Fig. 44 except for 200 hPa.

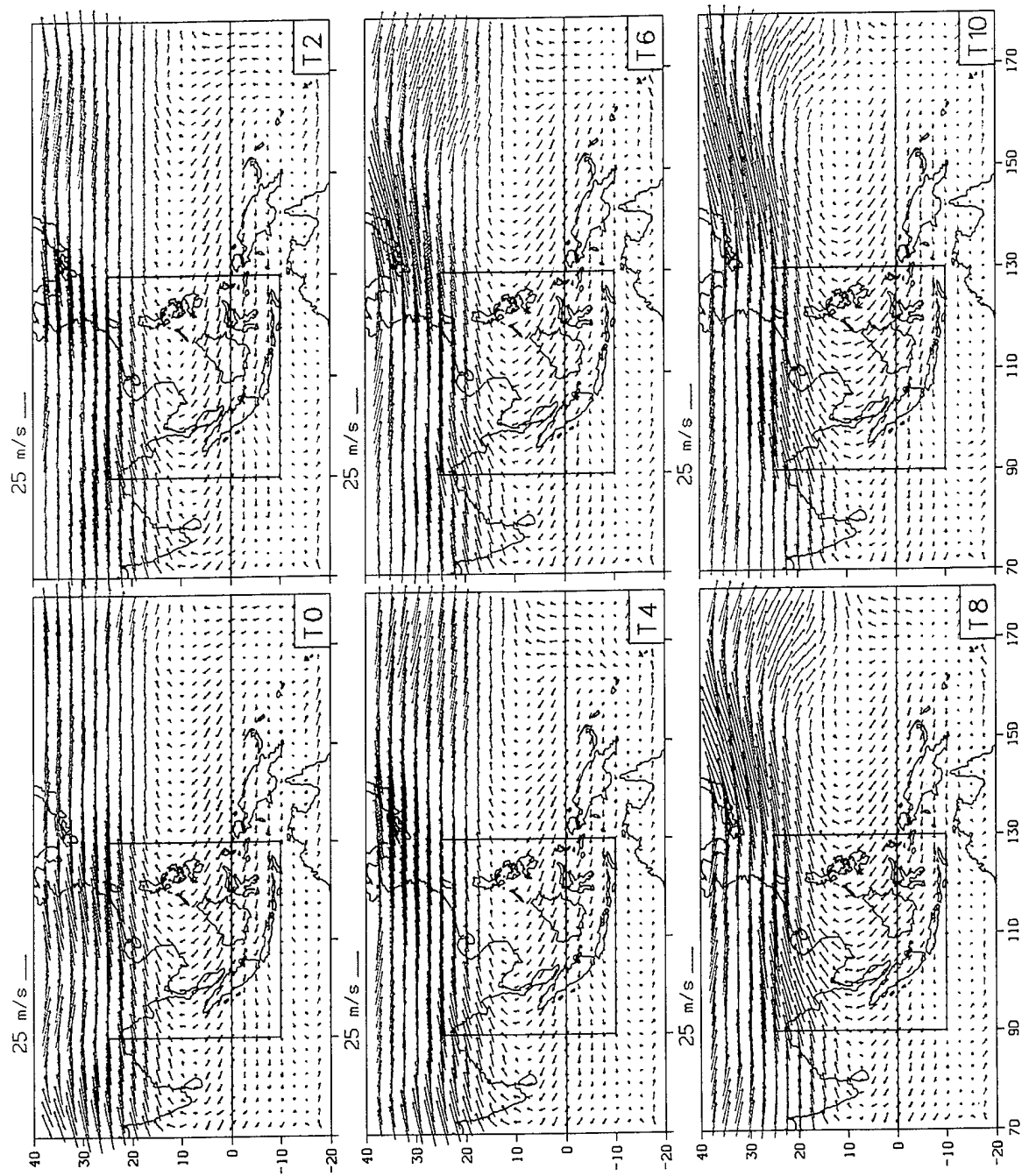


Figure 47. 200 hPa wind vector plots based on composites of the 13 strongest cold surge cases at 6 consecutive 24-hourly time lags with the background mean included. Vector scale is shown at the top of each frame.

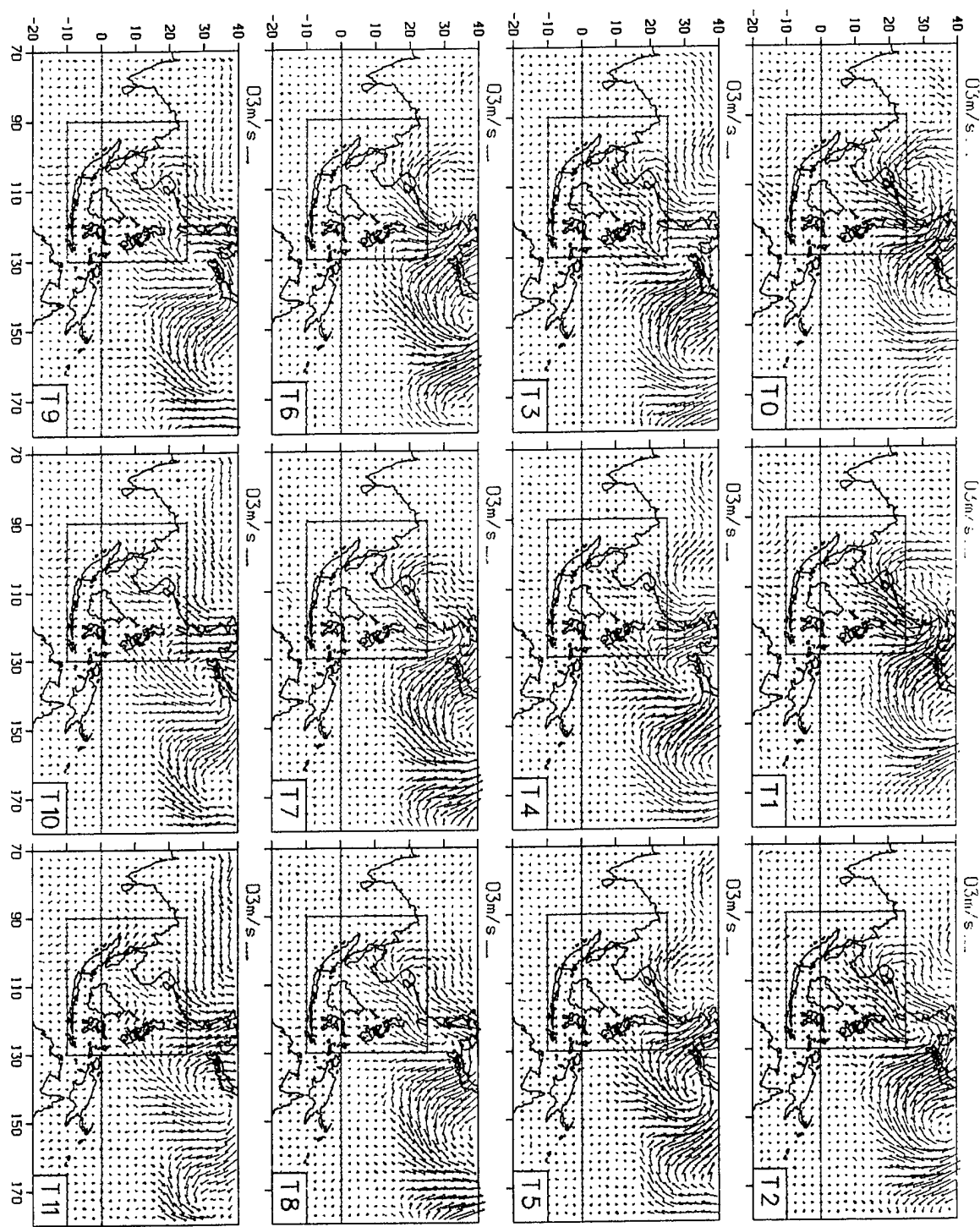


Figure 48. Surface wind vector plots based on composites of 54 medium-strength cold surge cases at 12 consecutive 12-hourly time lags with the background mean removed. Vector scale is shown at the top of each frame.

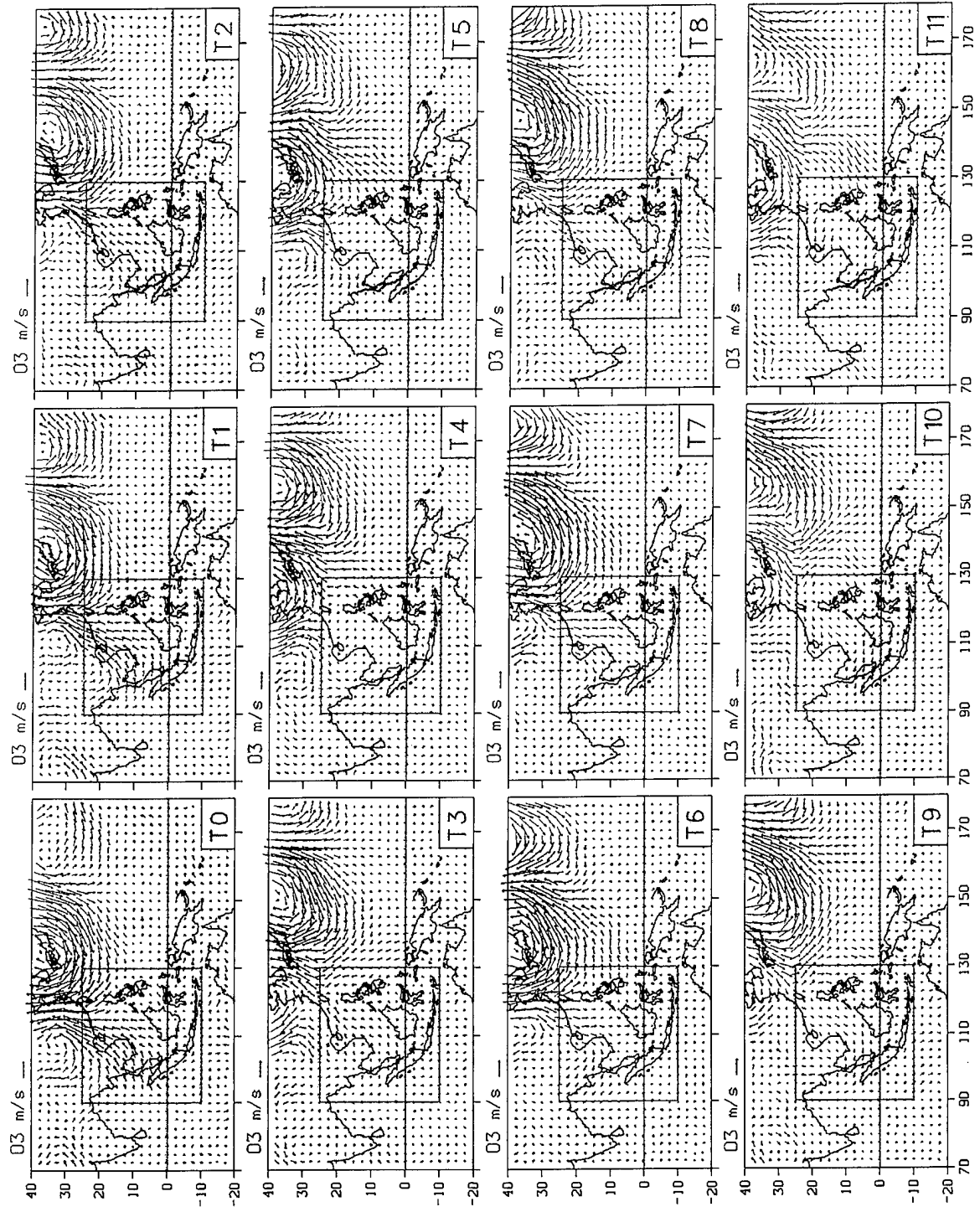


Figure 49. Same as Fig. 48 except for 700 hPa.

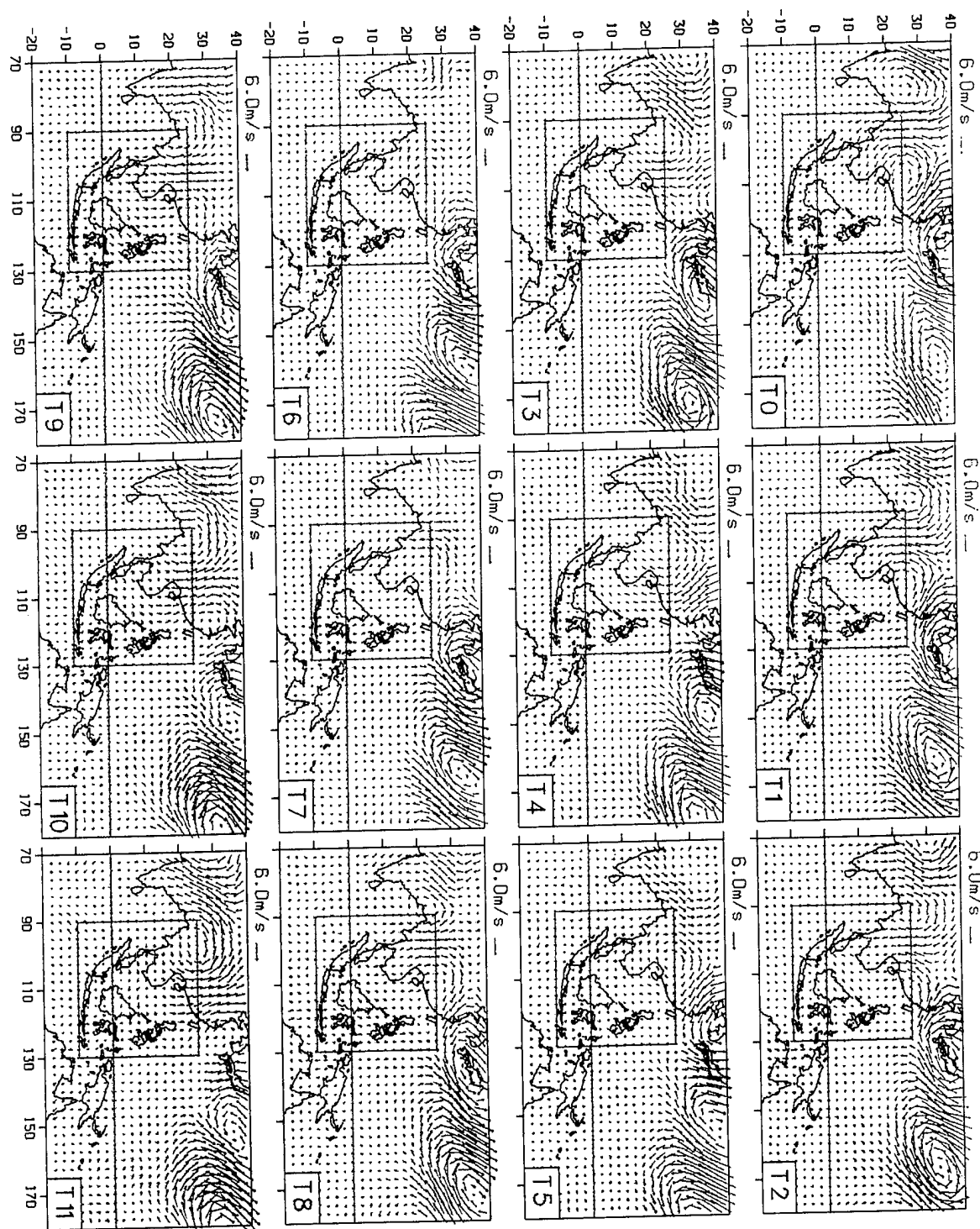


Figure 50. Same as Fig. 48 except for 200 hPa.

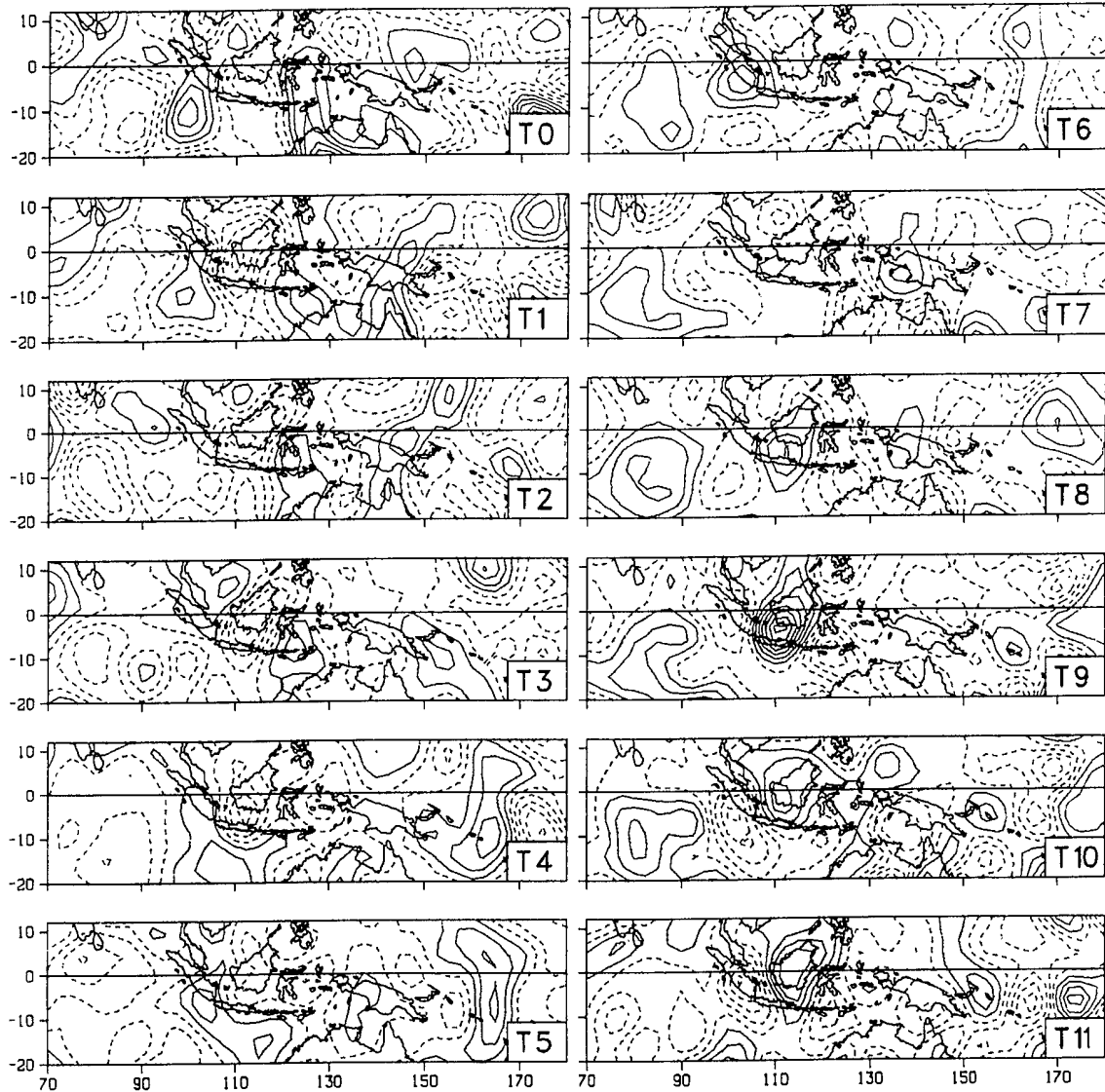


Figure 51. Spatially averaged 200 hPa anomaly divergence fields based on composites of the 13 strongest cold surge cases at 12 consecutive 12-hourly time lags. Contour interval is 0.000002 1/s.

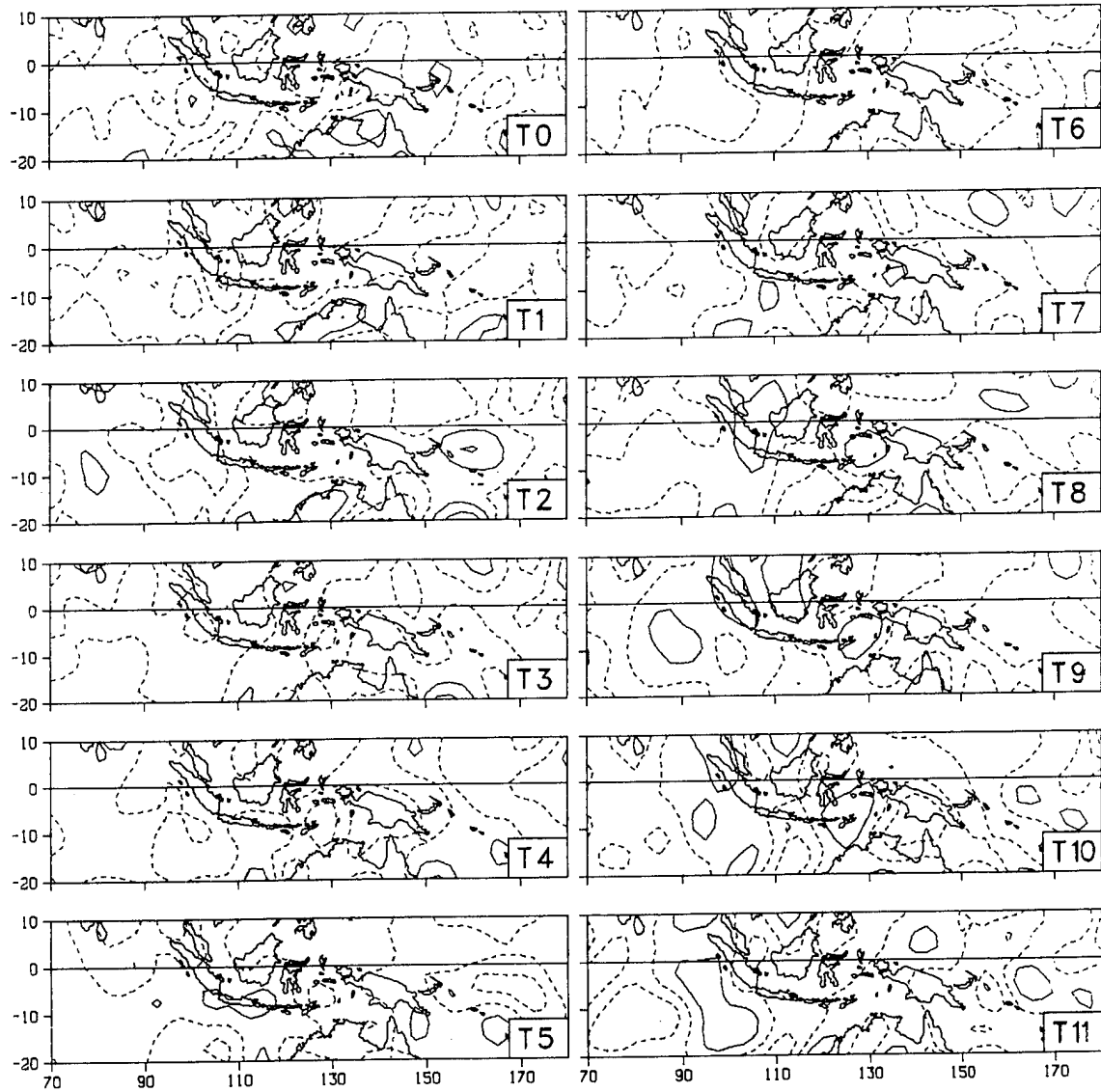


Figure 52. Same as Fig. 51 except for 54 medium-strength cases.

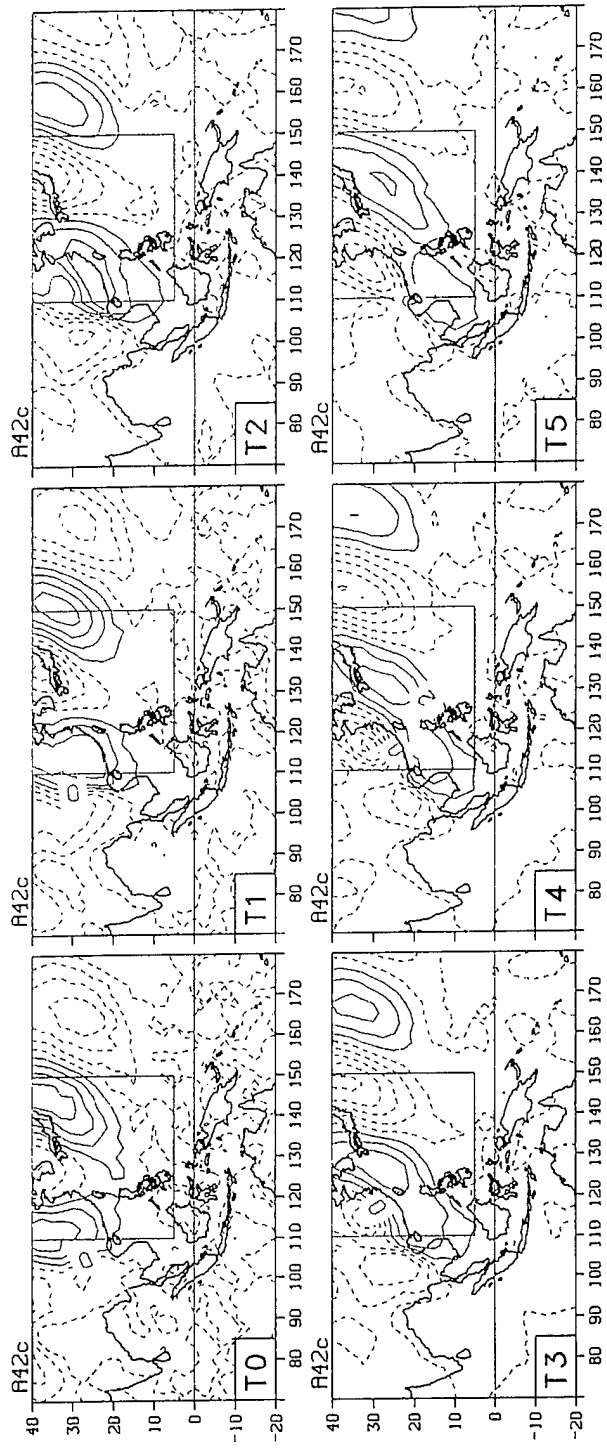


Figure 53. Single-point correlation patterns of surface v with MCC mode 3, East China Sea domain, at 6 consecutive 12-hourly time lags. Contour interval is 0.1 and negative values are dashed.

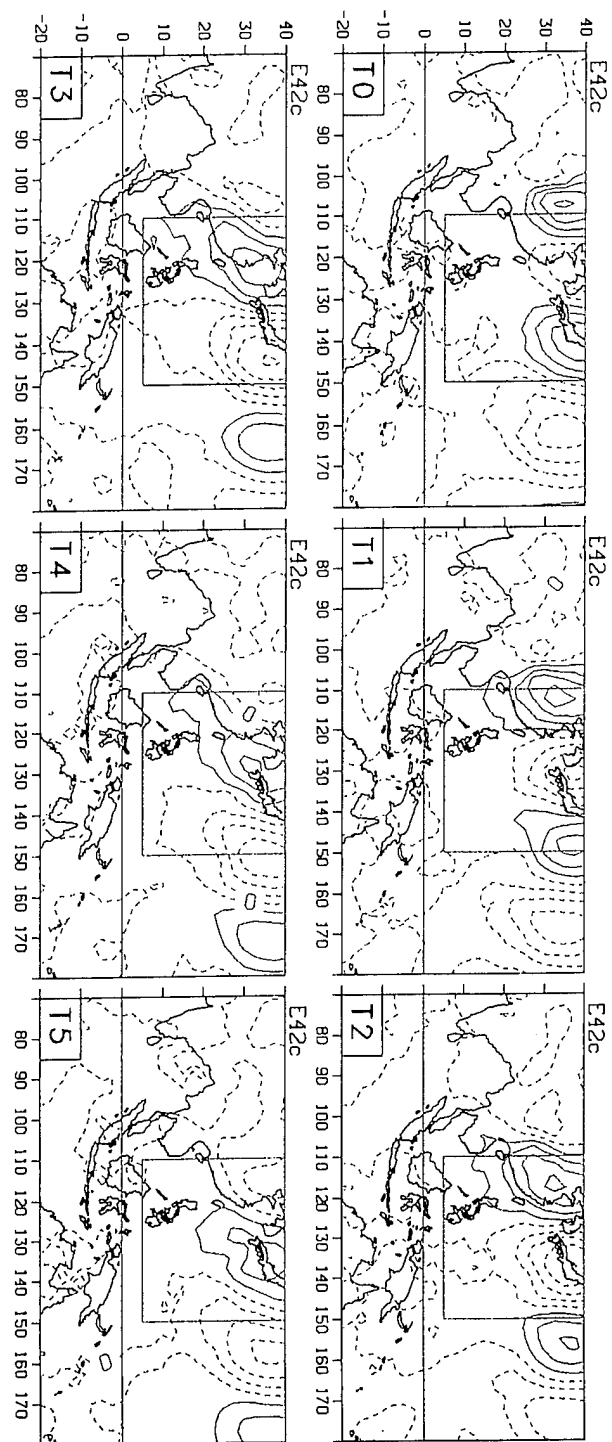


Figure 54. Same as Fig. 53 except for 700 hPa.

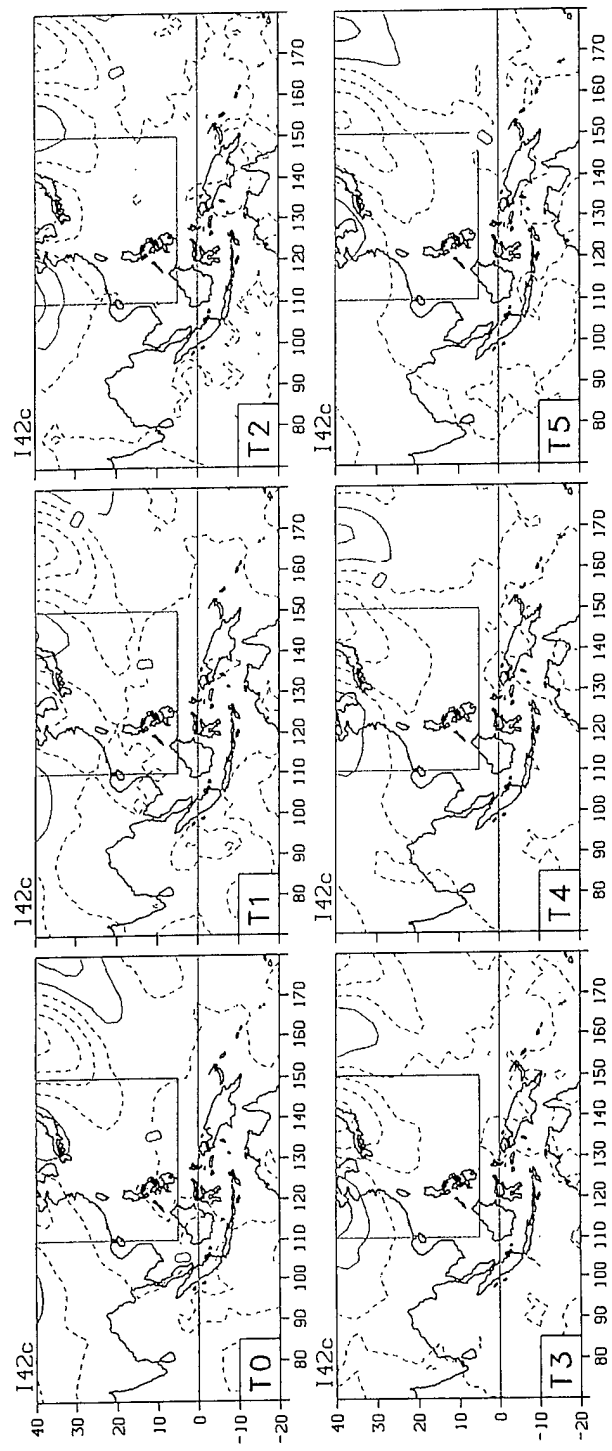


Figure 55. Same as Fig. 53 except for 200 hPa.

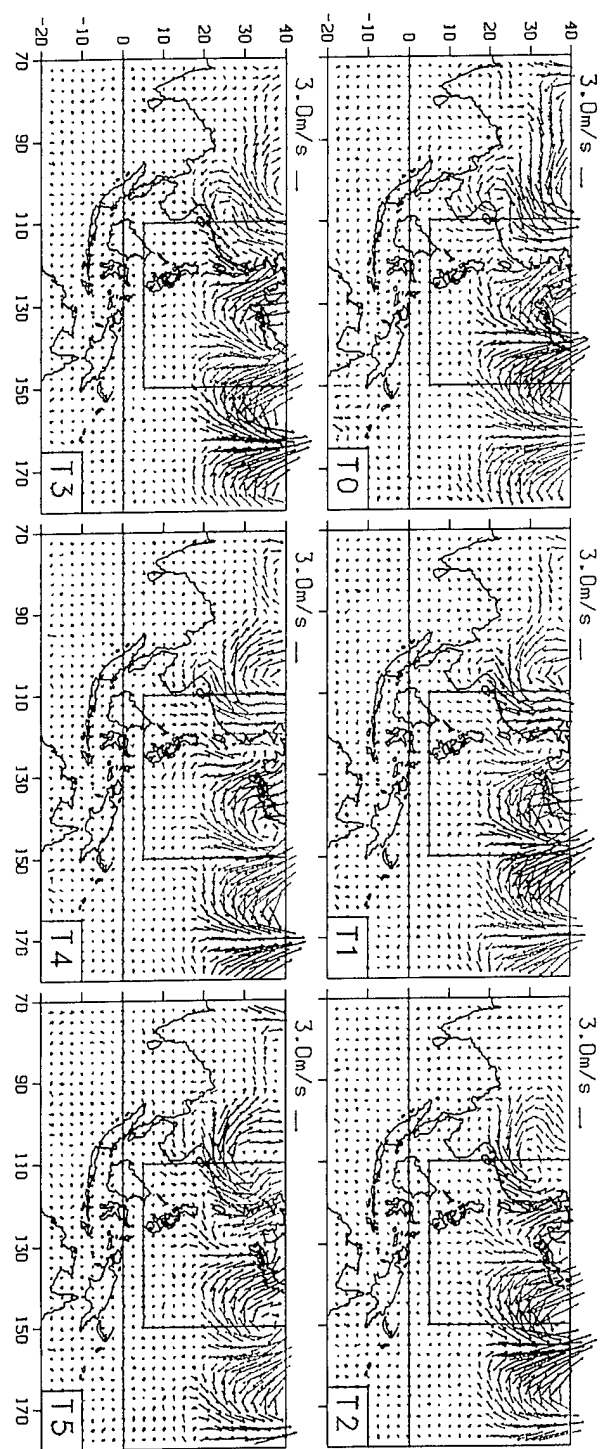


Figure 56. Surface wind vector plots based on composites of 27 cases at 6 consecutive 12-hourly time lags with the background mean removed. Vector scale is given at the top of each frame.

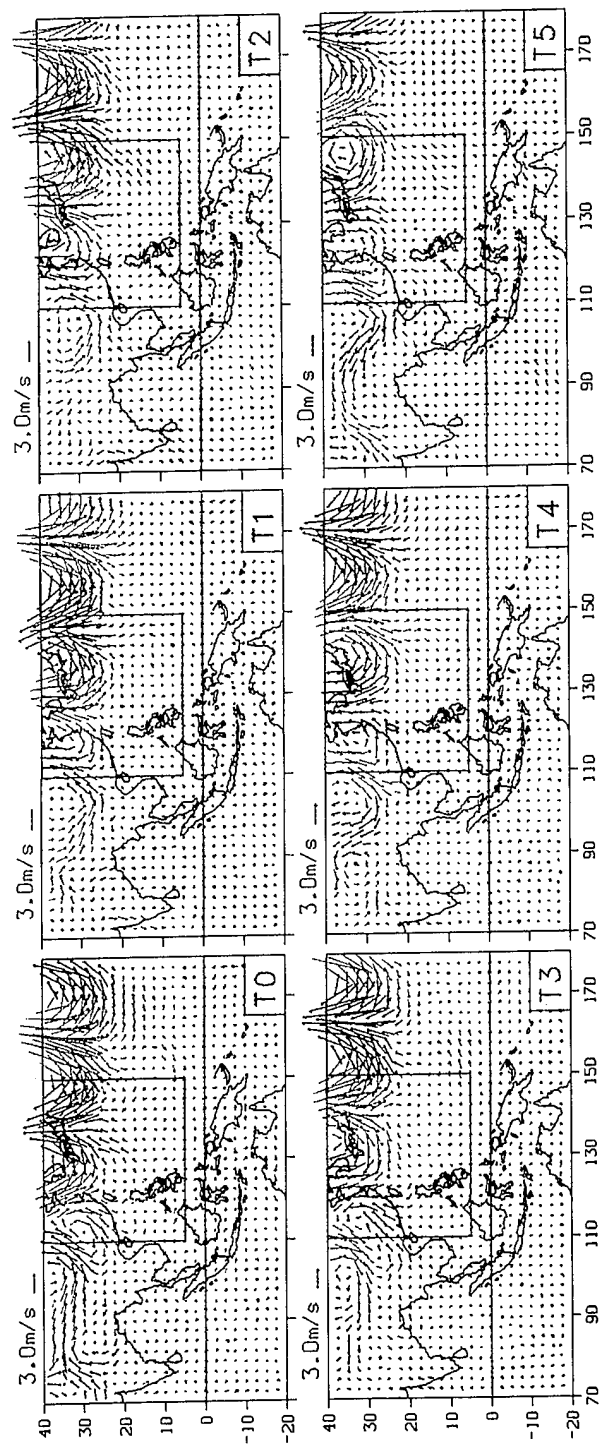


Figure 57. Same as Fig. 56 except for 700 hPa.

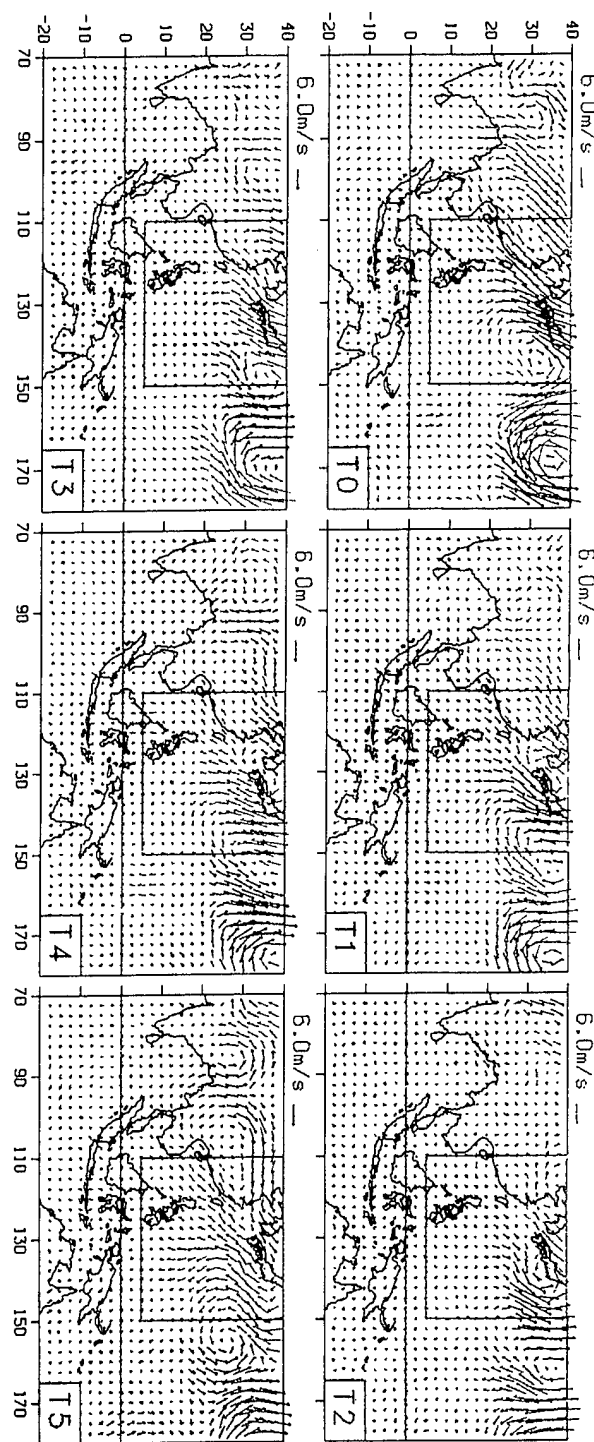


Figure 58. Same as Fig. 56 except for 200 hPa.

V. SUMMARY AND CONCLUSIONS

In this study we examine the structures of motions over a large domain that includes the western Pacific and eastern Indian oceans during 14 winters from 1975-1988 using Navy tropical Global Band Analysis (GBA) data. Multiple-set Canonical Correlation Analysis (MCCA) is applied to 12 datasets in two small domains that are imbedded in a large domain that includes the western Pacific and eastern Indian oceans. The structure of motions in the large domain is then determined through the use of single-point correlation analysis and composite analysis based on the basic MCC modes. The 12 datasets are constructed by a forward sliding time window which consists of 12 twice-daily time frames of the surface v field, through 3 months of the year (January, February, March). The resulting MCC modes are ranked by the geometrically-averaged correlation between surface v fields of adjacent times within the 12 time frames, or 5.5 days.

MCC modes 1 and 2 calculated over the small South China Sea and East China Sea domains reveal the basic structure of the Asian winter monsoon cold surge. The surge moves across the South China Sea with a positive anomaly moving from north to south followed by a negative anomaly with an average period of 8 days. Previous studies of the cold surge (e.g., Chang and Chen 1992) did not address the character of the "break" in the cold surge. Our result indicates that the break does not occur as a withdrawal of the northeasterly wind northward, but rather as an equatorward propagation of the negative phase. Meanwhile, large-scale disturbances with wavelengths on the order of 3000 to 4000 km propagate eastward from Asia across the East China Sea also with an average period of 8 days. Coherence and phase calculations between the amplitude coefficient time series' of MCC mode 1 for the South China Sea domain and MCC mode 1 for the East China Sea domain confirm that they are both manifestations of the same event (i.e. the cold surge). In addition, the time series' are also used to construct single-point correlation analyses over the large domain. Both MCC mode 1 time series' yield similar correlation patterns. In summary, the surge can be viewed as a *single* mode over a rather broad region with an average period of 8 days that includes eastward propagating longwaves

over the East China Sea and equatorward propagating surge waves across the South China Sea.

Other features evident during cold surge events are depicted in composite plots over the large domain. Cases are selected based on the magnitude of the peaks of the time-integrated amplitude coefficient time series for MCC mode 1. Over the 14-year period 13 cases are categorized as "strong" and 54 cases are categorized as "medium-strength". Cross-equatorial surge influence is seen in both the strong and medium-strength cold surge surface composites. For the strong cases, an increase in northeasterly winds off the northwest coast of Australia is exhibited during the maximum northeasterly surge. For the medium-strength cases, a phase shift in anomalous winds with a period that exactly matches that of the cold surge is observed in the area between 100°E and 110°E along 20°S. The cross-equatorial influence of cold surges has been recognized by other investigators (e.g., Lau 1982; Lau and Chang 1987). At 200 hPa, composite plots reveal a large-scale anomalous anticyclone positioned north of the Bay of Bengal that is gradually replaced by an anomalous cyclone throughout the surge sequence. This feature, which was not reported in previous cold surge studies, exists for both the strong and medium-strength composites. As mentioned previously, whether the circulations are a cause or effect of the cold surge remains unknown. Perhaps reanalysis over a larger domain that includes higher latitudes would provide some insight.

Several investigators have found that there is an increase in the level of convective activity over the general area of the southern South China Sea during monsoon surges (e.g., Houze *et al.* 1981; Chang *et al.* 1979). In order to determine whether or not evidence of this exists in the GBA data, divergence fields are calculated over a tropical band between 20°S and 10°N using 200 hPa u and v components and then composited based on strong and medium-strength amplitude coefficients. Results show a noticeable increase in divergence over Borneo for the strong cases, but not for the medium-strength cases. This indicates that only during strong cold surges is the 200 hPa divergence strong enough to be detectable by our kinematic calculation method. The divergence field composites also show a positive anomaly located along the equator near New Guinea at

the time of the surge onset that slowly moves eastward toward 180° over the 5 1/2 day sequence. This anomaly might be associated with an equatorial Kelvin wave.

Over the East China Sea MCC modes 3 and 4 reveal eastward propagating anomalies with wavelengths on the order of 1500 to 2000 km with an average period of about 3 days. Composite plots of 27 cases selected from the 14 winter seasons show a sequence of shortwaves propagating across the midlatitudes that look similar to the MCC mode 3 weighting function patterns. A reversal in wind anomalies from northerly to southerly with a period of 3 days is present across the South China Sea. This "mini surge" phenomenon present in MCC modes 3 and 4 will provide a contribution to the primary surge seen in MCC modes 1 and 2 when the two pair are in phase. Nitta and Yamamoto (1973) also found cyclones that propagate across the East China Sea with similar wavelengths and periods, however they were shallow with little development above 850 hPa. Our results show that these disturbances are in fact deep. The 200 hPa composite sequence for the same 27 cases show 3-day shortwaves moving off the Asian continent that are about a quarter cycle out of phase with the surface disturbances.

Future investigations of the East Asian cold surge may be conducted with similar statistical techniques used in this study, but with new, improved datasets. The GBA data used here, although it covers a relatively long period, suffers from an analysis scheme that uses persistence as a first guess. Over the data-sparse regions typical in the tropics, this artificial persistence may last for days. Major numerical weather prediction centers in the United States and Europe are now producing reanalyzed data that goes back to the late 1970's. These reanalyses are four-dimensional assimilated data that use model forecasts as a first guess rather than persistence fields. In these reanalyzed data all variables at all standard levels are available for a detailed analysis. This may offer more insight into some of the features associated with cold surges that were examined in this study.

LIST OF REFERENCES

Barnett, T.P., and R.W. Preisendorfer, 1987: Origins and levels of monthly and seasonal forecast skill for the United States surface air temperatures determined by canonical correlation analysis. *Mon. Wea. Rev.*, **115**, 1825-1850.

Boyle, J.S., and Chen, T.J., 1987: Synoptic aspects of the wintertime East Asian monsoon. In *Monsoon Meteorology*, C.P. Chang and T.N. Krishnamurti, Eds., Oxford University Press, 125-160.

Cardenas Amores, J.A., 1994: Intraseasonal oscillations over the tropical western Pacific and eastern Indian Ocean for the northern summers of 1989-1991. Master's Thesis, Naval Postgraduate School, Monterey, CA, 106 pp.

Chang, C.P., V.F. Morris, and J.M. Wallace, 1970: A statistical study of easterly waves in the western Pacific: July-December 1964. *J. Atmos. Sci.*, **27**, 195-201.

Chang, C.P., and J.M. Chen, 1992: A statistical study of winter monsoon cold surges over the South China Sea and the large-scale equatorial divergence. *J. Meteorol. Soc. Japan*, **70**, 287-302.

Chang, C.P., J.E. Erickson, and K.M. Lau, 1979: Northeasterly cold surges and near equatorial disturbances over the winter MONEX area during December 1974. Part I: Synoptic aspects. *Mon. Wea. Rev.*, **107**, 812-829.

Chen, T.C., and Chen J.M., 1993: The 10-20 day mode of the 1979 Indian monsoon: its relation with the time variation of monsoon rainfall. *Mon. Wea. Rev.*, **121**, 2465-2482.

Chang, C.P., and C.R. Miller III, 1977: Comparison of easterly waves in the tropical Pacific during two periods of contrasting sea-surface temperature anomalies. *J. Atmos. Sci.*, **34**, 615-628.

Chang, C.P., and K.M. Lau, 1982: Short-term planetary-scale interactions over the tropics and midlatitudes during northern winter. Part I: Contrasts between active and inactive periods. *Mon. Wea. Rev.*, **110**, 933-946.

Chang, C.P., J.E. Erickson, and K.M. Lau (1979): Northeasterly cold surges and near-equatorial disturbances over the winter MONEX area during December 1974. Part I: Synoptic aspects. *Mon. Wea. Rev.*, **107**, 812-829.

Chen, J.M., and C.P. Chang, 1994: A technique for analyzing optimal relationships among multiple sets of data fields. Part 2: A reliability case study. *Mon. Wea. Rev.*, **122**, 2494-2505.

Chen, J.M., C.P. Chang, and P.A. Harr, 1994: A technique for analyzing optimal relationships among multiple sets of data fields. Part 1: The method. *Mon. Wea. Rev.*, **122**, 2482-2493.

Chu, P.S., and S.U. Park, 1984: Regional circulation characteristics associated with a cold surge event over East Asia during winter MONEX. *Mon. Wea. Rev.*, **112**, 955-965.

Dunn, G.E., 1940: Cyclogenesis in the tropical Atlantic. *Bull. Amer. Met. Soc.*, **21**, 215-229.

Frederikson, J. S., 1979: The effect of long planetary waves on the regions of cyclogenesis: Linear theory. *J. Atmos. Sci.*, **36**, 2320-2335.

GARP (Global Atmospheric Research Program), 1981: Scientific results of the Air Mass Transformation Experiment (AMTEX). GARP Publication Series No. 24, World Meteorological Organization, Geneva.

Glahn, H.R., 1968: Canonical correlation and its relationship to discriminant analysis and multiple regression. *J. Atmos. Sci.*, **25**, 23-31.

Hotelling, H., 1935: The most predictable criterion. *J. Edu. Psych.*, **26**, 139-142.

Hotelling, H., 1933: Analysis of a complex of statistical variables into principal components. *J. Edu. Psych.*, **26**, 139-142.

Hotelling, H., 1936: Relations between two sets of variates. *Biometrika*, **28**, 321-377.

Houze, R.A., S.G. Geotis, F.D. Marks, and A.K. West, 1981: Winter monsoon convection in the vicinity of North Borneo. Part I: Structure and time variation of the clouds and precipitation. *Mon. Wea. Rev.*, **109**, 1595- 1628.

Johnson, R.H., and D.L. Priegnitz, 1981: Winter monsoon convection in the vicinity of North Borneo. Part II: Effects on large-scale fields. *Mon. Wea. Rev.*, **109**, 1615- 1628.

JTWC, 1988: Annual Tropical Cyclone Report, Joint Typhoon Warning Center Guam, Mariana Islands, 216 pp.

Lau, K.M., and P.H. Chan, 1983: Short-term climate variability and atmospheric teleconnections from satellite observed outgoing longwave radiation. Part I: Simultaneous relationships. *J.Atmos.Sci.*, **40**, 2735-2750.

Lau, K.H., and N.C. Lau, 1990: Observed structure and propagation characteristics of tropical summertime synoptic-scale disturbances. *Mon.Wea.Rev.*, **118**, 1888-1913.

Lau, K.M., 1982: Equatorial response to northeasterly cold surges as inferred from satellite cloud imagery. *Mon.Wea.Rev.*, **110**, 1306-1313.

Lau, K.M., and C.P. Chang, 1987: Planetary scale aspects of the winter monsoon and atmospheric teleconnections. In *Monsoon Meteorology*, C.P. Chang and T.N. Krishnamurti, Eds. Oxford University Press, 161-202.

Lewis, J.M., and T.H. Grayson, 1972: The adjustment of surface wind and pressure by Sasaki's variations matching technique. *J.Appl.Meteor.*, **11**, 586-597.

Liebmann, B., and H.H. Hendon, 1990: Synoptic scale disturbances near the equator. *J.Atmos.Sci.*, **47**, 1463-1479.

Lorenz, E.N., 1956: Empirical orthogonal functions and statistical weather prediction. Science Report No. 1, Statistical Forecasting Project, Dept. of Meteorology, Massachusetts Institute of Technology, Cambridge, MA, 49 pp.

Madden, R.A., and P.R. Julian, 1971: Description of a 40-50 day oscillation in the zonal wind in the tropical Pacific. *J.Atmos.Sci.*, **28**, 702-708.

Manabe, S., and T.B. Terpstra, 1974: The effects of mountains on the general circulation of the atmosphere as identified by numerical experiments. *J.Atmos.Sci.*, **31**, 3-42.

Maruyama, T., 1967: Large-scale disturbances in the equatorial lower stratosphere. *J.Meteorol.Soc.Japan*, **45**, 391-408.

Maruyama, T., 1968: Time sequence of power spectra of disturbances in the equatorial lower stratosphere in relation to the quasi-biennial oscillation. *J.Meteorol.Soc.Japan*, **46**, 327-342.

Nitta, T., and J. Yamamoto, 1974: On the observational characteristics of intermediate-scale disturbances generated near Japan and vicinity. *J.Meteorol.Soc.Japan*, **52**, 11-31.

Nitta, T., Y. Nakagomi, Y. Suzuki, N. Hasegawa, and A. Kadokura, 1985: Global analysis of the lower tropospheric disturbances in the tropics during the northern summer of the FGGE year. Part I: Global features of the disturbances. *J.Meteorol.Soc.Japan*, **63**, 1-19.

Nitta, T., and Y. Takayabu, 1985: Global analysis of the lower tropospheric disturbances in the tropics during the northern summer of the FGGE year. Part II: Regional characteristics of the disturbances. *Pure.Appl.Geophys.*, **123**, 272-292.

Piersig, W., 1936: Schwankungen von Luftdruck und Luftbewegung sowie ein Beitrag zum Wettergeschehen im Passatgebiet des oestlichen nordatlantischen Ozeans. *Arch.Dent.Seewarte.*, **54**(6). [Parts I and II have been translated and printed, 1944: The cyclonic disturbances of the subtropical eastern north Atlantic. *Bull.Amer.Meteor.Soc.*, **25**, 2-17.]

Preisendorfer, R.W., 1988: *Principal Component Analysis in Meteorology and Oceanography*. Elsevier, 425 pp.

Prohaska, J.T., 1976: A technique for analyzing the linear relationships between two meteorological fields. *Mon.Wea.Rev.*, **104**, 1345-1353.

Reed, R.J., A. Hollingsworth, W.A. Heckley, and F. Delsol, 1988: An evaluation of the performance of the ECMWF operational forecasting system in analyzing and forecasting easterly wave disturbances over Africa and the tropical Atlantic. *Mon.Wea.Rev.*, **116**, 824-865.

Regula, M., 1936: Druckschwankungen und Tornados an der westküste von Afrika. *Ann.Hydrog.Mar.Meteor.*, **64**, 107-111.

Riehl, H., 1945: Waves in the easterlies and the polar front in the tropics. *Misc.Rep.No.17*, Dept. of Meteorology, University of Chicago, 79 pp.

Saito, N., 1977: On the structure of medium-scale depressions over the East China Sea during AMTEX 75. *J.Meteorol.Soc.Japan*, **55**, 286-300.

Salby, M.L., and Hendon H.H., 1994: Intraseasonal behavior of clouds, temperature, and motion in the tropics. *J.Atmos.Sci.*, **51**, 2207-2224.

Tai, K.S., and Y. Ogura, 1987: An observational study of easterly waves over the eastern Pacific in the northern summer using FGGE data. *J.Atmos.Sci.*, **44**, 339-361.

Wallace, J.M., and C.P. Chang, 1969: Spectrum analysis of large-scale wave disturbances in the tropical lower troposphere. *J.Atmos.Sci.*, **26**, 1010-1025.

Yanai, M., T. Maruyama, T. Nitta, and Y. Hayashi, 1968: Power spectra of large-scale disturbances over the tropical Pacific. *J.Meteorol.Soc.Japan*, **46**, 308-323.

INITIAL DISTRIBUTION LIST

	No. Copies
1. Defense Technical Information Center Cameron Station Alexandria, Virginia 22304-6145	2
2. Library, Code 52 Naval Postgraduate School Monterey, California 93943-5101	2
3. Chairman (Code OC / Bk) Department of Oceanography Naval Postgraduate School Monterey, CA 93943-5000	1
4. Chairman (Code MR / Hy) Department of Meteorology Naval Postgraduate School Monterey, CA 93943-5000	1
5. Prof. Chih-Pei Chang (Code MR / Cp) Department of Meteorology Naval Postgraduate School Monterey, CA 93943-5000	2
6. Prof. Jeng Ming Chen (Code MR / Ch) Department of Meteorology Naval Postgraduate School Monterey, CA 93943-5000	1
7. Prof. Patrick Harr (Code MR / Hp) Department of Meteorology Naval Postgraduate School Monterey, CA 93943-5000	1
8. LT James R. Jarvis 1135 Third St Monterey, CA 93940	2